

Aerodynamics of cylinders in tandem

Experimental investigation by stereoscopic PIV

Master Thesis

Jože Bajuk

Aerodynamics of cylinders in tandem

Experimental investigation by stereoscopic PIV

by

Jože Bajuk

to obtain the degree of Master of Science
at the Delft University of Technology,
to be defended publicly on Friday January 26, 2024 at 9:30.

Thesis supervisors:

A. Sciacchitano	TU Delft - Aerodynamics
H. Ubbens	Team DSM - Aerodynamic and innovation expert
W. Terra	NOC*NSF - Embedded Scientist Aerodynamics
Student number:	5136857
Date:	January, 2024
Faculty:	Faculty of Aerospace Engineering, TU Delft

An electronic version of this thesis is available at <http://repository.tudelft.nl/>.

Preface

At this opportunity that marks the end of a chapter and the start of a new one, I would like to acknowledge people without whom I would not be here.

Firstly, my supervisors Andrea Sciacchitano, Harm Ubbens, and Wouter Terra for guidance throughout the master thesis. You set a high standard and allowed me to experience how academic research should be carried out. You were always willing to help and contributed greatly to this work. I could not wish for a better team. Thank you.

Secondly to my parents. Without your stability and support, none of this would be possible. I always knew I could count on you, which made focusing on my dreams immeasurably easier. Thank you!

Finally, I would like to thank Iris Grže from the bottom of my heart for believing in me and showing me that I can fly. I did not know how much my life would change when I met you. Thank you!

*Jože Bajuk
Delft, January 2024*

Abstract

This thesis investigates the aerodynamics of two finite wall-mounted cylinders in tandem, focusing on drag reduction as a function of governing parameters.

For the experimental wind tunnel campaign, two measurement techniques were employed: balance measurements and stereoscopic particle image velocimetry. While balance measurements exhibited good repeatability, drag values obtained with PIV saw high uncertainty and only limited conclusions could be made from it.

Cylinders were mounted to the floor of a closed wind tunnel test section. The trailing cylinder was rigidly attached to the balance underneath, while the leading cylinder could move upstream to the desired distance. Stereoscopic PIV images of the wake at various distances upstream and downstream were taken through the transparent sides of the wind tunnel. These images, in combination with the control volume approach, were used to determine the drag of a trailing cylinder.

Coefficients of drag, obtained with a balance for isolated cylinders of various aspect ratios, were in line with similar results from the literature, albeit on the higher side. For cylinders in tandem of the same aspect ratio, AR , as the distance between them increased, the C_D of a trailing cylinder converged to that of an isolated cylinder. Comparing tandem configurations with different AR and at the same nondimensionalized in-between distance, trailing cylinders with larger AR experienced larger drag reduction.

Introducing cylinder diameter ratio as an additional degree of freedom showed that smaller diameter trailing cylinders experienced greater drag reduction at close distances. However, at a certain distance further downstream, this trend reversed.

The drag reduction values obtained with PIV confirmed the findings from balance measurements. However, due to the limited set of usable data, further work would need to be carried out to gain more confidence in the method.

Contents

Abbreviations and Symbols	ix
1 Introduction	1
2 Cylinder Aerodynamics	2
2.1 Isolated Cylinder	2
2.1.1 Flow Topology Around a Cylinder of Infinite Height	2
2.1.2 Flow Topology Around a Cylinder of Finite Height	7
2.2 Cylinders in Tandem	12
2.2.1 Flow Topology Around Two Equal Infinite Cylinders in Tandem	12
2.2.2 Effects on Drag	16
2.2.3 Flow Topology Around Two Infinite Cylinders of Different Diameters in Tandem	17
2.3 Research Objective	21
3 Measurement Techniques	22
3.1 Balance Measurements	22
3.2 Particle Image Velocimetry	22
3.2.1 Tracer Particles	23
3.2.2 Laser Illumination	25
3.2.3 Imaging	25
3.2.4 Data Processing	26
3.3 Stereo-PIV	27
3.3.1 Stereo-PIV Setup	28
3.3.2 Calibration	28
3.3.3 Velocity Field Reconstruction	29
3.3.4 Recommendations	30
3.4 PIV Uncertainty Quantification	30
3.5 Control Volume Approach	32
3.5.1 Theoretical Background	32
3.6 Pressure from PIV	34
3.6.1 Uncertainty of the Pressure Measurements	35
3.7 Aerodynamic Drag Uncertainty with CVA	36
3.8 Examples of CVA Application	36
3.9 Wind Tunnel	38
3.9.1 Cylinder Wind Tunnel Corrections	39
4 Experimental Setup	40
4.1 Wind Tunnel Facility	40
4.2 Cylinder Models	41
4.3 Measurement Techniques	42
4.3.1 Balance Measurements	42
4.3.2 Stereo-PIV	43
4.4 Measurement Campaign	45
5 Data Reduction and Processing	46
5.1 Balance Measurements Data Processing	46
5.2 PIV Data Processing	47
5.2.1 Light Reflection	47
5.2.2 PIV Post-processing Settings	48
5.2.3 Domain	48
5.3 Freestream	49

5.4	Aerodynamic Drag Force from PIV	51
5.4.1	Conservation of Mass	51
5.4.2	Momentum Term	53
5.4.3	Re Stress Term	53
5.4.4	Pressure Term	54
5.5	C_D from CVA	57
6	Results	61
6.1	Aerodynamic Drag of Isolated Cylinders of Finite Height	61
6.1.1	Balance Measurements	61
6.1.2	PIV Measurements	63
6.2	Aerodynamic Drag of Cylinders in Tandem	65
6.2.1	Cylinders in Tandem of the same AR	65
6.2.2	Cylinder in Tandem of Varying AR	66
6.2.3	PIV measurements	70
7	Conclusion	73
7.1	Improvements and Further Research Recommendations	74
7.2	Application in Cycling	75
	References	76
A	Test Matrix	80

List of Figures

2.1	Distinct flow regions around a two dimensional cylinder (M. Zdravkovich and Pridden 1977).	3
2.2	Illustration of the four transitional regions from laminar to turbulent flow. (L) laminar flow, (T) turbulent flow, (Tr) transition, (S) point of separation (M. Zdravkovich and Pridden 1977).	3
2.3	Different flow regimes around a nominally two-dimensional cylinder as a function of the Re (Lienhard et al. 1966).	4
2.4	Coefficient of drag as a function of Re overlaid with information about different flow regions (M. M. Zdravkovich 1997).	5
2.5	$C_D(Re)$ comparison between different experimental studies and one large eddy simulation (LES) (Rodríguez et al. 2015).	6
2.6	Scheme of the flow topology around a low AR cylinder (Pattenden, Turnock, and Zhang 2005).	7
2.7	Visualisation of the upstream horseshoe vortex system (Baker 1980).	7
2.8	Various positions of the main horseshoe vortex core gathered from PIV images (Pattenden, Turnock, and Zhang 2005).	8
2.9	Vorticity distribution. PIV images of the wake were taken at various distances from the cylinder (Pattenden, Turnock, and Zhang 2005).	9
2.10	C_D as a function of aspect ratio, for different BL heights, $Re = 3, 2 \cdot 10^4$, (Kawamura et al. 1984).	10
2.11	Model of the flow by (Kawamura et al. 1984), comparing two cylinders of finite height, showing the <i>suppressed two-dimensional flow</i> around cylinders with higher AR.	11
2.12	A comparison of various experimental studies investigating the drag coefficient (C_D) as a function of aspect ratio (AR). The corresponding Re at which the measurements were taken place can be seen in the legend.	11
2.13	Flow pattern classification based on (Igarashi 1984).	12
2.14	Flow subdivision based on flow topology. The extended body regime is located on the left side with further subdivision of the reattachment regime in the middle and co-shedding regime on the right (Y. Zhou and Yiu 2006).	13
2.15	Comparison between the flow past an isolated cylinder at $Re = 3.0 \cdot 10^3$ and two cylinders in tandem $L = 1.25$ and $Re = 3.3 \cdot 10^3$ (Lars Ljungkrona and Bengt Sundén 1993).	13
2.16	Comparison between the flow past an isolated cylinder at $Re = 3.0 \cdot 10^3$ and two cylinders in tandem $L = 4$ and $Re = 10 \cdot 10^3$ (Lars Ljungkrona and Bengt Sundén 1993).	14
2.17	Comparison between the flow past an isolated cylinder at $Re = 3.0 \cdot 10^3$ and two cylinders in tandem $L = 4$ and $Re = 12 \cdot 10^3$ (Lars Ljungkrona and Bengt Sundén 1993).	14
2.18	Critical pitch ratio (upper curve) and vortex formation length (bottom curve) (L. Ljungkrona, Norberg, and B. Sundén 1991).	15
2.19	Phase average vorticity indicating progression of the Kármán vortices behind cylinders in tandem for different flow regimes due to varying pitch ratio (Y. Zhou and Yiu 2006).	15
2.20	On the left, the patterns of the averaged streamlines are shown behind the cylinder indicating the variable recirculation region, and on the right average streamwise velocity as a function of the distance on the mid-plane (L. Ljungkrona, Norberg, and B. Sundén 1991).	16
2.21	C_D as a function of the pitch ratio. The upper curves represent C_D of the leading cylinder, and the bottom curves that of a trailing cylinder (M. Alam et al. 2003), (Mittal, Kumar, and Raghuvanshi 1997), (M. Zdravkovich and Pridden 1977), (Biermann and Herrnstein 1933).	17
2.22	St as function of d/D for leading and trailing cylinder (Mahbub Alam and Y. Zhou 2008). The cylinders were in the Co-shedding regime at $L = 5.5$.	18

2.23	Visualisation of the flow behind trailing cylinders. Before $x/D < 5$, both lower and higher f shedding vorticity can be observed, but after that, only the dominant remains (Mahbub Alam and Y. Zhou 2008).	18
2.24	Normalised time averaged streamwise velocity in the gap at $x/D = -1$ (a) and behind the cylinder at $x/D = 1$ (b) and $x/D = 4$ (c), for different d/D (Mahbub Alam and Y. Zhou 2008).	19
2.25	C_D of a trailing cylinder as a function of d/D for cylinders in tandem at $l = 5.5$ (Mahbub Alam and Y. Zhou 2008).	19
2.26	C_D as a function of L for different d/D (L. Wang, M. M. Alam, and Yu Zhou 2018).	20
3.1	An example of a experimental PIV setup to examine the flow around a cylinder, where the measurement plane is parallel to the free stream direction (Atkins 2016).	23
3.2	Example of a light scatter pattern around a particle (Andrea Sciacchitano and Fulvio Scarano 2022)	24
3.3	Two images of the flow separated by Δt (Andrea Sciacchitano and Fulvio Scarano 2022).	26
3.4	Example of interrogation windows from the two images separated by Δt and a resulting cross-correlation map between them (Raffel et al. 2018).	27
3.5	Angular lens displacement method with tilted back plane stereo-PIV imaging configuration (Raffel et al. 2018).	28
3.6	An example of a dual level calibration target used for stereo-PIV (LaVision n.d.).	29
3.7	Geometrical reconstruction of the stereo-PIV setup for XZ-plane (Raffel et al. 2018).	29
3.8	Control volume around a cylinder. Cylinder is not part of the fluid and the cylinder surface acts as a part of a control surface.	32
3.9	Left-hand side of the figure shows pressure distribution in the wake of a sphere, and the right plot shows C_D of a sphere as a function of the distance of the outlet plane from the sphere alongside individual contributions to the C_D (Terra, Sciacchitano, and Scarano 2017).	37
3.10	Schematic representation of the two cyclists in tandem and locations of the PIV images taken to be used as inlet and outlet for CVA. (A. Spoelstra et al. 2021).	38
3.11	Drag reduction as a function of the longitudinal and lateral spacing between the two cyclists in tandem (A. Spoelstra et al. 2021).	38
4.1	Wind tunnel experiment setup with the orientation of the coordinate system.	40
4.2	Scheme of the top-down look at the WT section where the measurements took place.	41
4.3	A selection of cylinders used for the experiment.	42
4.4	Balanced used for the experiment.	42
4.5	Attachment connecting cylinders to the balance.	43
4.6	Pulsed laser used for the experiment with lenses used to expand and contract the laser beam.	44
4.7	The two cameras focus on the measurement plane without perturbing the flow in Figure a).Lens connected to the camera through the Scheimflug attachments in figure b).	44
4.8	Multilevel calibration plate.	45
5.1	$C_D(Re)$ for the two isolated cylinders. Each line represents a specific run repeated at different WT velocities. Where there is only a point, the measurement was performed only at one WT velocity.	47
5.2	Raw PIV image and that image overlaid with the computed velocity field.	48
5.3	Velocity fields for individual components of the velocity vector for the isolated cylinder with $D = 5$ cm $H = 20$ cm and the distance between its center and PIV measurement plane 50 cm.	49
5.4	Freestream velocity component of the freestream velocity field, overlaid with lines that signify which sections were examined in figure 5.5.	49
5.5	Velocity profiles.	50
5.6	Images of the inlet and outlet with wake mask applied.Cylinder with $D = 4$ cm, $H = 24$ cm and the distance between it and PIV measurement plane 22 cm.	52
5.7	Images of the wake with the maximum available downstream outlet plane. Cylinder with $D = 4$ cm, $H = 24$ cm and the distance between it and PIV measurement plane 22 cm.	52

5.8	Images of the dynamic pressure distribution over the inlet and outlet. Cylinder with $D = 4$ cm, $H = 24$ cm and the distance between it and PIV measurement plane 22 cm.	53
5.9	Images of the turbulent kinetic energy distribution over the inlet and outlet. Cylinder with $D = 4$ cm, $H = 24$ cm and the distance between it and PIV measurement plane 22 cm.	54
5.10	Pressure distribution on the upstream and downstream plane behind a cylinder.	55
5.11	vorticity behind a cylinder with regions of clockwise and anticlockwise matching observations from the literature.	55
5.12	Images of the pressure distribution over the inlet and outlet. Cylinder with $D = 4$ cm, $H = 24$ cm and the distance between it and PIV measurement plane 22 cm.	56
5.13	Pressure distribution along upstream and downstream planes.	57
5.14	Images of the wake at varying distances behind the cylinder with $D = 4$ cm, $AR = 6$ and high WT speed setting. The images show the freestream component $w(x, y)$	58
5.15	C_D as a function of L_{PIV} alongside individual contributions from the momentum, Re stress, and the pressure term.	58
5.16	$C_D(L_{PIV})$ for the two cylinders at medium and high WT settings in figure a). Momentum term $C_D(L_{PIV})$ contribution for the two cylinders at medium and high WT settings in figure b).	59
6.1	$C_D(AR)$ for selected cylinders obtained with a balance compared to results from literature.	62
6.2	$C_D(AR)$ for selected cylinders with the same diameter at two different Re	63
6.3	$C_D(AR)$ from different sources. Results from PIV were taken at $L_{PIV} = 10$	64
6.4	Dynamic pressure distributing behind cylinders of various AR at $L_{PIV} = 10$ or close to 10.	64
6.5	$C_D(L)$ for cylinders of the same AR , overlaid are the results from literature.	65
6.6	$DR(L)$ for cylinders of the same AR	66
6.7	DR as a function of distance for the case where there was the same leading cylinder and the distance between them being nondimensionalized by the leading diameter L_{lead} in a) and trailing diameter L_{trail} in b).	67
6.8	DR as a function of distance for the case where there was the same leading cylinder and the distance between them being nondimensionalized by the leading diameter L_{lead} in a) and trailing diameter L_{trail} in b).	68
6.9	DR as a function of distance for the case where there was the same trailing cylinder and the distance between them being nondimensionalized by the trailing diameter L_{trail} in a) and leading diameter L_{lead} in b).	69
6.10	DR as a function of distance for the case where there was the same trailing cylinder and the distance between them being nondimensionalized by the trailing diameter L_{trail} in a) and leading diameter L_{lead} in b).	70
6.11	DR as a function of distance for the case where there was the same leading cylinder and the distance between them being nondimensionalized by the leading diameter L_{lead} in a) and trailing diameter L_{trail} in b). With balance data overlaid with PIV measurements.	71
6.12	Images of the wake behind cylinders in tandem. In all cases, the leading cylinder was $AR = 4$, $d = 5$ cm. All images were taken at the same distance of 18 cm behind the trailing cylinder center.	72

List of Tables

2.1	Comparison of the reattachment distance at various AR from multiple sources.	8
4.1	Baseline Cylinders	41
5.1	Average freestream velocities obtained with PIV and Pitot tube for the three different WT settings.	50
5.2	Comparison between C_D results obtained with PIV and literature.	60

Nomenclature

Abbreviations

Abbreviation	Definition
BL	Boundary layer
CFD	Computational fluid dynamics
CVA	Control volume approach
CV	Control volume
DOF	Depth of field
FOV	Field of view
FDM	Fused Deposition Modeling
LES	Large eddy simulation
MSLS	Masked Stereolithography Apparatus
NS	Navier-Stokes
PIV	Particle image velocimetry
RoF	Ring of Fire
RMS	Root mean square
St	Strouhal number
TPU	programmable timing unit
WT	Wind tunnel

Symbols

Symbol	Definition	Unit
A	Projected frontal area of the cylinder	$[m^2]$
AR	Cylinder aspect ratio	$[-]$
C	Projected area of the wind tunnel cross-section	$[m^2]$
C_D	Coefficient of drag	$[-]$
$C_{D,c}$	Corrected coefficient of drag	$[-]$
C_p	Pressure coefficient	$[-]$
c_{len}	Characteristic length of the wake	$[m]$
D	Cylinder diameter	$[m]$
$D_{leading}$	Leading cylinder diameter	$[m]$
DR	Drag reduction	$[\%]$
$D_{trailing}$	Trailing cylinder diameter	$[m]$
d/D	Diameter ratio	$[-]$
d_{ap}	Diameter of the lens aperture	$[m]$
d_i	Distance between the sensor and the lens	$[m]$
d_o	Distance between the sensor and the object	$[m]$
d_p	Diameter of the tracer particle	$[m]$
d_τ	Diameter of the tracer particle on the camera sensor	$[m]$
d_{diff}	Diameter of diffraction of the tracer particle	$[m]$
F	Total aerodynamic force	$[N]$
F_{aero}	Combined aerodynamic force	$[N]$
F_D	Aerodynamic drag force	$[N]$
f	Lens focal length	$[m]$
$f\#$	Lens f-stop	$[-]$

Symbol	Definition	Unit
H	Cylinder height	[m]
$H_{leading}$	Leading cylinder height	[m]
$H_{trailing}$	Trailing cylinder height	[m]
k_w	streamwise turbulent kinetic energy	$[m^2/s^2]$
L	Pitch ratio	[/]
L_{char}	Characteristic flow length	[m]
L_{CR}	Critical pitch ratio	[/]
$L_{leading}$	Distance nondimensionalized by the leading cylinder diameter	[/]
$L_{trailing}$	Distance nondimensionalized by the trailing cylinder diameter	[/]
M	Magnification factor	[/]
R	Reactive force	[N]
Re	Reynolds number	[/]
Re_{crit}	Critical Reynolds number	[/]
S	Projected area of the cylinder	$[m^2]$
S_k	Particle Stokes number	[/]
St	Strouhal number	[/]
U	Fluid flow velocity	[m/s]
V	Particle velocity	[m/s]
v	Freestream velocity	[m/s]
w	Laser sheet thickness	[m]
Δt	Pulse separation time	[s]
ΔV	The change between particle and flow velocity	[m/s]
Δv	Reference flow velocity	[m/s]
δ	Shoulder angle	[°]
δt	Laser pulse width	[s]
δz	Width of the focus plane	[m]
ϵ	Empirical blockage constant	[/]
ϵ_{rand}	Velocity random error	[m/s]
ϵ_{resid}	Residual of the least squares method	[px]
λ	Laser light wavelength	[nm]
μ	Dynamic viscosity	[kg/ms]
ν	Kinematic viscosity	$[m^2/s]$
ρ	Density	$[kg/m^3]$
ρ_p	Density of the tracker particle	$[kg/m^3]$
ρ_f	Density of the fluid	$[kg/m^3]$
σ	std. deviation of the freestream velocity component	[m/s]
τ_p	Particle response time	[s]
τ_f	Flow characteristic time	[s]

1

Introduction

Motivation for this thesis comes from the field of cycling aerodynamics.

As with any sport performed at an elite level, there is a constant need for improvement. Among others, it comes from a better understanding of the athletics body, optimizing power transfer, and reducing energy losses due to interactions with air. The last one is especially important at a professional level since the naturally unaerodynamic shape of the cyclist-bicycle system greatly rewards those who master it and allows for some compensation for a less favorable body physique with a better riding technique.

One example of where aerodynamics plays a visible role is the sprint lead out before the race finish. This is where a cycling formation forms around a kilometer before the end of a race. It consists of the main sprinter and one or two assistants before him, forming a lead-out train. Since cyclists can only perform at their peak wattage for a couple of seconds, it was discovered that the optimal strategy to give the strongest rider a better chance of winning was to give him assistants who ride in front of him. They would sacrifice their chance of winning to perform at their pick wattage a couple of hundred meters before the end. This way, the sprinter is sheltered from the wind in their wake, reducing required power and energy losses. Once the last assistant would not be able to keep the required output, he would move away and allow the sprinter to unleash his power in the final meters.

Multiple factors, like their power output and riding technique, determine the best-assisting cyclists besides aerodynamics. However, the following question remains. Looking purely from an aerodynamics perspective, for a given trailing cyclist, what properties of the leading cyclist would be optimal for the trailing cyclist's drag reduction? Due to the cyclist's highly un-aerodynamic bluff body shape, the flow topology is very complex and irregular. Small changes in posture result in a non-linearly proportional flow response and drag force. Combined with numerous geometric degrees of freedom that could be defined on a cyclist, performing one variable at a time experimental campaign is impractical. Therefore, a different approach needs to be undertaken.

Since this is the first study in this investigation, cylinders will be used as bluff bodies due to their limited degrees of freedom. A comprehensive study of cylinders in tandem will be performed, emphasizing aerodynamic drag. Measurements will be performed with two measurement techniques: balance measurements and particle image velocimetry (PIV). The first one will be used as a baseline due to its low uncertainty, while PIV will be used alongside as a proof of concept to see if it can be used for the study of trailing bodies in more detail in the future.

The subsequent chapters of this thesis are organized as follows: Chapter 2 presents the literature review on the aerodynamics of cylinders in isolation and tandem and finishes with the research objective. Chapter 3 provides an overview of the PIV measurement technique and the control volume approach. Chapter 4 focuses on the experimental setup, followed by a chapter on data reduction and results. The thesis is concluded with the conclusion in chapter 7.

2

Cylinder Aerodynamics

The present chapter is structured into two subsections. The first subsection focuses on the flow topology around isolated cylinders and its consequent impact on the coefficient of drag C_D , equation 2.1. It is defined as the ratio between the aerodynamic drag force F_D and the dynamic pressure times the frontal area of a cylinder A , where ρ and v are density and velocity of the freestream. This analysis is conducted for a nominally two-dimensional flow, as well as on a cylinder of finite height, where the influence of three-dimensional features is more dominant.

$$C_D = \frac{F_D}{\frac{1}{2}\rho v^2 A} \quad (2.1)$$

In the second subsection, the same flow characteristics are studied in the case of two cylinders arranged in tandem, with an initial investigation of the scenario where the cylinders have an infinite height, followed by an examination of a more practical case of finite height cylinders.

The motivation behind this approach is to introduce complexity and relevant governing parameters progressively.

2.1. Isolated Cylinder

2.1.1. Flow Topology Around a Cylinder of Infinite Height

The most basic form of a flow around a cylinder is represented by that of an infinite cylinder, where the aspect ratio AR , defined as the ratio between the cylinder height H and its diameter D in Equation 2.2, is large enough such that the flow can be considered nominally two dimensional.

$$AR = \frac{H}{D} \quad (2.2)$$

Rayleigh (F.R.S. 1915) was the first to utilize dimensionless analyses and introduce the Reynolds number (Re) to study cylinder flows. The Re , equation 2.3 is defined as the ratio of momentum to viscous forces, with D representing the cylinder diameter, v representing the freestream velocity, and ν representing the kinematic viscosity. Subsequent research confirmed that the Re could be considered the governing parameter for flow around a cylinder in an idealized, disturbance-free environment (M. M. Zdravkovich 1997). However, in practical situations, the flow can be influenced to varying degrees by the onset of disturbances. Notably, influential parameters that can affect the flow include turbulence, surface roughness, and transverse and streamwise oscillations (M. Zdravkovich and Pridden 1977).

$$Re = \frac{v D}{\nu} \quad (2.3)$$

M. M. Zdravkovich, in his work (M. Zdravkovich and Pridden 1977), established a classification of four distinctive flow regions that emerge in the vicinity of a two-dimensional cylinder. As illustrated in Figure 2.1 below, these regions comprise the decelerated flow region (1), the boundary layer development region (2), the displaced flow regions (3), and the wake region (4).

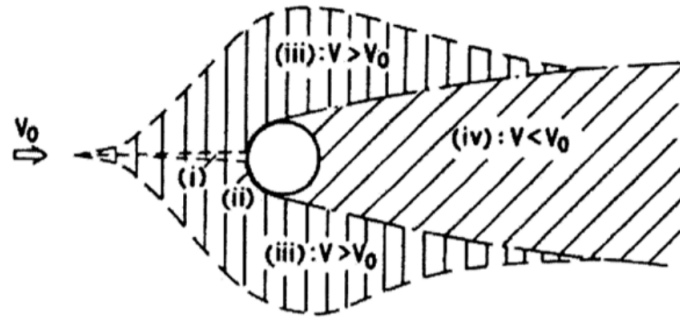


Figure 2.1: Distinct flow regions around a two dimensional cylinder (M. Zdravkovich and Pridden 1977).

Of the four identified regions, the boundary layer, and wake regions are particularly noteworthy. Downstream of the stagnation point, the flow initially experiences a favorable pressure gradient, followed by an adverse pressure gradient. Depending on the value of Re , the flow may either remain attached or separate, leading to the formation of a free shear layer and the wake. The position at which the flow transitions from laminar to turbulent also significantly affects the flow topology. In this manner, Zdravkovich (M. Zdravkovich and Pridden 1977) roughly defined four regions depending on where the transition occurs, as depicted in Figure 2.2. In the case of low Re , but where the flow already detaches, the transition occurs from laminar to turbulent in the separated shear layer (a). As Re increases, the transition point moves upstream. The transition occurs in the free shear layer emanating from the detached boundary layer (BL) before the wake is fully formed (b). This flow regime is often referred to as subcritical. In Region c, the flow transitions from laminar to turbulent within the BL , and the flow regime is considered critical from this point onward. As Re increases even further, the transition point moves toward the stagnation point, representing the final stage where the flow is turbulent everywhere (d).

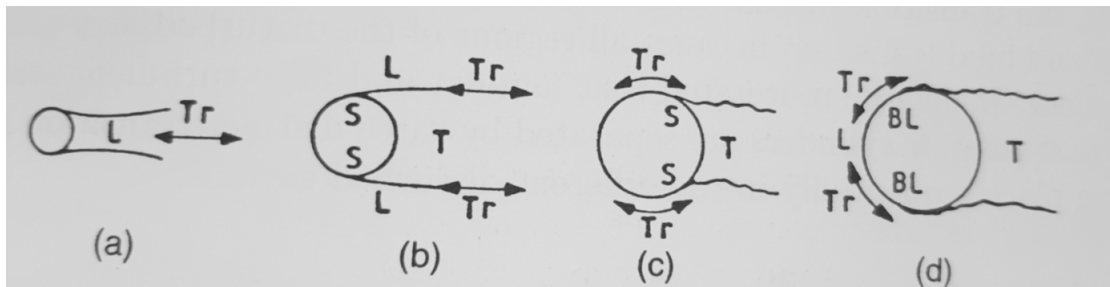


Figure 2.2: Illustration of the four transitional regions from laminar to turbulent flow. (L) laminar flow, (T) turbulent flow, (Tr) transition, (S) point of separation (M. Zdravkovich and Pridden 1977).

Several flow subdivisions based on the Reynolds number Re have been proposed in the literature. One such classification, often cited, is that of (Lienhard et al. 1966), depicted in Figure 2.3. At very low Re below 4 – 5, the flow remains laminar throughout and is dominated by viscous effects. The BL remains attached on the whole perimeter of the cylinder (a). As Re increases to around 40, the boundary layer detaches, and two symmetrical recirculation zones appear in the wake (b). As the Re number increases, alternating eddies first develop in the laminar wake downstream due to laminar wake instabilities (Kovasznay 1949). Later in this stage, the flow starts to transition from laminar to turbulent inside the wake. This transition moves further upstream, affecting eddies up until they become turbulent already during their formation (b) and (c) (M. M. Zdravkovich 1997). At this stage, the mechanism behind the eddy formation changes from the above-mentioned laminar flow instabilities to turbulent eddy roll-up and shedding mode from the cylinder (M. M. Zdravkovich 1997). This change is reflected in the eddy shedding frequency, denoted by the Strouhal number. St is defined in the equation 2.1.1

where f is the shedding frequency, D cylinder diameter, and v free stream velocity.

$$St = \frac{fD}{v}$$

At this point, the transition waves appear in the free shear layer, which later roll into a discrete vortex. It later becomes turbulent and moves off the cylinder as a part of alternating shedding eddies (M. M. Zdravkovich 1997). (Gerrard 1966) explained this alternating eddy formation by saying that as the forming vortex grows in size and vorticity, it will draw the smaller forming vortex from the opposite side towards it. This second vortex will cut off the larger one, which will now become a free vortex that will propagate downstream, where it will later burst into turbulence depending on the Re . This flow regime remains dominant until around $5.3 \cdot 10^5$, where there is an almost discontinuous drop in C_D and from where the flow is referred to as supercritical.

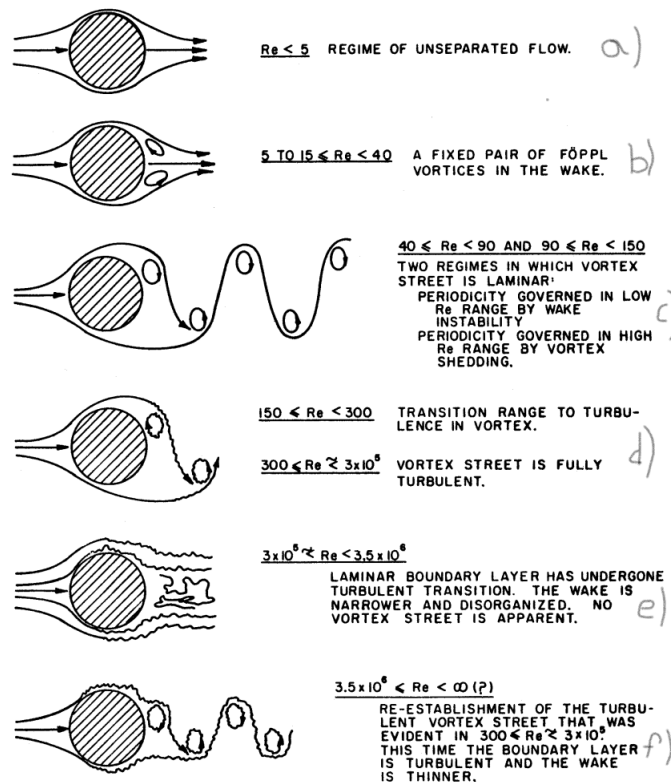


Figure 2.3: Different flow regimes around a nominally two-dimensional cylinder as a function of the Re (Lienhard et al. 1966).

The first drop, which can be seen in the TrBI0 region in Figure 2.4, occurs due to flow transition coming close to the separation line on the cylinder. This disturbs the near wake and delays the vortex formation (M. M. Zdravkovich 1997). This is then followed by an additional discrete drop in C_D due to the formation of the laminar separation bubble (TrBI1). Here the detached flow of the laminar boundary layer undergoes the transition to turbulent and reattaches shortly downstream before the subsequent turbulent separation. This stage is then followed by the formation of the second laminar bubble on the opposite side as well (TrBI2). These two regions are sensitive to disturbances and might not be present where influential parameters, like surface roughness, are significant (M. M. Zdravkovich 1997). At a higher Re , the disruption and fragmentation of the bubbles appear before the regular vortex shedding reappears when the transition from laminar to turbulent occurs inside the boundary layer before the separation.

As the transition point moves towards the stagnation point, the flow is often considered to be in a turbulent regime. Here, as the Re increases, the flow features and the St should remain largely invariant,

although as (M. M. Zdravkovich 1997) mentored in his work, at a certain point the effects of compressibility or cavity (in water flows) become large enough where they become part of the governing parameters.

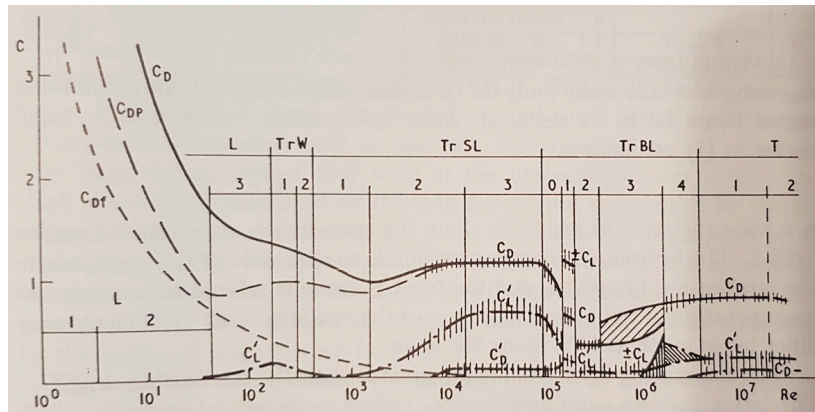


Figure 2.4: Coefficient of drag as a function of Re overlaid with information about different flow regions (M. M. Zdravkovich 1997).

The presented figures 2.4 and 2.5 indicate a noticeable variability in the coefficient of drag (C_D), particularly at the critical Reynolds number (Re_{crit}), which marks the transition from sub-critical to supercritical flow regimes. This variance is largely attributed to a host of influential parameters, the experimental setup, and the hysteresis effect observed in numerous investigations.

Among the influential parameters, three are worth looking at in more detail. Firstly, the impact of free-stream turbulence on the coefficient of drag is noteworthy, as an increase in turbulence levels has been shown to result in transition occurring at lower Reynolds numbers. This effect is likely to be the main reason for the deviation observed in the experimental results of Fage, as illustrated in Figure 2.5 (Rodríguez et al. 2015).

Cylinders with higher surface roughness will experience BL transition from laminar to turbulent sooner, resulting in Re_{crit} at lower Re . Additionally to that, the minimum C_D will increase (Rodríguez et al. 2015).

Thirdly, the effect of compressibility on the coefficient of drag is also noteworthy, as it has been observed to shift the critical Reynolds number towards higher values, leading to an increase in drag at all Re (Rodríguez et al. 2015). While compressibility effects are typically assumed to be negligible below Mach number $Ma = 0.4$, Polhamus (Polhamus 1981) reported that these effects can already be detected at around $Ma = 0.2$.

Regardless, several observations can be made from the data presented in the figures. In the laminar regime, there is a steep decrease in the coefficient of drag as the Reynolds number increases, followed by a plateau-like region where the C_D remains relatively constant and where there is a formation of turbulent eddies. This trend continues until a critical Reynolds number of approximately $5.3 \cdot 10^5$ is reached. Beyond this, there is a sharp drop in the C_D due to the transition from subcritical to supercritical flow regimes. In the turbulent regime, the C_D gradually increases again but remains lower than the constant value observed in the plateau region.

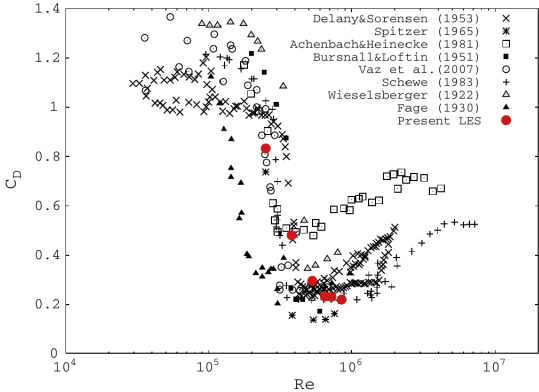


Figure 2.5: $C_D(Re)$ comparison between different experimental studies and one large eddy simulation (LES) (Rodríguez et al. 2015).

2.1.2. Flow Topology Around a Cylinder of Finite Height

Cylinders of infinite height have been the subject of numerous studies. However, the investigation of the low aspect ratio cylinders with an exposed free end have received comparatively little attention in the academic literature.

In the work (Pattenden, Turnock, and Zhang 2005), the authors examined the flow around a wall-mounted cylinder with the aspect ratio of one. They utilized various measurement techniques from unsteady surface measurements, particle image velocimetry (PIV), and surface flow visualization to identify mean flow features, which can be seen in Figure 2.6. They also distinguished three areas of particular interest:

- the horseshoe vortex system upstream.
- flow over the free-end.
- wake region.

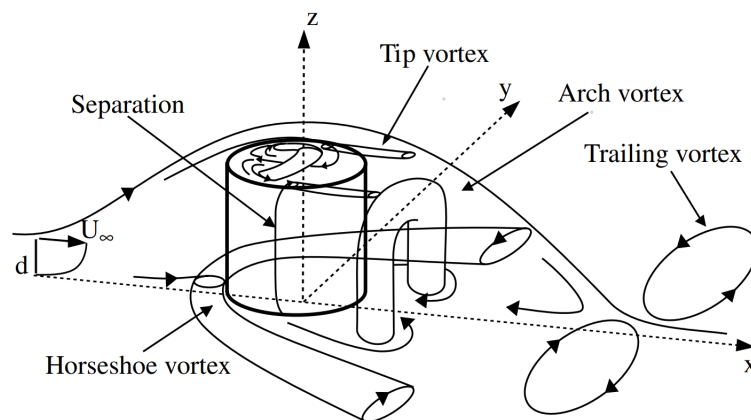


Figure 2.6: Scheme of the flow topology around a low AR cylinder (Pattenden, Turnock, and Zhang 2005).

Just upstream of the cylinder at the base, a vortex system develops, Figure 2.7, with one main larger clockwise rotating vortex, two smaller ones between it and the ground, and one rolling of the cylinder edge (Baker 1980).

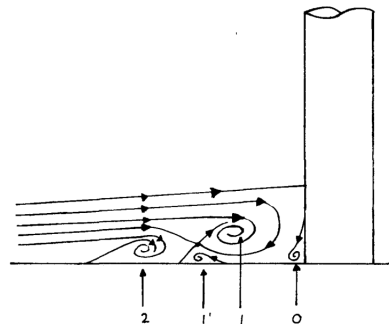


Figure 2.7: Visualisation of the upstream horseshoe vortex system (Baker 1980).

This pattern was similarly observed by (Pattenden, Turnock, and Zhang 2005) with surface flow visualization and partially also PIV (the bottom vortices were not distinguishable due to resolution and proximity to the ground, but downwash observed just above it does indicate the potential existence of one).

Interestingly, the position of the main vortex, 1 in figure 2.7, is unsteady, varying in size and position of formation and decay. Varying positions of this vortex's core upstream of the cylinder gathered from

PIV images can be seen in Figure 2.8. Here the $\frac{x}{d}$ and $\frac{z}{d}$ represent a non dimensional distance from the cylinder centre and the ground (centre of the coordinate system in Figure 2.6).

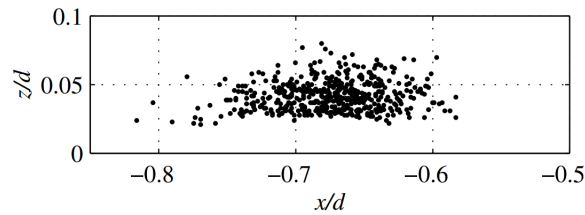


Figure 2.8: Various positions of the main horseshoe vortex core gathered from PIV images (Pattenden, Turnock, and Zhang 2005).

As this clockwise rotating vortex rolls around the sides of the cylinder it can now be seen in figure 2.6 as the horseshoe vortex. At a distance of $x/d = 0.5$ this horseshoe vortex is already positioned at $y/d \approx \pm 1$ sideways, indicating that there is also a large perturbation of the flow in the side-way direction.

On the top side of the cylinder, the flow is highly three-dimensional. This includes separation at the sharp leading edge followed by the region of reversed flow and two foci, and reattachment.

From the sides of the cylinder free end, a pair of counter-rotating vortices form. They stay at a relatively similar position until $0.5 x/d$ downstream where they start to move down towards the ground. This is likely due to downwash behind the cylinder. As they move further on, they expand and later merge with the vorticity from the flow converging outside the separation bubble (Pattenden, Turnock, and Zhang 2005).

In the case of cylinders with finite height, the flow separation on the sides occurs sooner than in the case of infinite cylinders. This is often attributed to the higher back pressure from the flow entering over the free end. (Pattenden, Turnock, and Zhang 2005) visualized the separation of the truncated cylinder once with laminar BL and secondly with the tripped turbulent BL. They found that in the case of the laminar BL, it occurred 10° sooner than at an infinite cylinder where it separates at 70° . Separation at various heights also varied with 5° delay at the bottom and top edge due to the oblique flow. Separation occurs similarly 20° sooner for the equivalent example with tripped BL, where the flow separates at 80° for a nominally two-dimensional flow. The study also found that tripping the BL and delaying the separation did not affect the flow's topology.

Separated flow from the sides encloses a recirculating region behind the cylinder until it meets the descending tip vortices from the free-end when those reach the ground plane, as discussed earlier. (Okamoto and Sunabashiri 1992) found that recirculating length reduces with aspect ratio. While later studies more or less confirmed this, they still vary in the distance. This could be partly due to flow conditions, different measurement techniques and approaches used to measure this distance. The comparison of some studies can be found in the Table 2.1.

Research	Cylinder AR	reattachment distance $x/$
(Okamoto and Sunabashiri 1992)	1	2.9
(Pattenden, Turnock, and Zhang 2005)	1	1.6
(Leder 2003)	2	2.2
(Sumner, Heseltine, and Dansereau 2004)	3	3

Table 2.1: Comparison of the reattachment distance at various AR from multiple sources.

In the recirculating region, there is an area of reverse flow which wraps into an arch vortex just behind the cylinder, Figure 2.6.

At the bottom of a cylinder, close to the wall, the reverse flow impinging on the curved face of the cylinder causes the creation of a small pair of clockwise rotating vortices parallel to the free stream direction (Pattenden, Turnock, and Zhang 2005).

During their research, (Pattenden, Turnock, and Zhang 2005) produced planar images of the wake at different distances from the cylinder, Figure 2.9. What is noticeable the most are the two tip vortices

and their trajectories. As they move, they slowly expand and merge with vorticity from the detached flow shear layer. When they reach the ground, they start moving to the side.

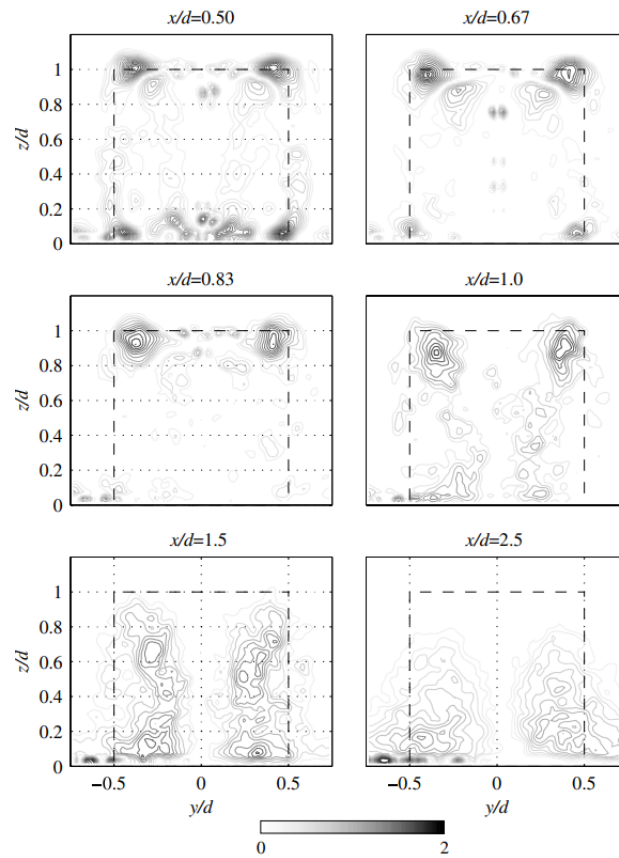


Figure 2.9: Vorticity distribution. PIV images of the wake were taken at various distances from the cylinder (Pattenden, Turnock, and Zhang 2005).

(Kawamura et al. 1984) investigated the effect of the BL size on the wall where the cylinder is mounted and found that the C_D decreases with the increase of BL, figure 2.10. This was in line with other research.

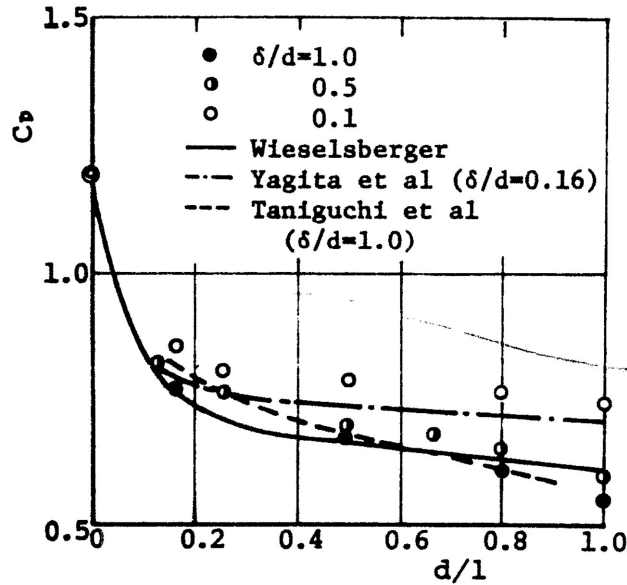


Figure 2.10: C_D as a function of aspect ratio, for different BL heights, $Re = 3, 2 \cdot 10^4$, (Kawamura et al. 1984).

It is important to note that the descriptions provided in this context primarily pertain to mean flow characteristics that are averaged over time. These features significantly differ from the flow topology observed at any given moment. The vorticity distribution in such cases is considerably more chaotic, and its spatial distribution is predominantly governed by the turbulent nature of the problem rather than exhibiting any discernible structural pattern. Several researchers have cautioned against relying on time-averaged models to investigate flows of this nature, as they may not provide sufficient accuracy in capturing the intricacies of such turbulent flows.

So far the focus has been on the two contrasting conditions: infinitely long cylinders that exhibit nominally two-dimensional flow features and the finite cylinder of aspect ratio 1, which exhibit a pronounced three-dimensional flow.

However, most real-world scenarios involve cylinders with aspect ratios that fall somewhere between these two extremes. (Sarode, Gai, and Ramesh 1981) investigate cylinders of various heights and found that C_D increases with an increase in AR . In their example, a cylinder with $AR = 10$ still experienced smaller C_D than that of an infinite one. This observation was confirmed by (Okamoto and Sunabashiri 1992), who got to the same conclusion, taking measurements of a cylinder of AR as high as 23. (Fox and West 1993) attributed lower drag to increased wake pressure caused by free-end disturbances. (Farivar 1981) in their research suggested that three-dimensional effects are only contained to a small part of the cylinder near the top. In one of their examples with the cylinder of $AR = 12.5$, they found that the base pressure would remain constant between the heights of $0.39 \leq y/h \leq 0.81$, which they would call suppressed two-dimensional flow, figure 2.11. In their research, they found the possible existence of three different vortex sets. In lower regions, vortices were shed at such a frequency for the St number to be comparable to that of a similar infinite cylinder.

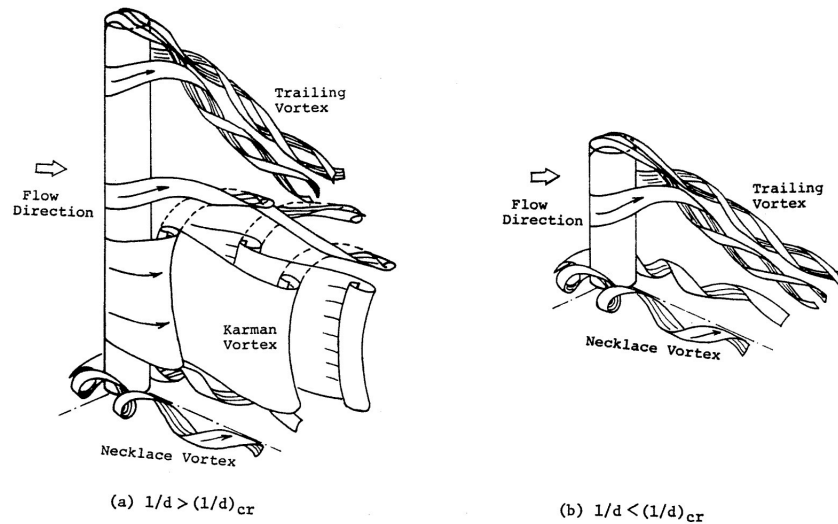


Figure 2.11: Model of the flow by (Kawamura et al. 1984), comparing two cylinders of finite height, showing the *suppressed two-dimensional flow* around cylinders with higher AR.

Figure 2.12 presents a comparative analysis of various experimental investigations of isolated finite height cylinders. As reported by previous research, the drag coefficient tends to increase with higher aspect ratios and eventually approaches the value obtained for an infinite cylinder. However, the observed results are subject to variations due to the presence of different influential parameters and variations in the experimental setup. None of the analyzed studies applied wind tunnel corrections, and they differed in the blockage ratio. Notably, the outcomes of Okamoto's study stand out as an outlier, which could be attributed to their different approach to determining C_D , which involved computing it from the pressure measurements on the cylinder's surface.

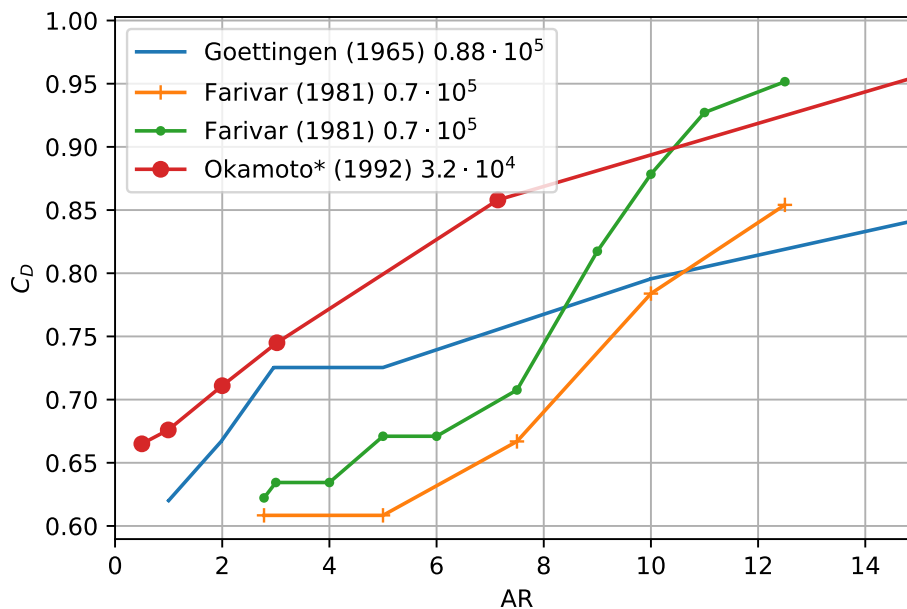


Figure 2.12: A comparison of various experimental studies investigating the drag coefficient (C_D) as a function of aspect ratio (AR). The corresponding Re at which the measurements were taken place can be seen in the legend.

2.2. Cylinders in Tandem

Two cylinders are in tandem when they are positioned one after another and parallel to the oncoming flow, where the trailing cylinder is submerged in the wake of a leading cylinder.

The ensuing flow topology and, notably for our purposes, the wake characteristics and drag exerted on a trailing cylinder are influenced by the following parameters:

- Pitch ratio L , defined as the distance between the centers of two cylinders, normalized by the leading cylinder diameter $D_{leading}$:

$$L = \frac{\text{distance between cylinder centres}}{D_{leading}} \quad (2.4)$$

- Reynolds number Re .
- Aspect ratio AR , defines ad the ratio between the cylinder height H and its diameter D :

$$AR = \frac{H}{D} \quad (2.5)$$

- Boundary layer of the ground plane.

The flow behaviour around two cylinders in tandem has been a subject of prior studies due to its resemblance and approximation of a wide range of engineering applications, including power lines, wires on bridges, and cylindrical towers. Along with the study of flow topology, a considerable focus has been placed on exploring the unsteady oscillations and evaluating the Strouhal number St due to its impact of unsteady loading on structures and acoustic implications. According to Sumner's review (Sumner 2010) of this field, the majority of research has concentrated on the study of two cylinders with infinite height and identical diameters. Therefore, the initial section of this discourse will be devoted to examining this simplest case, followed by the introduction of cylinders with varying diameters in subsequent parts.

2.2.1. Flow Topology Around Two Equal Infinite Cylinders in Tandem

If we now consider a case of two infinite cylinders with the same diameter, we can limit the number of independent parameters to pitch ratio L and the Re (Sumner 2010).

In the past different approaches have been undertaken in an attempt to classify the flow features observed when varying L and Re . Arguably the most useful, and also the one that has been adopted the most, is the classification based on observable flow patterns. In the works (Igarashi 1982) and (Igarashi 1984), the author, based on his and other research, proposed the following eight flow regimes that can be seen in Figure 2.13. Many have expended on it since or applied it to other variations of the two-cylinder problem, but this one is widely accepted.

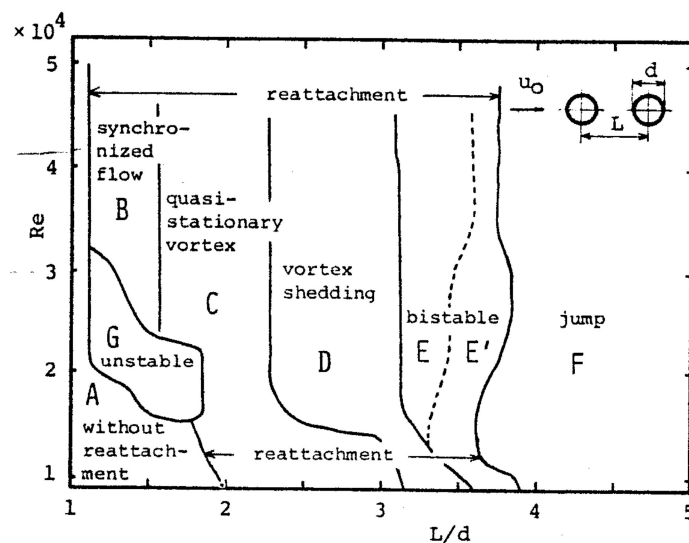


Figure 2.13: Flow pattern classification based on (Igarashi 1984).

Following (M. Zdravkovich 1987) the flow patterns in these eight flow regimes can be broadly joined together into three distinct groups:

- Extended body regime or single bluff-body behaviour.
- Reattachment regime or shear layer reattachment behaviour.
- Co-shedding regime or Kàrmàn vortex shedding from each cylinder.

These three types can be seen in Figure 2.14 below and will be explored in more detail now.

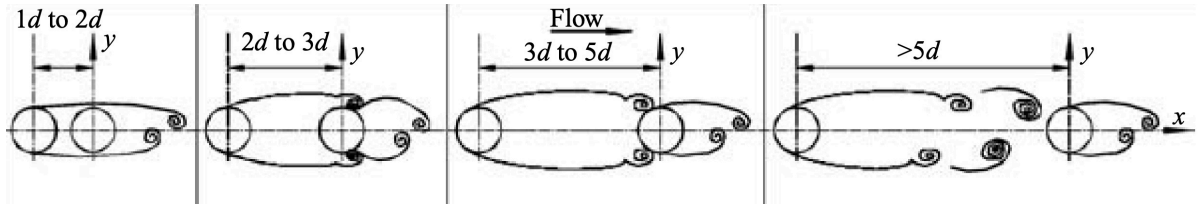


Figure 2.14: Flow subdivision based on flow topology. The extended body regime is located on the left side with further subdivision of the reattachment regime in the middle and co-shedding regime on the right (Y. Zhou and Yiu 2006).

Extended body regime

This is a region positioned roughly between $1 < L < 2$ and varies slightly with Re (M. Zdravkovich 1987),(Y. Zhou and Yiu 2006). The two cylinders are close enough such that the shear layer that separates from the leading cylinder has no choice but to enclose the trailing cylinders and rolls into Kàrmàn vortices behind, without reattaching on its surface (Sumner 2010). These vortices roll up closer to the cylinder, are more elongated, and the wake is narrower than in the case of an isolated cylinder (Lin, Yang, and Rockwell 2002). An example of the extended body regime can be seen in Figure 2.15.

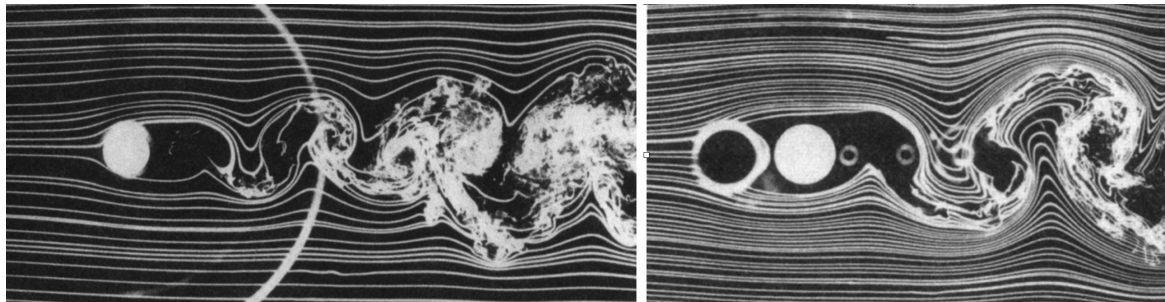


Figure 2.15: Comparison between the flow past an isolated cylinder at $Re = 3.0 \cdot 10^3$ and two cylinders in tandem $L = 1.25$ and $Re = 3.3 \cdot 10^3$ (Lars Ljungkrona and Bengt Sundén 1993).

Reattachment regime

For pitch ratios $1.2-1.8 < L < 3.4-3.8$ according to (M. Zdravkovich 1987) and $2 < L < 5$ from (Y. Zhou and Yiu 2006) the distance between the two cylinders is such that the shear layer separated from the leading cylinder can no longer enclose the trailing cylinder and therefore reattaches on its surface. (Lin, Yang, and Rockwell 2002) showed in their research a formation of eddies in the gap between the two cylinders which vary in their strength and behaviour. However, due to the sensitivity of this regime the research is still inconclusive (Sumner 2010). In the work of (Y. Zhou and Yiu 2006), authors made a further separation of the flow at $2 < L < 3$ and $3 < L < 5$. In the first case, they observed that the flow reattaches more often on the downstream side of the trailing cylinder, interfering with the boundary layer, which results in smaller and weaker vortices. They observed that the shear layer reattaches at the upstream side of the trailing cylinder at larger L and interferes less with the BL development, which results in stronger vortices (Sumner 2010). An example of the reattachment regime can be found in the following Figure 2.16.

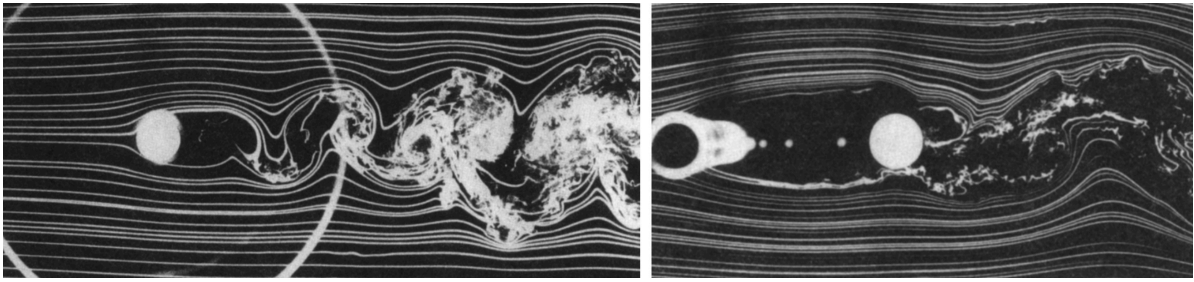


Figure 2.16: Comparison between the flow past an isolated cylinder at $Re = 3.0 \cdot 10^3$ and two cylinders in tandem $L = 4$ and $Re = 10 \cdot 10^3$ (Lars Ljungkrona and Bengt Sundén 1993).

Co-shedding regime

At pitch ratios higher than $L > 3.4\text{--}3.8$ (M. Zdravkovich 1987) or $L > 5$ according to (Y. Zhou and Yiu 2006) the distance is now large enough such that the trailing cylinder is no longer in the vortex formation zone of the leading one, and both cylinders shed their own Kàrmàn vortices (Sumner 2010). Shedding of the downstream vortices is triggered by the arrival and the impingement of the upstream vortices (Sumner 2010). Both are being shed at the same frequency. The oncoming vortices from the leading cylinder get distorted as they are forced around the trailing cylinder (Lin, Yang, and Rockwell 2002), and they merge with those being formed at the trailing one (Meneghini et al. 2001). These trailing Kàrmàn vortices form closer than those in the reattachment regime or from an isolated cylinder. (Y. Zhou and Yiu 2006) found that the vortex street is weaker and dissipates sooner, partially due to the aforementioned impinging process. Figure 2.17 shows an example of such a regime.

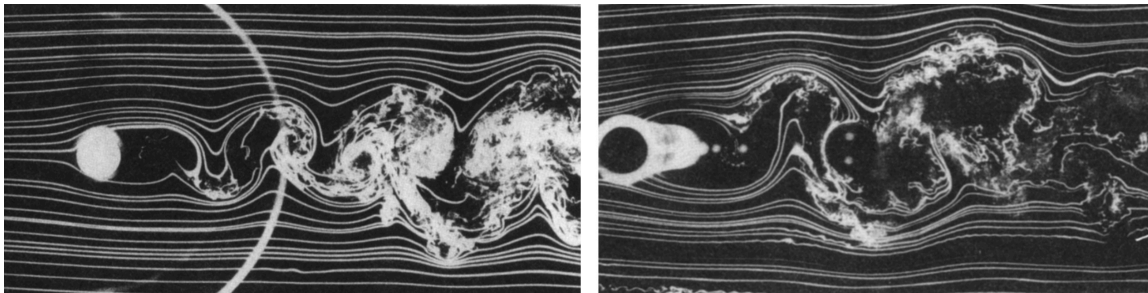


Figure 2.17: Comparison between the flow past an isolated cylinder at $Re = 3.0 \cdot 10^3$ and two cylinders in tandem $L = 4$ and $Re = 12 \cdot 10^3$ (Lars Ljungkrona and Bengt Sundén 1993).

One important parameter when discussing flow regimes is the critical pitch ratio L_{CR} . It denotes a point at which there is a sudden transition, jump, from the reattachment regime to the co-shedding one. It varies from L of 3 to 5, depending on the source, and it is sensitive to Re changes. This is why the distances between the two cylinders are the same in figures 2.16 and 2.17, but just a change in the Re resulted in a different flow regime. It was also observed by (M. Zdravkovich 1987) that L_{CR} experiences a hysteretic behavior. Interestingly (L. Ljungkrona, Norberg, and B. Sundén 1991) observed that L_{CR} follows the vortex formation length closely (Figure 2.18) and decreases considerably when turbulence is introduced.

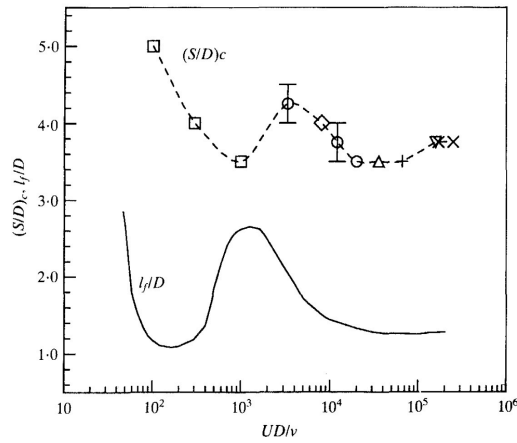


Figure 2.18: Critical pitch ratio (upper curve) and vortex formation length (bottom curve) (L. Ljungkröna, Norberg, and B. Sundén 1991).

Insightful visualization of the wake behind cylinders in tandem has been performed by (Y. Zhou and Yiu 2006) in Figure 2.19 and (Lin, Yang, and Rockwell 2002) in Figure 2.20. As previously mentioned, the vortices weaken more rapidly in the case of a co-shedding and extended body regime than in the reattachment regime, but the wake grows faster (Sumner 2010).

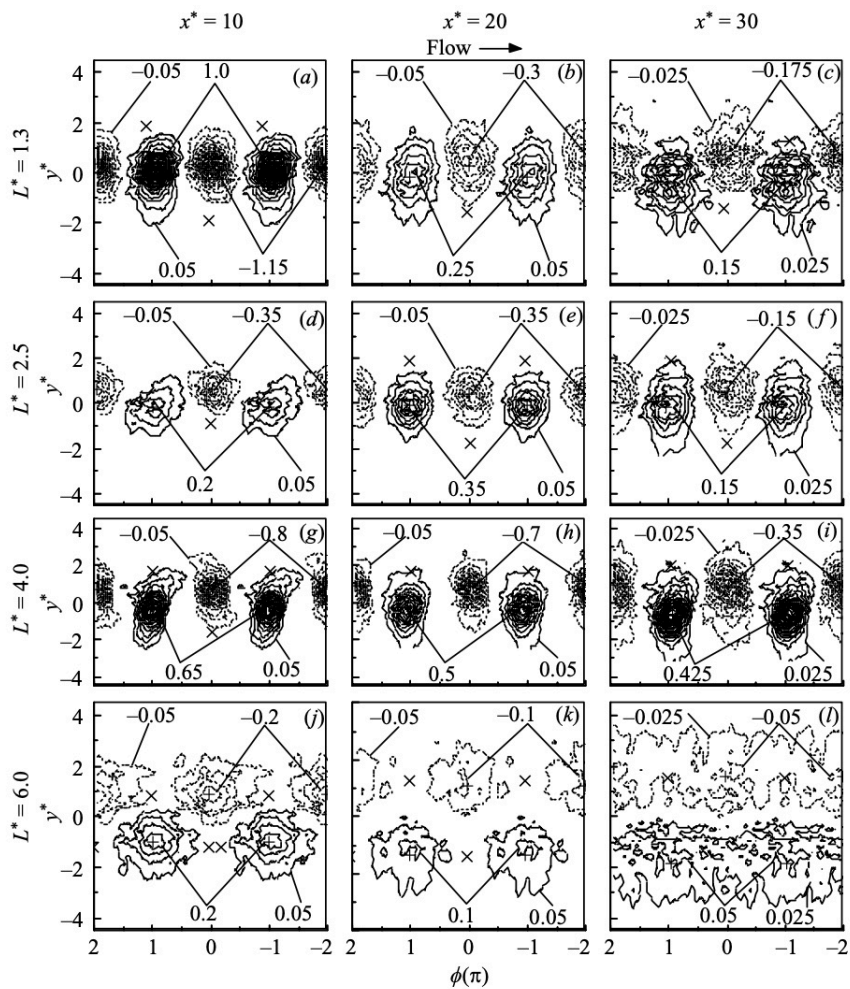


Figure 2.19: Phase average vorticity indicating progression of the Kármán vortices behind cylinders in tandem for different flow regimes due to varying pitch ratio (Y. Zhou and Yiu 2006).

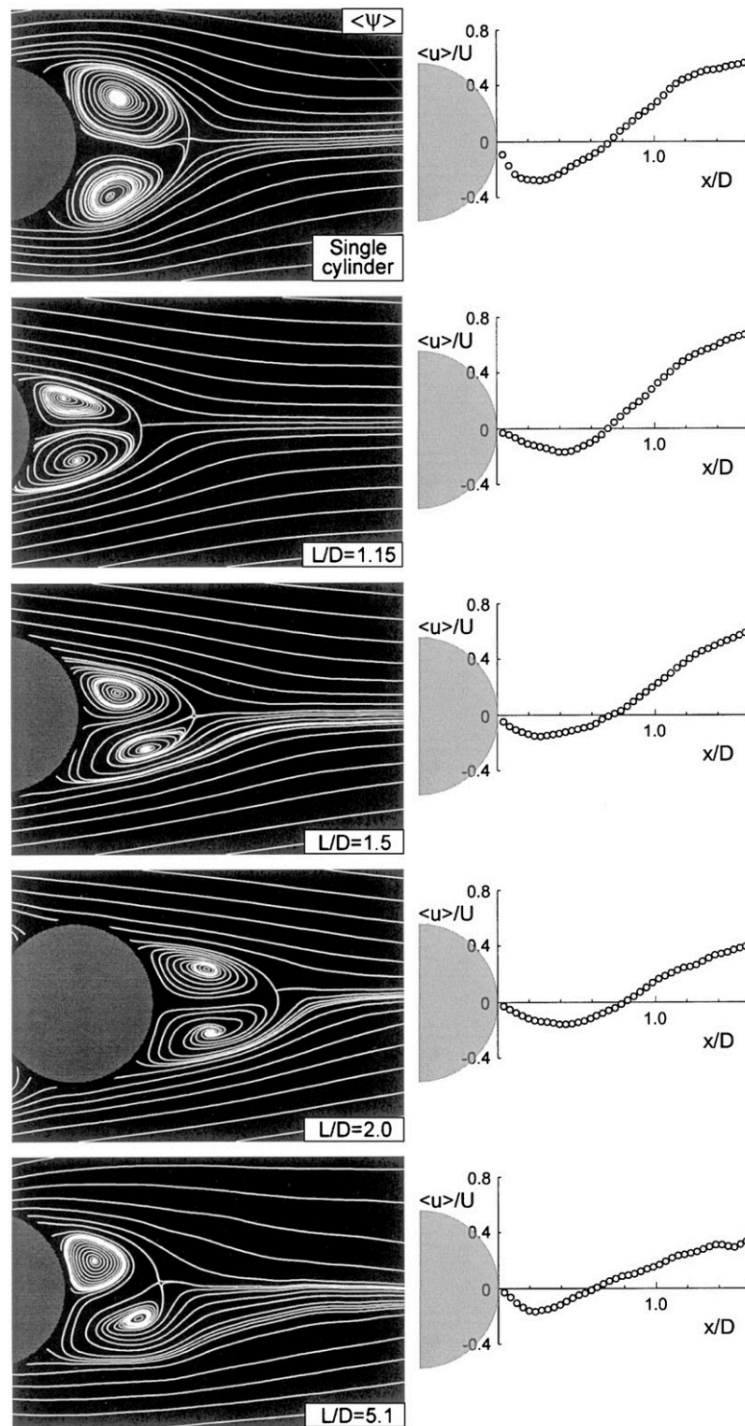


Figure 2.20: On the left, the patterns of the averaged streamlines are shown behind the cylinder indicating the variable recirculation region, and on the right average streamwise velocity as a function of the distance on the mid-plane (L. Ljungkröna, Norberg, and B. Sundén 1991).

2.2.2. Effects on Drag

As we have seen, the flow topology highly depends on the pitch ratio and the Re . The figure 2.21 shows the variation of the drag force C_D as a function of the pitch ratio L .

Observation from the figure can be summarised as follows:

- Both cylinders experience drag reduction when put in tandem.
- In the extended body regime, the trailing cylinder experiences thrust force.

- At the critical pitch ratio L_{CR} , there is a sudden jump in C_D due to flow transitioning from the reattachment regime to the co-shading regime.
- As L increases further, the drag of the two cylinders converges to that of an isolated cylinder.

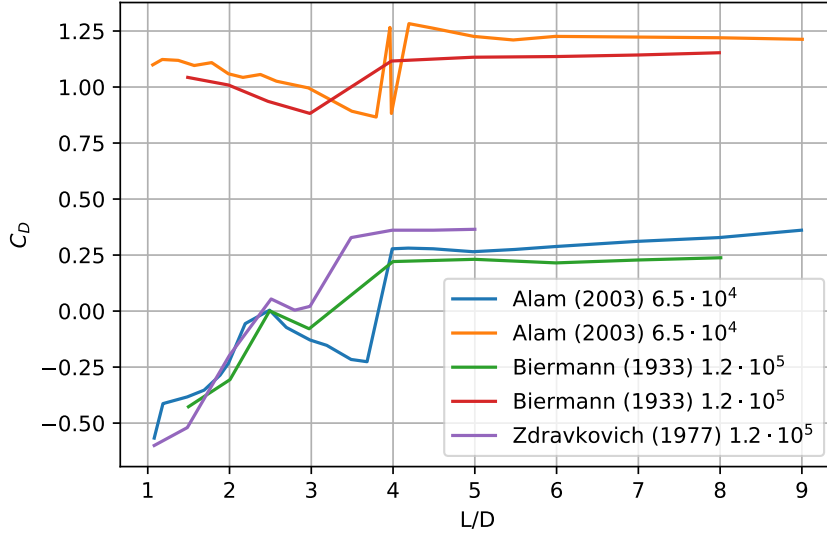


Figure 2.21: C_D as a function of the pitch ratio. The upper curves represent C_D of the leading cylinder, and the bottom curves that of a trailing cylinder (M. Alam et al. 2003), (Mittal, Kumar, and Raghuvanshi 1997), (M. Zdravkovich and Pridden 1977), (Biermann and Herrstein 1933).

2.2.3. Flow Topology Around Two Infinite Cylinders of Different Diameters in Tandem

Decoupling the two cylinders in terms of their diameters introduces an additional significant parameter known as the diameter ratio d/D . The diameter ratio is defined as the ratio of the diameter of the leading cylinder ($D_{leading}$) to that of the trailing cylinder ($D_{trailing}$):

$$d/D = \frac{D_{leading}}{D_{trailing}} \quad (2.6)$$

It is worth noting that the research on this type of flow with decoupled cylinder diameters has been relatively limited, with only a few comprehensive investigations conducted thus far. Among the notable studies in this area are (Mahbub Alam and Y. Zhou 2008) and (L. Wang, M. M. Alam, and Yu Zhou 2018). The first research focused on two cylinders of $AR = 14$ at a fixed longitudinal spacing $L = 5.5$ with a varying $0.24 < d/D < 1$. The latter investigated a similar setup but varied the pitch ratio for $1 < L < 8$. All cases in both studies had $d/D < 1$, which means that the leading cylinders were smaller than the trailing, except for the $d/D = 1$ where they were the same.

(L. Wang, M. M. Alam, and Yu Zhou 2018) found that as the diameter ratio increases, the shedding frequency of the leading cylinder increases and converges towards that of an isolated cylinder. In contrast, at the same time, the St of the trailing cylinder decreases. Their results can be observed in Figure 2.22. Authors argue that the first part is due to the upstream effects of the trailing cylinder slowing down flow around the leading one and a latter decrease in trailing cylinder St due to reduced incident flow velocity. (L. Wang, M. M. Alam, and Yu Zhou 2018) observed a similar trend.

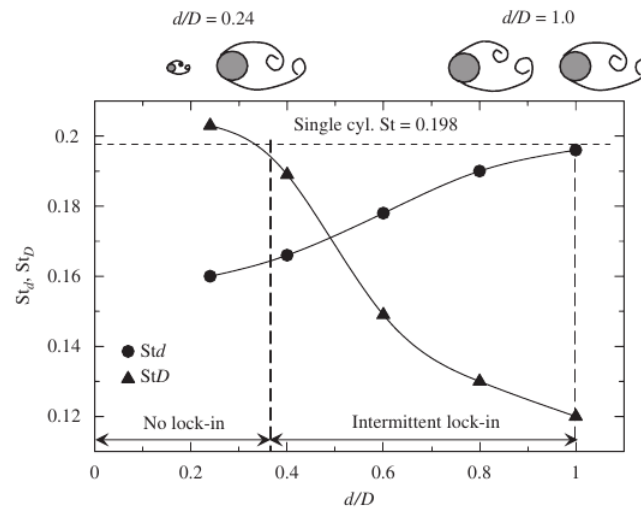


Figure 2.22: St as function of d/D for leading and trailing cylinder (Mahbub Alam and Y. Zhou 2008). The cylinders were in the Co-shedding regime at $L = 5.5$.

Bellow $d/D \geq 4$, excitation of the upstream cylinder was too weak to influence the shedding of the trailing cylinder. At $0.4 \leq d/D < 1$ (Mahbub Alam and Y. Zhou 2008) observed intermittent locking and $d/D = 1$ almost complete locking, which means that quasi-periodic impingement of the upstream vortices locked in vortex shedding of the trailing cylinder. Downstream of the tandem cylinders (Mahbub Alam and Y. Zhou 2008) detected two dominant frequency and vortex shedding structures, one associated with the trailing cylinders (higher f , after $d/D \geq 4$), and the second to the leading cylinder (lower f , after $d/D \geq 4$). They noticed that after the distance of $x/D > 5$, the higher f vorticity sheet morphed into low f vorticity due to the inherent instabilities of the wake. After that, only the dominant f remains (Mahbub Alam and Y. Zhou 2008). Visualization of this effect can be seen in figure 2.23.

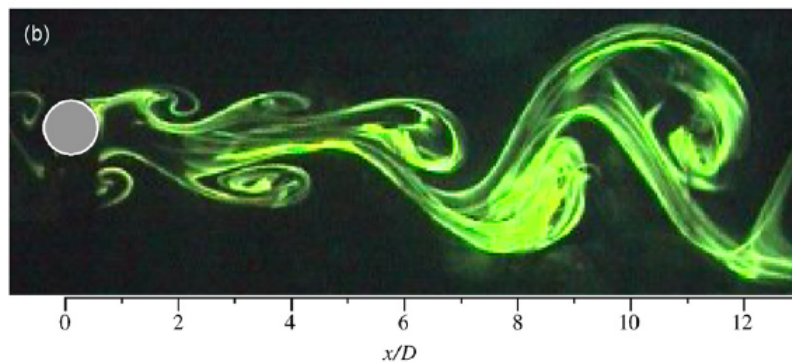


Figure 2.23: Visualisation of the flow behind trailing cylinders. Before $x/D < 5$, both lower and higher f shedding vorticity can be observed, but after that, only the dominant remains (Mahbub Alam and Y. Zhou 2008).

As d/D increases, the thickness of the wake in the gap between the cylinders increases as well. This can be inferred from figure 2.24, which presents normalized time-averaged streamwise velocity in the gap at $x/D = -1$ (a) and behind the cylinder at $x/D = 1$ (b) and at $x/D = 4$ (c) for different d/D . From these results, it can also be inferred that for smaller d/D , the velocity recovery rate is higher, which according to authors, implies higher entrainment rate due to stronger vorticity.

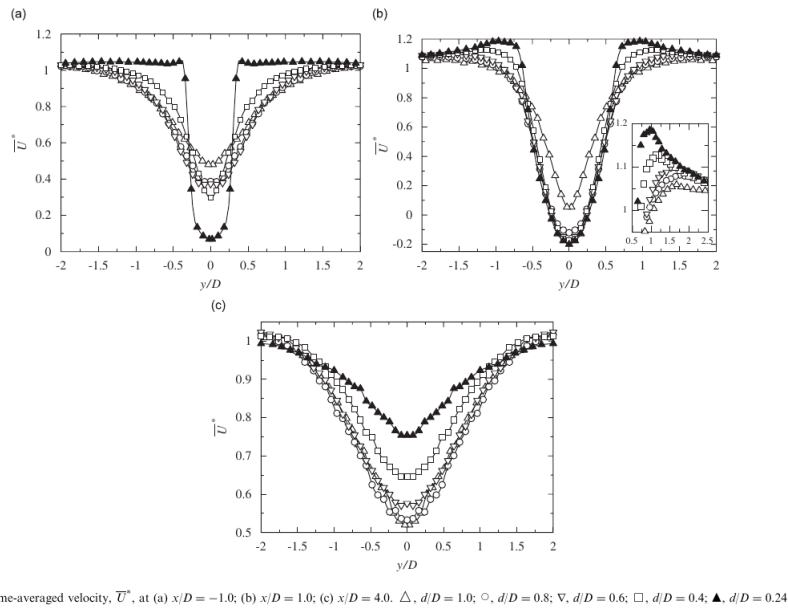


Figure 2.24: Normalised time averaged streamwise velocity in the gap at $x/D = -1$ (a) and behind the cylinder at $x/D = 1$ (b) and $x/D = 4$ (c), for different d/D (Mahbub Alam and Y. Zhou 2008).

Figure 2.25 shows the C_D of the trailing cylinder as a function of d/D . It can be observed that the drag reduces as d/D increases. (Mahbub Alam and Y. Zhou 2008) attributed this to more stagnant fluid and smaller dynamic pressure between the trailing cylinder. Contrarily, the RMS values of the drag and lift force increase due to stronger impingement of the upstream vortices on the trailing cylinder.

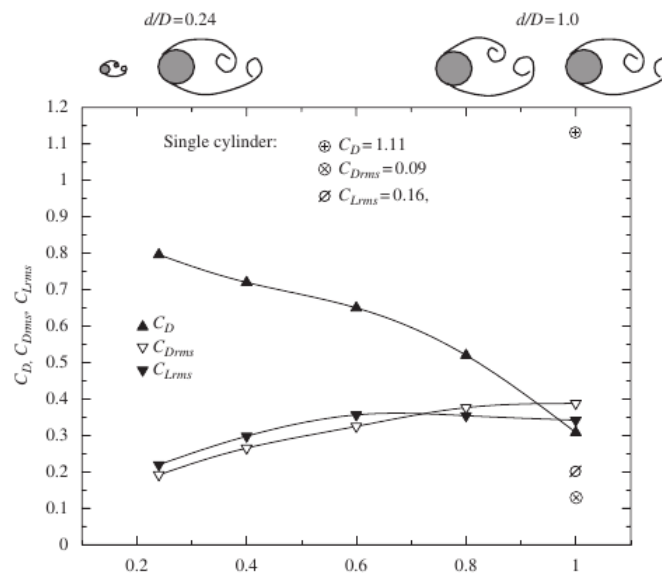


Fig. 18. Dependence on d/D of C_D , $C_{D,rms}$ and $C_{L,rms}$ on the downstream cylinder.

Figure 2.25: C_D of a trailing cylinder as a function of d/D for cylinders in tandem at $l = 5.5$ (Mahbub Alam and Y. Zhou 2008).

Previous observations about the flow are for the co-shading flow regime. (L. Wang, M. M. Alam, and Yu Zhou 2018) came to the same conclusion, but the varying L also allowed for an investigation of the reattachment regime. There, the flow topology and vortex formation strongly depend on the location of the free shear layer reattachment on the trailing cylinder. C_D as a function of L and d/D can be seen in figure 2.26.

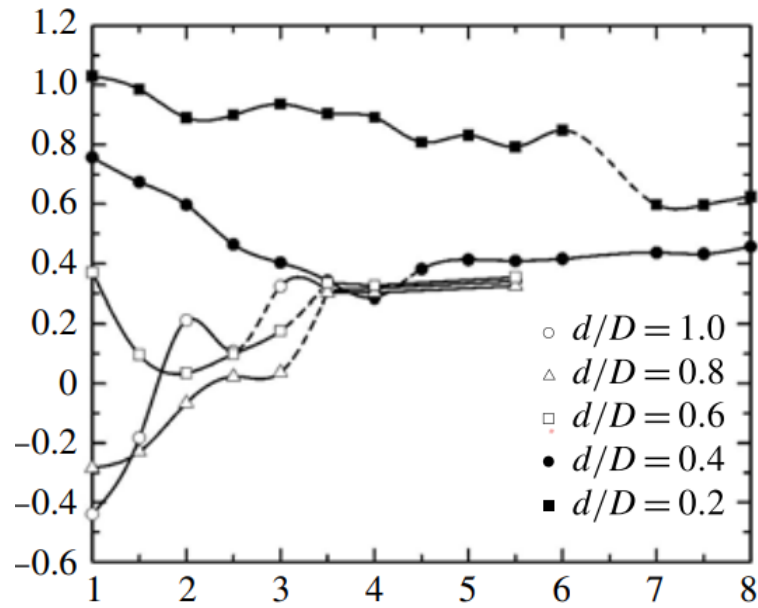


Figure 2.26: C_D as a function of L for different d/D (L. Wang, M. M. Alam, and Yu Zhou 2018).

This section has reviewed the effects of significant parameters on two tandem cylinders, assuming a two-dimensional flow. However, it is noteworthy that a comprehensive study of such systems with cylinders of finite height or $d/D > 1$ has not been conducted to the best of the author's knowledge. Although some studies have encountered such cases, their primary focus was not on flow topology and comparison to more straightforward scenarios. Therefore, further research is still needed to investigate the flow dynamics and characteristics of these more complex systems.

2.3. Research Objective

The literature review revealed that much research has been done on the aerodynamics of isolated cylinders with infinite height in the past. This focus can be attributed to the simple geometric shape of a cylinder, with only one geometric DoF, while having a complex bluff body wake response. Conversely, limited attention has been given to the study of cylinders with finite height. While the flow dynamics around two infinite drafting cylinders have been extensively explored, the examination of drafting cylinders with finite height remains relatively scarce. Furthermore, no systematic investigation exists wherein the aspect ratio of the two cylinders varies.

Previous studies have employed PIV as a measurement technique to examine the flow characteristics around cylinders. However, its primary application has been in qualitative investigations of flow topology rather than the quantitative determination of drag forces. The control volume approach is a well-established method that is gaining popularity, particularly in sports-related research. One such device is the *Ring of Fire*, which utilizes PIV and the control volume approach to determine cyclists' aerodynamic drag and can be deployed in the field to match real-world conditions better.

Therefore the objective of the thesis is:

To characterise the aerodynamics of two finite cylinders in tandem, with a focus on the aerodynamic drag of the trailing cylinder for different distances and aspect ratios.

In order to assess the attainment of the research objective, the following research question will be addressed in this study:

- What is the drag reduction of a trailing cylinder as a function of distance between the cylinders of different aspect ratios in tandem by:
 - performing wind tunnel balance measurements.
 - performing wind tunnel stereo-PIV measurements and utilizing control volume approach.

Due to the number of degrees of freedom involved in the study of cylinders in tandem with different aspect ratios, the following sub-questions will have to be addressed:

1. What is the aerodynamic drag of isolated cylinders with varying AR?
2. What is the aerodynamic drag of the trailing cylinder where both cylinders are of the same AR?
3. What is the aerodynamic drag of the trailing cylinder where cylinders are of different AR?

3

Measurement Techniques

This chapter aims to examine the relevant measurement techniques.

For the experiment a force balance and a stereo-PIV will be employed. After a brief description of the force balance, the PIV measurement technique is introduced with a detailed explanation of the simplest type of PIV, planar PIV. This is then followed by a stereo-PIV setup, which is the one that will be used for the experiment.

The subsequent section is dedicated to deriving equations for the control volume approach, as well as exploring various approaches for determining pressure based on velocity field data obtained through PIV.

3.1. Balance Measurements

In order to quantify the force exerted by the fluid flow upon the trailing cylinder, a dual-component force balance shall be employed. This apparatus comprises two strain gauges oriented in the freestream direction and one in the lateral direction. The operational mechanism of these devices is as follows: as a force is applied by the flow onto the trailing cylinder the strain gauge experiences a small deformation which results in the change of its resistances. It is connected with wires to a Wheatstone bridge, which effectively converts this change in resistance into a change of voltage. Subsequently, a data acquisition device is utilized to sample the signal at a designated frequency. This voltage then needs to be calibrated to accurately reflect the drag force.

A sampling frequency of 2.5 kHz has been selected to comprehensively capture both steady and unsteady phenomena such as vortex shedding.

A sample duration of 30 seconds was chosen to determine an ensemble average drag force. Before the start of the experiment the balance needs to be calibrated and whenever a new cylinder is put in the test section a baseline measurement at zero velocity is taken to serve as an offset for subsequent wind-on measurements.

Before every data acquisition, enough time needs elapse for new conditions to settle to avoid including any transient phenomena in the measurements.

3.2. Particle Image Velocimetry

Particle image velocimetry, or PIV, is an optical flow visualization method used to obtain instantaneous velocity measurement of the flow. Its simplest form consists of a laser beam expanded into a laser sheet, tracer particles, one digital camera, and a statistical method. This type of PIV is also referred to as planar PIV. The end result is an in-plane velocity vector field corresponding to the part of the flow that was illuminated by the laser and captured by the camera.

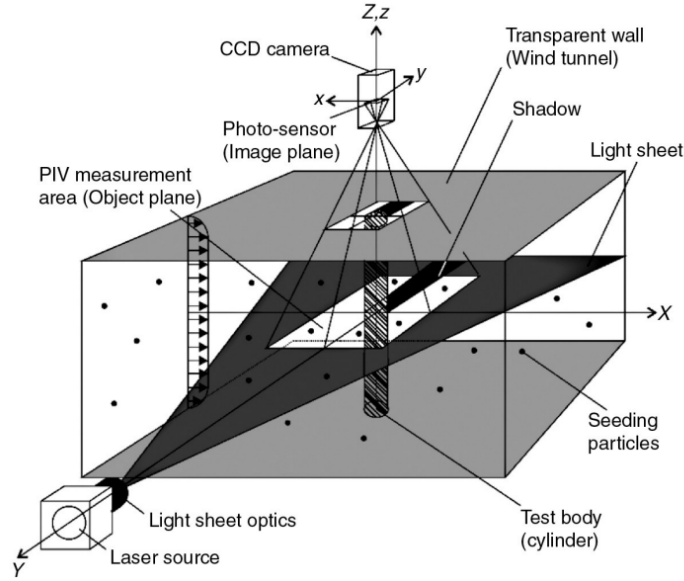


Figure 3.1: An example of a experimental PIV setup to examine the flow around a cylinder, where the measurement plane is parallel to the free stream direction (Atkins 2016).

The working principle of the planer PIV setup is as followed. Firstly, tracer particles are released into the freestream, where they get carried along with the flow throughout the test section where they are illuminated by the laser sheet at the measurement plane. Secondly, images of the now illuminated particles are captured by the camera at the two time steps, Δt apart. These two images of the particles are then combined analyzed with a statistical operator, the cross-correlation, that allows for determining the in-plane velocity vector field. A scheme of a experimental setup can be seen in the Figure 3.1. Each step of the process described above will now be described in more detail, including the most important considerations.

3.2.1. Tracer Particles

Having suitable particles to track is essential, as their change in relative position between the two time steps is what is used to determine the velocity vector field of the fluid flow. There are two main considerations for what a good tracer particle should have (Andrea Sciacchitano and Fulvio Scarano 2022):

1. It should follow the fluid flow as closely as possible.
2. It should scatter enough light from the laser, such that it can be picked up by the camera sensor.

When it comes to following the fluid flow, the parameter that is used to determine if the particle type is suitable or not is the particle Stokes number S_k . It is defined as the ratio between the particle response time τ_p , explored in more detail later, and flow characteristic time τ_f , defined as the ratio of the flow characteristic length L_{char} and a reference velocity Δv .

$$S_k = \frac{\tau_p}{\tau_f} \quad (3.1)$$

There exist numerous forces that exert an influence on particles and their fluid flow tracking ability. These include inertial forces arising from flow acceleration, body forces, quasi-steady viscous forces, the Basset force, additional forces due to added mass, and the lift force arising from particle rotation (Andrea Sciacchitano and Fulvio Scarano 2022).

In the case of small particles, the flow dynamics are primarily governed by the Stokes drag and a force due to acceleration. By imposing force balance, where these two forces are equal in magnitude and opposite in direction, the following equation 3.2 is obtained. Here the d_p represents the diameter of the particle, assuming that it can be approximated by a sphere, ρ_p the density of the particle, and ρ_f the density of the fluid.

$$\Delta V = V - U = -\frac{d_p^2 (\rho_p - \rho_f)}{18 \mu} \frac{dV}{dt} \quad (3.2)$$

The left-hand side of the equation 3.2 represents so-called *slip velocity* ΔV , which is a difference between the fluid flow velocity U and the particle velocity V . This discrepancy arises due to the acceleration of the flow and the particle's inability to respond instantaneously to the change. Ideally, this difference would be zero, and the particle's response would be infinitely fast. However, in practice and if $\rho_p \neq \rho_f$ it takes time for the particle to respond and reach the final flow velocity U . Therefore, we aim to minimise this difference. From equation 3.2 expression 3.3 for particle response time τ_p can be derived:

$$\tau_p = \frac{d_p^2 (\rho_p - \rho_f)}{18 \mu} \quad (3.3)$$

This equation indicates how long it takes for a particle to have a velocity variation equal to 63% the velocity variation in the flow. It is beneficial to look at parameters that affect τ_p since minimising it will improve particle responsiveness. From equation 3.3, it can be observed that the particle response time is directly proportional to the square of the particle diameter. Hence, a small particle diameter ensures a fast particle response to a variation of the fluid velocity. The particle response time is also improved if density of a particle matches that of the fluid. It is generally not possible to influence the fluid's properties since they are bounded by the problem that is being investigated. It can nevertheless be observed that if fluid's viscosity is larger, as is the case when comparing water and air, the response time is lower when the same tracer particles are used. Some of the common particles for use with air are: DEHS, Glycol water solution, Vegetable oil, TiO_2 (Andrea Sciacchitano and Fulvio Scarano 2022).

Flow characteristic time τ_f is determined based on the flow's specifics and the area being investigated. In an example of a cylinder where more prominent flow features are of interest, D can be chosen as L_{char} . However, if the focus is on the formation of vorticity, the characteristic length would have to be accordingly smaller, resulting in higher S_k . For having tracer particles accurately following the flow, a good practice is for S_k to be below 0.1 (Samimy and Lele 1991).

Laser light scatter from a particle is not uniform, as can be seen in figure 3.2. It needs to be ensured that enough light is scattered for the camera sensor to image a particle and provide enough contrast to the background. In the example of planar PIV, one is usually most interested in the side scatter, as this is where the camera will lay in relation to the laser sheet. In the case of a stereo-PIV setup with two cameras positioned at 90° to each other, it can be seen that one camera, the one closer to forward scatter, will receive more light than the other. It needs to be ensured that both cameras receive enough light. The light scattering depends on: particle diameter d_p , laser light wavelength λ , and the ratio of reflective indices (Andrea Sciacchitano and Fulvio Scarano 2022).

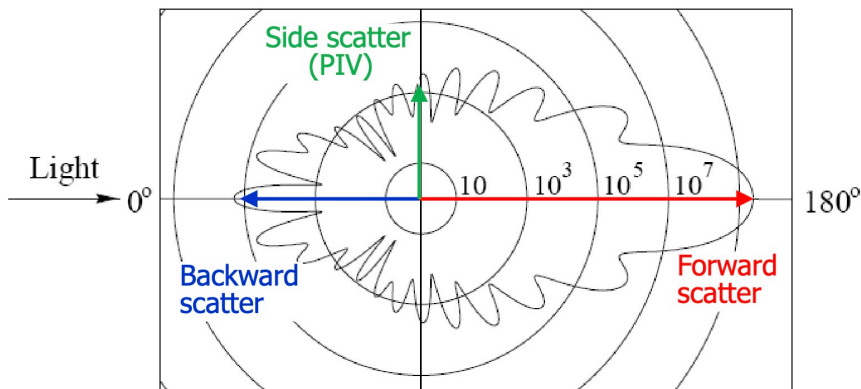


Figure 3.2: Example of a light scatter pattern around a particle (Andrea Sciacchitano and Fulvio Scarano 2022)

The following guidelines should be followed when introducing particles into a fluid flow. Firstly, the introduction of particles should not significantly alter the underlying fluid dynamics. Secondly, the seeding process should be as homogeneous as possible to ensure that the particle distribution is uniform throughout the flow. Typically, the concentration of particles should be around ten particles per cubic millimetre ($10 \text{ particles/mm}^3$) to ensure that the flow remains undisturbed while providing an adequate number of particles for tracking.

3.2.2. Laser Illumination

The purpose of the laser is to illuminate the tracer particles on the measurement plane so that the camera can capture their images. Lasers vary in the type of light wavelength they produce, power output, and repetition rate. Using a continuous laser would be beneficial since it would not require syncing laser pulsing with the camera shutter, but they are usually not powerful enough to illuminate the particles. Therefore pulsed lasers are more generally used as they can accumulate energy and release it in short bursts. To get the velocity information, we need to acquire two images of particles distribution. Since the timing Δt between the two pulses needs to be small, the repetition rate of a single pulsed laser is often not fast enough. Therefore an array of two lasers with a one-sided mirror is used, which allows for any desired Δt to be achieved with proper timing. Even with two lasers, especially when we are interested in unsteady measurements, the repetition rate still limits flow sampling in the time domain.

To ensure that the particles are visualised as dots and not streaks the pulse width δt should satisfy the following condition (Andrea Sciacchitano and Fulvio Scarano 2022):

$$\delta t \ll \frac{d_\tau}{VM} \quad (3.4)$$

where d_τ is the particle image diameter, V is its velocity and M the magnification factor. In principle, this equation tells us that during the laser pulse, we want the particle to travel far less than particle image diameter, in which case the light streaks will be minimal, and particles can be considered frozen in time.

Lasers produce a monochromatic and collimated beam of light that can be easily shaped into a desired plane. By using a combination of cylindrical and spherical lenses, we can achieve the desired sheet width and sheet thickness. We usually want the thickness to be between one and two millimetres. Too short might cause particles to leave the plane in time between the two images taken. Too large will result in the laser power density reducing further, which might not provide enough illumination, and the assumption that the measurements were taken in a plane will not hold as well.

3.2.3. Imaging

Once the particles get illuminated by the laser beam, an image of the measurement plane is taken by a digital camera. To relate the distances captured on the sensor with that in the object space magnification factor M needs to be determined. It is the ratio between the sensor-to-lens distance d_i and the lens-to-object distance d_o :

$$M = \frac{\text{sensor size}}{\text{object size}} = \frac{d_i}{d_o} \quad (3.5)$$

M relates the dimensions in the object space H and the image space h , where $h = M \cdot H$. Following the thin lens theory, the focal length of the lens f is connected to d_i and d_o with the following equation:

$$\frac{1}{f} = \frac{1}{d_i} + \frac{1}{d_o} \quad (3.6)$$

With these two equations, a selected focal length, and a desired field of view (FOV), an appropriate lens can be chosen, and an approximate camera position determined. One additional important lens parameter is the f-stop $f_\#$, which is defined as the ratio between the lens focal length and the aperture diameter d_{ap} :

$$f_\# = \frac{f}{d_{ap}} \quad (3.7)$$

On camera, it is usually changeable in discrete steps (2.8, 4, 5.6, 8, etc.). The lower the f-stop, the more aperture is opened, the more light gets captured, and the image is brighter, but also, the depth of field (DOF) becomes shallower. Ideally, one would want the sensor to capture as much light as possible since it would require less illumination and a less powerful laser. However, it needs to be ensured that the width of the focus plane δz is larger than the laser sheet thickness so that the measurement plane is fully in focus. Otherwise, the particles on the image will be out of focus. The equation that relates $f\#$ to δz is (Andrea Sciacchitano and Fulvio Scarano 2022):

$$\delta z = 4.88 \lambda f\# \left(\frac{M+1}{M} \right)^2 \quad (3.8)$$

Due to the small point-like size of a tracer particle on a sensor, the particle image diameter d_τ is not only influenced by its geometric size d_p but also influenced by diffraction d_{dif} :

$$d_\tau = \sqrt{(M d_p)^2 + (d_{dif})^2} \quad \text{where} \quad d_{dif} = 2.44 \lambda f\# (1 + M) \quad (3.9)$$

Equation 3.9 assumes that the particles are imaged in focus and that there is no lens aberration. To achieve sub-pixel accuracy, d_τ should be on the order of 2 – 3 pixels in diameter. If d_τ is less than 1 pixel in diameter, the phenomenon known as peak locking will occur (Westerweel 1997), rendering it impossible to determine sub-pixel displacements. Therefore, it is crucial to carefully select particle sizes and imaging parameters to ensure accurate and reliable tracking of the fluid flow.

Determining the appropriate time interval Δt between consecutive images is important. A commonly used guideline is the one-quarter rule, which suggests selecting the pulse separation such that the particles travel one-quarter of the interrogation window, the concept of which will be described in more detail in the following section. This approach ensures sufficient particle displacement between consecutive frames to accurately estimate the fluid flow velocity.

3.2.4. Data Processing

So far, the result of the process is two in-focus images of the particles separated by Δt as seen in figure 3.3.

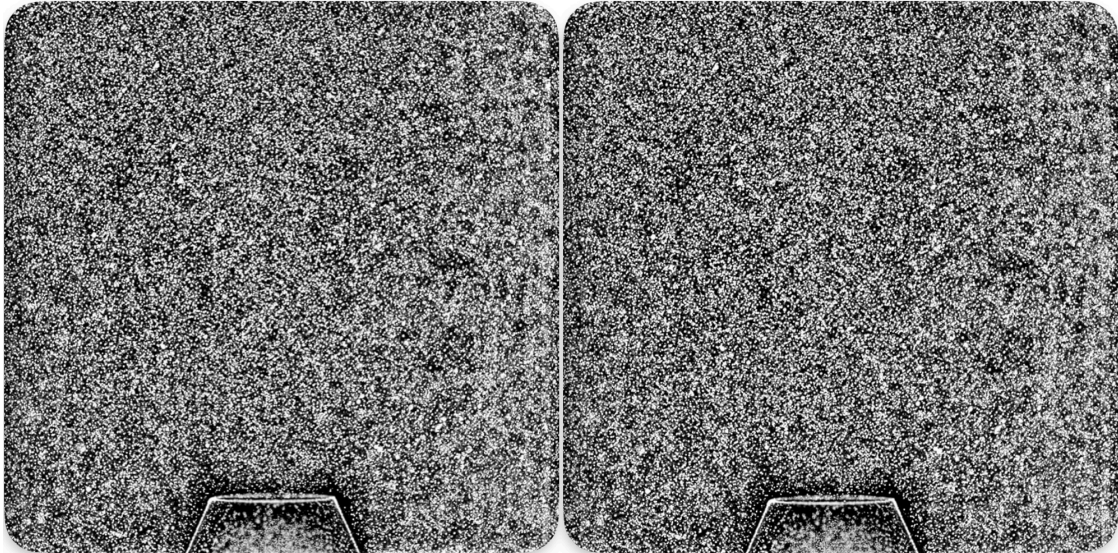


Figure 3.3: Two images of the flow separated by Δt (Andrea Sciacchitano and Fulvio Scarano 2022).

the data processing step aims to determine the velocity field from the two images. To determine it, the following equation is used:

$$u = \frac{\Delta x}{M \Delta t} \quad v = \frac{\Delta y}{M \Delta t} \quad (3.10)$$

u and v are components of the velocity vector \mathbf{v} , M magnification factor, Δt pulse width separation and Δx Δy particle displacements in the two in-plane dimensions. The M is determined from equation 3.5, and Δt is chosen, meaning only displacements still need to be determined. This is not done on a particle-to-particle basis but by systematically dividing the image and applying cross-correlation, as will be explained now. Firstly, images are divided into smaller so-called interrogation windows. In each window, one velocity vector is computed, corresponding to the average velocity of the tracer particles within that window. They can be of various shapes, although rectangles are the simplest form. Each window should contain at least ten tracer particles to ensure adequate tracking accuracy (Andrea Sciacchitano and Fulvio Scarano 2022). An example of a rectangular window at the same position on the two images separated by Δt can be seen in figure 3.4.

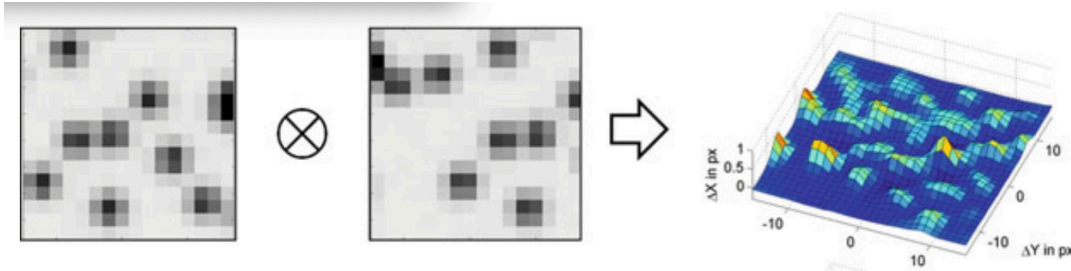


Figure 3.4: Example of interrogation windows from the two images separated by Δt and a resulting cross-correlation map between them (Raffel et al. 2018).

Once the two images are divided, a cross-correlation map ϕ , equation 3.11, is computed between the corresponding windows from the first and second image. The cross-correlation map provides a measure of similarity between the particle configurations in the two images. It is used to estimate the displacement vector between the two windows. This displacement vector is then used to calculate the fluid flow velocity using equation 3.10. This process is repeated for all interrogation windows, resulting in a grid of velocity vectors that gives the velocity vector field of the measurement plane.

$$\phi(m, n) = \frac{\sum_{i,j=1}^{I,J} IA(i, j) \cdot IB(i + m, j + n)}{\text{stdev}(IA) \cdot \text{stdev}(IB)} \quad (3.11)$$

The peak in a correlation map of the individual interrogation window presents the highest degree of matching with any second image window (the maximum in a cross-correlation map in figure 3.4). From this information, the displacement of particles between the two windows can be determined. The size of the window, therefore, limits the resolution of the velocity field. We can reduce the window size to increase it, but poor tracking might occur if reduced too much. Additional steps can be taken to increase the resolution, such as multiple passes and overlapping of the interrogation windows.

The cross-correlation map function produces a discrete set of values. To approximate the displacement more precisely, interpolation schemes like Gaussian fit can be used.

Once the satisfactory displacement vector field is computed, it can be divided by the magnification factor M and time between the two pulses Δt to obtain the velocity field.

3.3. Stereo-PIV

The Planar PIV, while being a powerful tool for flow measurement, has inherent limitations. The main one is the inability to capture the out-of-plane components of the velocity vector. This might pose a problem even in situations where only the in-plane velocity field is of interest. If the flow is highly three-dimensional, the out-of-plane velocity contributes noticeable uncertainty due to the so-called perspective transformation (Raffel et al. 2018). To overcome this limitation, a strategically positioned secondary camera can be introduced, resulting in a setup commonly referred to as stereo-PIV. In the following section, detailed specifications and considerations of this method, which are not required for planar PIV, will be presented, along with recommendations for achieving optimal results.

3.3.1. Stereo-PIV Setup

There exist multiple variations of the stereo-PIV setup. However, the one that is most common and will also be used during this thesis work consists of two cameras positioned to have a different view of the measurement plane.

For this setup, two basic imaging configurations exist: the translation method and the angular displacement method (Raffel et al. 2018). The focus will be on the latter as it is more common and will also be used during our experiment. Figure 3.5 shows an example of such a configuration. Since modulation transfer function (MTF) is generally best near the lens's principal axis, a camera's lens is aligned with the principal viewing direction. While this is beneficial from the perspective of obtaining the best possible image, it has two main drawbacks. The first drawback is that a large angle between the lens axis and the object plane would require a significant depth of field which is not achievable due to additional imaging constraints, as discussed during planar PIV. To alleviate this, the sensor image plane is rotated such that it, along with the lens's plane and the object plane, coincide in the same line (seen as a point looking from above in figure 3.5). The result of doing this is that the focus plane is now aligned with the object plane. This is often referred to as the Scheimpflug criterion.

The second drawback of the tilted lens, further exaggerated by the now tilted image plane, is the disordered perspective (Raffel et al. 2018). This results in an uneven magnification factor across the images, requiring additional calibration.

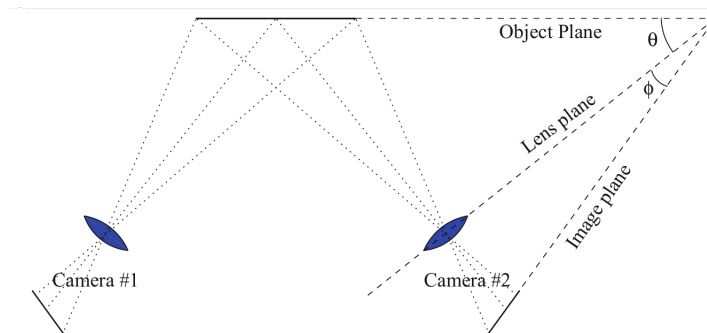


Figure 3.5: Angular lens displacement method with tilted back plane stereo-PIV imaging configuration (Raffel et al. 2018).

3.3.2. Calibration

Once the images have been taken and before the velocity field can be reconstructed from the particle displacements, this data firstly needs to be transformed from the image plane at a camera to the object image plane. During this process, magnification and other effects need to be accounted for.

There are different approaches to this transformation. One is to relate the image and the object plane through geometric optics, but this requires detailed knowledge of the optical setup and the distances between the two planes and does not account for nonlinearities such as lens distortion. This makes this method sensitive to small changes and impractical for most cases (Raffel et al. 2018). More robust approaches are those that create a mapping function, such as second-order image mapping and perspective projection. They rely on a combination of image-object point pairs and a least square fit method for the first and the Levenberg–Marquart method for the latter to determine the missing coefficient of the mapping function. The advantage of this approach is that it does not require physical models and can also account for nonlinearities by the higher order terms (Raffel et al. 2018).

These methods are used for transformations from the image to the object plane, but they do not provide information about camera positions needed for the velocity vector determination.

There exist multiple ways of determining positions between the two cameras and the measurement plane, but one often used with stereo-PIV, and will also be used during this experiment, is the one with the dual level calibration target, such as the one in figure 3.6.

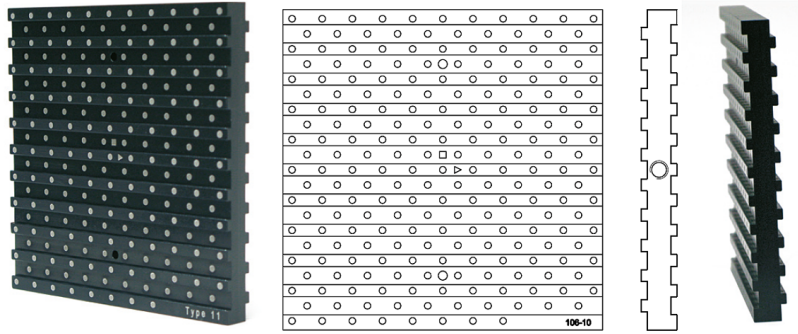


Figure 3.6: An example of a dual level calibration target used for stereo-PIV (LaVision n.d.).

This target is positioned co-linear with the object plane and consists of well-defined grid markers that can be used to determine the adequate mapping between the image and the object plane. Having grid points on one level does not provide enough information to determine the camera viewing angles. If the process is repeated with an additional set of points at a slight displacement or if the target already has markers at two levels, it is possible to relate the image plane to the two object planes and their relative positions (Raffel et al. 2018). Aside from determining transformations, additional corrections are applied at this step to improve the measurements' quality and account for slight displacements and movements during the measurement.

3.3.3. Velocity Field Reconstruction

Once images of the flow from the two image planes at the two timesteps are transformed to the object plane, the information about particle positions from the two perspectives and their displacement with time can be used to reconstruct the velocity vector. As a reference, figure 3.7 will be used, where α is the angle in the XY plane and β in the YZ plane (not shown in the reference). M is the magnification factor obtained during calibration, D with its components D_x, D_y, D_z is particle displacement, U, V, W velocity components and $x'_i - x_i$ represents the particle displacement projection in x direction on the image plane and $y'_i - y_i$ similarly the displacement projection in y direction. Notations with 1 represent the left camera, and those with 2 the right camera. The process of obtaining the velocity vector closely follows the one explained in (Raffel et al. 2018).

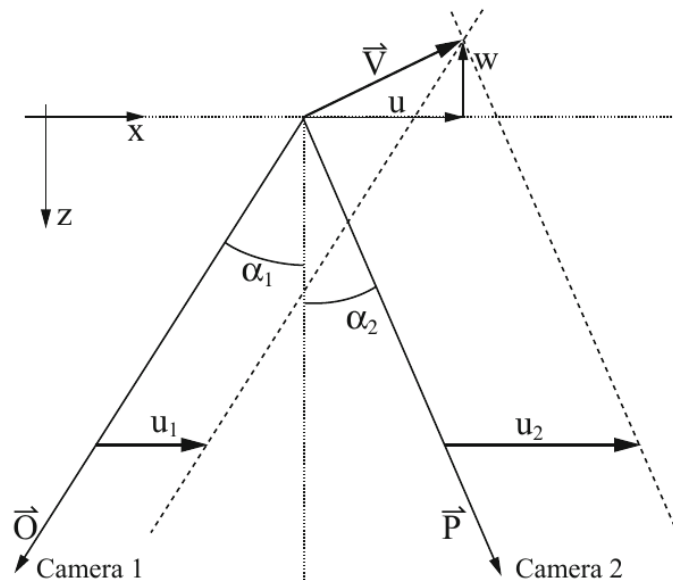


Figure 3.7: Geometrical reconstruction of the stereo-PIV setup for XZ-plane (Raffel et al. 2018).

For each camera we can use the following expressions 3.13 and to reconstruct the in-plane velocity

components:

$$x'_i - x_i = -M \left(D_X + D_Z \frac{x'_i}{z_0} \right) \quad (3.12)$$

$$y'_i - y_i = -M \left(D_Y + D_Z \frac{y'_i}{z_0} \right) \quad (3.13)$$

where $\frac{x'_i}{z_0}$ and $\frac{y'_i}{z_0}$ can be expressed through:

$$\tan \alpha = \frac{x'_i}{z_0} \quad (3.14)$$

$$\tan \beta = \frac{y'_i}{z_0} \quad (3.15)$$

From here, it follows that the in-plane velocity as seen from one camera can be reconstructed using:

$$U_i = -\frac{x'_i - x_i}{M \Delta t} \quad (3.16)$$

$$V_i = -\frac{y'_i - y_i}{M \Delta t} \quad (3.17)$$

Once those are determined, the three components of the velocity vector can be determined as:

$$U = \frac{U_1 \tan \alpha_2 + U_2 \tan \alpha_1}{\tan \alpha_1 + \tan \alpha_2} \quad (3.18)$$

$$V = \frac{V_1 \tan \beta_2 + V_2 \tan \beta_1}{\tan \beta_1 + \tan \beta_2} \quad (3.19)$$

$$W = \frac{U_1 - U_2}{\tan \alpha_1 + \tan \alpha_2} \quad (3.20)$$

$$W = \frac{V_1 - V_2}{\tan \beta_1 + \tan \beta_2} \quad (3.21)$$

It can be observed that the system of equations is over-defined. One way of solving it is to use the least square fit method, where the residual ϵ_{resid} can be used as a measure of quality. In an ideal case, it would be zero, but in practice, the common values are in the range of $0.1 - 0.5px$ according to (Raffel et al. 2018).

3.3.4. Recommendations

In the book (Raffel et al. 2018), the authors provide some general guidelines to increase the quality of the stereo-PIV measurements:

- To minimize uncertainty, the two cameras should be positioned 90° apart unless a specific velocity component is more important, at which point the camera angles should be adjusted accordingly.
- Multi-level calibration target provides sufficient calibration results.
- The minimum PIV interrogation window should be equal to or larger than the light sheet thickness.
- The residual ϵ_{resid} from the velocity vector reconstruction can be used as quality measurements, and its values should typically be in the $0.1 - 0.5px$ range.
- An appropriate image reconstruction technique should be used. Image deformation and image back project can be combined into one step to maximize performance.

3.4. PIV Uncertainty Quantification

This section will explore the sources of uncertainty when using PIV. This will be followed by a separate section on error propagation of determining aerodynamic drag from PIV measurements after the control volume approach is introduced.

Following (Andrea Sciacchitano 2019), we can systematically identify sources of errors based on where in the process they occur:

Fluid Flow

Fluctuations in velocity, streamline curvature, and velocity gradients result in errors due to algorithms struggling to resolve those correctly and due to particle slip velocity. With current, more advanced algorithms, the effects of in-plane velocity gradients can be resolved, while out-of-plane gradients can not be accounted for and contribute to uncertainty (Andrea Sciacchitano 2019).

Since PIV can only determine particle displacements, fluctuations in fluid properties like temperature, density, and viscosity, along with variations in the Re and Ma , can not be accounted for and increase the measurement error (Andrea Sciacchitano 2019).

Particle Tracking

As discussed in a previous section 3.2.1 on tracer particles, the velocity field of the fluid flow is measured indirectly through the particle displacement. Due to a difference between the properties of the fluid and particles, there is a velocity mismatch, also called slip velocity. The lower the velocity difference smaller the error. The requirements for the responsiveness of the particles vary based on the type of experiment. Good results can be obtained in the air with liquid or solid tracers with particles of size $0.1 - 2 \mu m$ (S. Wang, Mao, and Guanwei 2007). But with helium-filled soap bubbles, which are neutrally buoyant, the size can be larger $300 - 500 \mu m$ (Fulvio Scarano et al. 2015).

Due to the constant transition of particles through the measurement plane, some are only captured on the first or second image. Therefore, those particles can not be correlated and contribute to noise. Particles also overlap from a perspective of a camera, increasing the intensity and causing random errors in the displacement (Andrea Sciacchitano 2019).

Experimental Setup

In the case of a stereo-PIV, which uses two cameras to determine the velocity field, some error sources, such as perspective errors that come with a planar PIV, can be avoided. Additional self-calibration procedures can attenuate slight misalignment between the calibration plate and the measurement plane. Nevertheless, it is always good to follow best practices, if possible, while setting up an experiment to reduce the uncertainty further, such as having cameras positioned at 90° , having a more considerable distance between the measurement plane and the two cameras, and using a telecentric lens (Andrea Sciacchitano 2019).

Illumination

A laser system with sufficient illumination is important to produce enough contrasts between particles and the background. Slight variations between the intensity of the two pulses are insignificant as long as they aligned well on the measurement plane since the cross-correlation operator is insensitive to absolute intensity variations (Andrea Sciacchitano 2019).

Timing

The equation 3.10 shows that the timing δ directly affects the determination of the velocity vectors. (Bardet, André, and Neal 2013) performed a study on timing issues for more multiple laser systems and found that the timing errors were mostly systematic, from $40ns$ to several microseconds, and that random errors were negligible in comparison. This means that in a situation such as investigating supersonic flow, where this uncertainty would be too high to obtain qualitative results, they can be accounted for and removed.

Imaging

When it comes to errors that originate from imaging, peak locking is an important phenomenon, as mentioned briefly in a previous section. It occurs when an image of a particle is smaller than the size of a pixel on the camera sensor. When cross-correlation is later performed, the displacement of the particle is biased toward integer pixel displacements and does not allow for subpixel accuracy. The errors that originate from this are on the size of $0.1px$ (Andrea Sciacchitano 2019) and can not be neglected in general. Besides making images of the particles larger, as discussed previously, different methods have been developed to try and mitigate pick locking, such as optical diffusers, image defocusing, multi- Δt image acquisition, and data post-processing approaches (Andrea Sciacchitano 2019).

Additional errors also occur due to the noise of pixel readings.

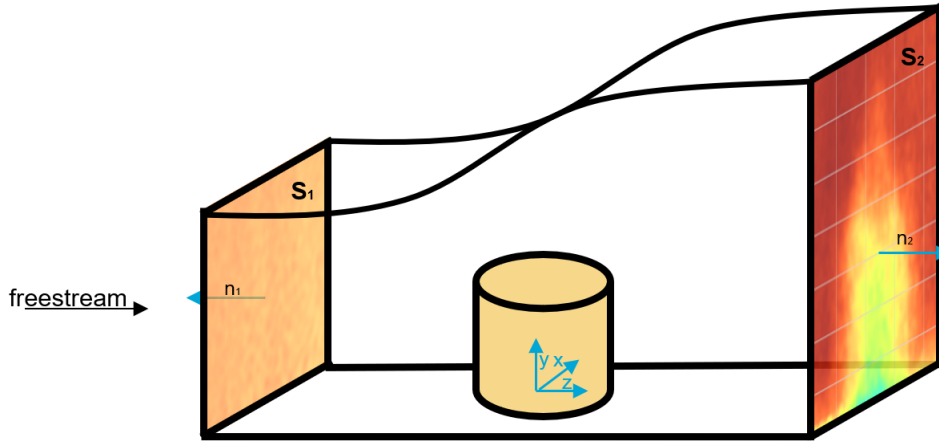


Figure 3.8: Control volume around a cylinder. Cylinder is not part of the fluid and the cylinder surface acts as a part of a control surface.

Evaluation Techniques

Once images are captured, they need to be processed to obtain the velocity field information. The errors that arise from this process depend on the evaluation technique and the parameters chosen. This includes interrogation window sizes and shapes, cross-correlation peak fit algorithms, and image and vector interpolation schemes for image deformation algorithms (Andrea Sciacchitano 2019).

3.5. Control Volume Approach

3.5.1. Theoretical Background

To determine the drag coefficient C_D of a system using PIV images of the flow, a control volume is positioned around the cylinder system and the momentum equation is applied in an integral form. An example of a such control volume that will also be used as a reference can be seen in figure 3.8.

Please note that in this chapter on measurement techniques, the x-axis of the coordinate system is aligned with the freestream, as often found in the literature. Later, the z-axis will be aligned with the freestream for the experiment.

Starting from the integral form of the incompressible momentum equation in the Eulerian formulation:

$$\frac{\partial}{\partial t} \iiint_V \rho \mathbf{v} dV + \iint_S (\rho \mathbf{v} \cdot \mathbf{n}) \mathbf{v} dS = - \iint_S p \mathbf{n} dS + \iiint_V \rho \mathbf{f} dV + \iint_S \boldsymbol{\tau} \cdot \mathbf{n} dS + \mathbf{R} \quad (3.22)$$

Where ρ is the density of the fluid, V the control volume, \mathbf{v} the velocity vector, S the surface of the control volume, \mathbf{n} normal of the control surface facing outwards, p pressure, \mathbf{f} body forces, $\boldsymbol{\tau}$ the internal shear tensor and \mathbf{R} the reactive force action the fluid flow. Assuming steady incompressible flow with constant viscosity and neglecting volumetric forces, our problem can now be reduced to the following equation where \mathbf{F} is the total aerodynamic force of the fluid acting on the body, in figure 3.8 that would be the cylinder, and is equal to $-\mathbf{R}$:

$$\mathbf{F} = - \iint_S \rho (\mathbf{v} \cdot \mathbf{n}) \mathbf{v} dS - \iint_S p \mathbf{n} dS + \iint_S \boldsymbol{\tau} \cdot \mathbf{n} dS \quad (3.23)$$

The first term on the right side represents the sum of the flow momentum over the boundaries of the control volume, the second term is the integral of the pressure over the external surfaces, and the last term is the sum of shear forces over the boundary of the control volume.

One important thing that can be observed from this equation is that the drag force can be determined by only looking at what is happening at the contour of the control volume without having the knowledge of what is going on on the inside. This is the main working principle behind the control volume approach (CVA).

For this study, we are interested in the mean forces acting on the body. To do so, the velocity can be decomposed into its mean values and unsteady turbulent fluctuations:

$$\mathbf{v} = \bar{\mathbf{v}} + \mathbf{v}' \quad (3.24)$$

we can now rewrite our equation 3.23 by replacing \mathbf{v} with $\bar{\mathbf{v}} + \mathbf{v}'$ from equation 3.24 (B. Oudheusden et al. 2007). We will now rewrite the system of equations in the tensor notation for clarity:

$$\bar{F}_i = -\rho \iint_S \bar{v}_i \bar{v}_j \bar{n}_j dS - \rho \iint_S \overline{v'_i v'_j} n_j dS - \iint_S \bar{p} n_i dS + \mu \iint_S \left(\frac{\partial \bar{v}_i}{\partial x_j} + \frac{\partial \bar{v}_j}{\partial x_i} \right) n_j dS \quad (3.25)$$

For our specific case, we can make certain assumptions to simplify the problem further:

- We only consider the drag force, which is the force acting in the direction of the flow (x direction as in in figure 3.8), reducing our system to a single equation.
- if we make our inlet and outlet surfaces perpendicular to the flow and align others to follow the streamlines, where $\mathbf{v} \cdot \mathbf{n} = 0$, which will make their integrals all zero, we only have to evaluate momentum terms on the inlet and outlet.
- If we take surfaces sufficiently far away from the object, we can assume that the pressure on all boundaries of the CVA around equals p_∞ . In that case the integral of the pressure term on the sides of the control volume equals to zero and only the inlet and outlet planes need to be considered. If this assumption can not be made, the side planes need to be included in the calculations.
- Similarly, if we take the contour far away from the body where it is mostly in freestream and the flow is more *regular*, we can neglect the viscous stresses (B. Oudheusden et al. 2007).

This results in the system of equations 3.25 being noticeably reduced as seen in equation 3.26. Here S_1 refers to the area of the control volume inlet surface and S_2 to the outlet as indicated in figure 3.8

$$\bar{F}_x = \rho \iint_{S_1} \bar{v}_x^2 dS - \rho \iint_{S_2} \bar{v}_x^2 dS + \rho \iint_{S_1} \overline{v_x'^2} dS - \rho \iint_{S_2} \overline{v_x'^2} dS - \iint_{S_1, S_2} \bar{p} n_x dS \quad (3.26)$$

This is the main equation that will be utilized in the analysis of drag acting on isolated bodies as well as bodies arranged in tandem.

In literature, researchers often make additional assumptions that result in a simpler expression. If we assume conditions on the upstream plane to be constant, such that the momentum term can be represented using only one average velocity, velocity fluctuations on the inlet can be neglected and that pressure can be expressed as one constant value p_1 , then, from (Anderson 2017), we can do the following.

Starting from the conservation of mass in an integral form, we can write:

$$\iint_{S_1} \rho v_{S_1,x} dS = \iint_{S_2} \rho v_{S_2,x} dS \quad (3.27)$$

We can now multiple both sides by $v_{S_1,x}$ and put it inside the integral since it is constant:

$$\iint_{S_1} \rho v_{S_1,x}^2 dS = \iint_{S_2} \rho v_{S_1,x} v_{S_2,x} dS \quad (3.28)$$

This allows us do modify our original momentum term:

$$\iint_{S_1} \rho v_{S_1,x}^2 dS - \iint_{S_2} \rho v_{S_2,x}^2 dS = \iint_{S_2} \rho v_{S_1,x} v_{S_2,x} dS - \iint_{S_2} \rho v_{S_2,x}^2 dS \quad (3.29)$$

$$= \iint_{S_2} \rho v_{S_2,x} (v_{S_1,x} - v_{S_2,x}) dS \quad (3.30)$$

The equation for aerodynamic drag force D can now be rewritten:

$$D = \iint_{S_2} \rho v_{S_2,x} (v_{S_1,x} - v_{S_2,x}^2) dS - \rho \iint_{S_2} \overline{v_x'^2} dS + p_1 S_2 - \iint_{S_2} \bar{p} n_x dS \quad (3.31)$$

A rigorous examination of equation 3.26 reveals that both velocity and pressure information is required to obtain accurate results. While velocity data can be obtained directly from PIV measurements, pressure cannot be directly measured using PIV. Calculating pressure from PIV images will be the topic of the following section.

3.6. Pressure from PIV

Since we are unable to measure pressure directly, we need to determine it indirectly. Through time, many methods have been developed to quantify pressure without flow protrusion. From all of the methods developed in the past, using high-quality velocity PIV data appears to be the most powerful tool so far (B. W. v. Oudheusden 2013). There are different approaches to utilizing obtained PIV velocity field data, but they all involve combining experimental data with governing equations.

In the case of irrotational, incompressible, inviscid flow Bernoulli equation can be used to relate pressure and velocity. Usually, the starting point is the NS momentum equation, which allows for steady and unsteady conditions depending on the formulation. We can express them in a Lagrangian or Eulerian frame of reference and with pressure gradient or divergence (Poisson equation) formulation. The formulation of the equations for incompressible flow can be seen below:

- Lagrangian formulation in a form of a pressure gradient:

$$\nabla p = -\rho \frac{D\mathbf{u}}{Dt} + \mu \nabla^2 \mathbf{u} \quad (3.32)$$

- Lagrangian formulation in the form of a Poisson equation:

$$\nabla^2 p = \nabla \cdot \left(-\rho \frac{D\mathbf{u}}{Dt} + \mu \nabla^2 \mathbf{u} \right) \quad (3.33)$$

- Eulerian formulation in the form of a pressure gradient:

$$\nabla p = -\rho \frac{\partial \mathbf{u}}{\partial t} - \rho (\mathbf{u} \cdot \nabla) \mathbf{u} + \mu \nabla^2 \mathbf{u} \quad (3.34)$$

- Eulerian formulation in the form of a Poisson equation:

$$\nabla^2 p = -\rho \nabla \cdot (\mathbf{u} \cdot \nabla) \mathbf{u} \quad (3.35)$$

While theoretically, all of these formulations are identical, when implemented practically, their accuracy varies. This is due to different velocity propagation errors and sensitivity to spatial and temporal discretization (B. W. v. Oudheusden 2013).

Now, let us examine the individual components that are involved in the Eulerian formulation of the Poisson equation.

$$\nabla^2 p = \left(\frac{\partial u}{\partial x} \right)^2 + \left(\frac{\partial v}{\partial y} \right)^2 + \left(\frac{\partial w}{\partial z} \right)^2 + 2 \frac{\partial v}{\partial x} \frac{\partial u}{\partial y} + 2 \frac{\partial w}{\partial x} \frac{\partial u}{\partial z} + 2 \frac{\partial w}{\partial y} \frac{\partial v}{\partial z} \quad (3.36)$$

In the context of the Eulerian formulation of the Poisson equation, it becomes apparent that the out of plane gradient terms, denoted by $\frac{\partial}{\partial x}$, are present. These terms, however, cannot be computed with stereo PIV measurements, as velocity data is only obtained in a single plane. To obtain volumetric data, either fully tomographic PIV measurements or additional measurement planes separated by a distance Δx are required. One such method is multiple plane stereo particle image velocimetry, proposed by (Kähler and Kompenhans 2000), designed for this specific case. Nonetheless, several studies, like (Charonko et al. 2010), (De Kat and Van Oudheusden 2012), have demonstrated that small out-of-plane gradients do not significantly affect the determination of the pressure field.

3.6.1. Uncertainty of the Pressure Measurements

There are multiple factors that affect the accuracy of pressure determination. The most important ones are:

- Neglecting the out-of-plane gradients.
- accuracy of the velocity field data.
- spatial resolution and with it numerical discretization error and precision error.

As mentioned before, the uncertainty of the velocity measurements from the PIV experiment is expressed by the cross-collation precision. Following (Raffel et al. 2018) $0.1 px$ can be set as a characteristic value for $\varepsilon_{CC,PIX}$. From there the velocity uncertainty ε_u can be expressed as:

$$\varepsilon_u \approx \frac{\varepsilon_{CC,PIX}}{M, \delta t} \quad (3.37)$$

Following (De Kat and Van Oudheusden 2012) and assuming that Taylor series expansion can be used to estimate the truncation error, taking the second order central discretization scheme, assuming velocity measurements are uncorrelated, overlap factor is not larger than 50% the uncertainty of the material derivative in the Eulerian formulation is:

$$\varepsilon_{Du/Dt}^2 \approx \varepsilon_u^2 \left(\frac{1}{2\Delta t^2} + \frac{1}{2} \frac{|\mathbf{u}|^2}{h^2} + |\nabla \mathbf{u}|^2 \right) \quad (3.38)$$

where h represents grid spacing. And the same in the Lagrangian formulation:

$$\varepsilon_{Du/Dt}^2 \approx \varepsilon_u^2 \left(\frac{1}{2\Delta t^2} + \frac{1}{2} |\nabla \mathbf{u}|^2 \right) \quad (3.39)$$

Upon analyzing the equations for the uncertainty in both Lagrangian and Eulerian formulations, it becomes apparent that the first error is related to precision error, while the second error in Eulerian formulation is due to truncation error. In contrast, the second error in Lagrangian formulation arises from path-line reconstruction. While it may seem that Lagrangian method is superior for pressure determination, solely based on the equations for uncertainty, this can be deceiving. (De Kat and Van Oudheusden 2012) summed up their comparison on during a test by saying that Eulerian implementation is more sensitive to noise and advection motion, while Lagrangian struggles with capturing rotational flow, since it complicates flow path reconstruction. (Jakobsen, Dewhurst, and Greated 1997) compared the two formulations on a standing wave and found that Eulerian consistently outperformed the other, citing poor tracking due to large accelerations and long tracking times.

Focusing now more on the Eulerian formulation, (Murai et al. 2007) performed a comparison between using Poisson formulation and iterative integration of the pressure gradient formulation and found that there is little difference (De Kat and Van Oudheusden 2012). They also investigated the effect of noise and found that the gradient method was more susceptible, where as the Poisson equation showed to be insensitive due to the way it is integrated. (Charonko et al. 2010) compared different Eulerian implementations and integration methods and found that all integration methods were highly susceptible to noise, which is in contrast with many other studies, including (De Kat and Van Oudheusden 2012) where they found it to be minimum. All methods showed to perform well to about 30° of misalignment. (Violato, Moore, and Fulvio Scarano 2011), found in their study where they compared tomographic PIV and Lagrangian approach on a 2D plane, that as long as the plane is aligned with the dominant flow direction, results were comparable. Still, the planer results become erroneous when that condition is not met anymore. (De Kat and Van Oudheusden 2012) investigated the effect of temporal and spatial resolution on the determining pressure on an example of advecting Gaussian vortex. They found that the normalized pressure peak response was within 10% when the window size was smaller than one-third of the vortex core. They also investigated out-of-plane stereoscopic PIV planes and found the 10% reduction in peak pressure at 25° . Their practical experiment found that stereo PIV performed well where there were no strong 3D flows.

Note all the research cited above was performed in unsteady conditions since this is more interesting for analyzing turbulence and other unsteady phenomena, where pressure determination from PIV would be most beneficial. In their work (De Kat and Van Oudheusden 2012) also made recommendations and supplied some criteria for successful determination of the pressure:

- For both implementations (Eulerian and Lagrangian), the window size should be set sufficiently small relative to the flow structures.
- Larger OF increases the quality but is less influential when the window size is sufficiently small.
- complete 3d measurements are needed to capture the pressure in 3D flow properly,
- Reducing the measurement noise of the velocity field improves pressure determination directly

3.7. Aerodynamic Drag Uncertainty with CVA

In work (Spoelstra et al. 2021), the authors performed a study to identify the main sources of uncertainty for their Ring of Fire (RoF) measurement concept. Its working principle also follows the control volume approach; therefore, their uncertainty findings can also be applicable to our experiment. The main difference between a *classical* stereo-PIV setup and the RoF is that the latter is designed to perform on-site experiments of aerodynamic drag for transiting objects (Spoelstra et al. 2021) and allows for a study of full-size test subjects such as cyclists and professional ice-skaters.

Initially, they made a priori uncertainty drag estimation by performing a linear error propagation for an example where the velocity measurements are affected by the random error ϵ_{rand} . They assume that the pressure between the inlet and the outlet can be neglected and that there was an uniform inflow. Their simplified CVA equation resulted in the following:

$$D = \rho \iint_A (u_\infty - u) \cdot u dS \quad (3.40)$$

Where D is the resulting drag force, u_∞ free stream velocity, and u streamwise velocity component behind the cyclist. They assumed that that random error affecting velocity could be included as:

$$u = u_{true} - \epsilon_{rand} \quad (3.41)$$

Combining these two equations result in an equation for the drag force:

$$D = D_{true} - \rho \iint_A \epsilon (u_{true} + \epsilon) dS \quad (3.42)$$

or if the error is assumed to be uncorrelated with the velocity:

$$D = D_{true} - \rho \iint_A \epsilon^2 dS \quad (3.43)$$

This expression shows that the random error in the velocity field results in underestimating the drag force (Spoelstra et al. 2021). They tested this further by performing a Monte Carlo simulation on a flow field around a sphere and found the same results. This finding highlights the importance that the inlet and outlet size should not be arbitrary but small as possible. On the other hand, the contours of the surfaces should not cut into the body's wake. Doing so will interfere with the fluid dynamics and braking assumption about the CVA, resulting in high and unpredictable uncertainty. Therefore, to minimize the error, the size of the countries should be just large enough to encompass the wake of the body in question.

This study also investigated the sensitivity of spatial resolution on the results. Finite interrogation windows with cross-correlation have a filtering effect (Raffel et al. 2018). This could affect the drag estimate when using CVA. Reducing the size of the windows will reduce this effect but will come at the cost of increased uncertainty (Andrea Sciacchitano 2019). This means that there is an optimum somewhere in between. They found that the size of the window should be within $0.05 c_{len}$ and $0.25 c_{len}$, where c_{len} is the characteristic length scale of the wake.

3.8. Examples of CVA Application

The utilization of the control volume approach (CVA) for the determination of body drag is a well-established method in the field of fluid dynamics. In this section, two examples of CVA will be looked at. The first, more academic, says something about various terms in the formulation of the CVA and how they vary as the distance from the body increases. The second study applied the CVA in practice

to determine the drag of a trailing cyclist.

In the work (Terra, Sciacchitano, and Scarano 2017), the authors performed a large-scale tomographic PIV imaging of the flow behind a sphere to determine the drag force exerted by the flow on it. The latter was done by invoking the time-average momentum equation within a control volume. Tomographic PIV allows for imaging the whole velocity field inside a volume, not limited to the measurement plane as in the case of stereo-PIV. While CVA only relies on the control surface of the control volume, having information about the flow inside allows for the pressure term to be fully resolved, as described in a previous section on obtaining pressure from PIV images. As part of the study, they varied the outlet plane as the distance from the sphere and investigated how the various terms of the right side in equation 3.26 for drag vary with distance and how much they contribute to the aerodynamic drag. The results of that study can be seen in figure 3.9.

What can be observed is that the combined C_D remains fairly constant, while its contributions vary significantly, especially in the close wake. Here, the contributions of the pressure term play a significant role and should be addressed. That can only be done after $5 x/D$ distance from the sphere, at which point the momentum term and, to a lesser importance, the Reynold stress term provide adequate results.

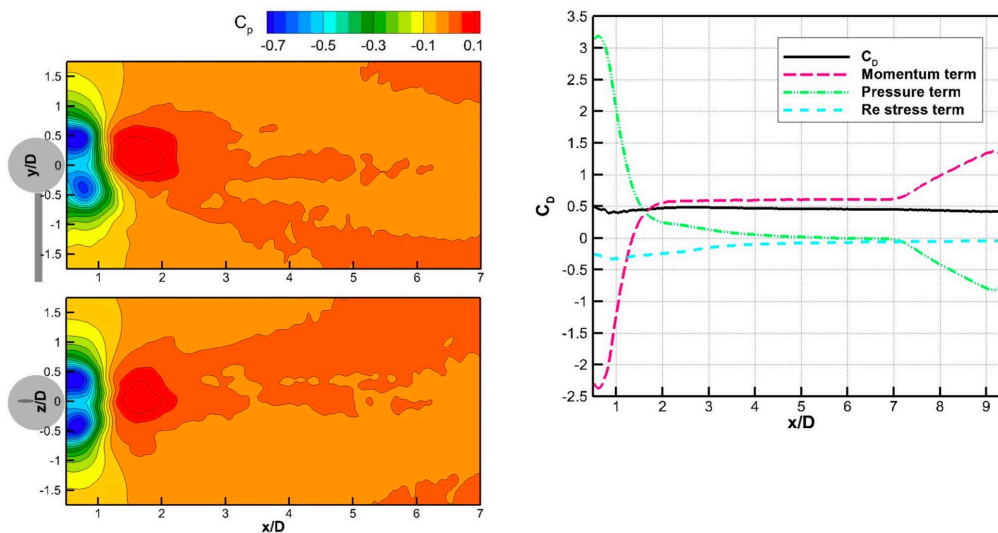


Figure 3.9: Left-hand side of the figure shows pressure distribution in the wake of a sphere, and the right plot shows C_D of a sphere as a function of the distance of the outlet plane from the sphere alongside individual contributions to the C_D (Terra, Sciacchitano, and Scarano 2017).

In the work (A. Spoelstra et al. 2021), the authors investigate the aerodynamic drag of an isolated cyclist and drag reduction of a trailing cyclist as a function of longitudinal and latter distance by utilizing the RoF. They achieved this by taking images of freestream before the leading cyclist (S_1 in figure 3.10), the wake between the leading and the trailing cyclist, S_2 , and the wake after the trailing cyclist, S_3 , to be used as an inlet and outlet planes for CVA.

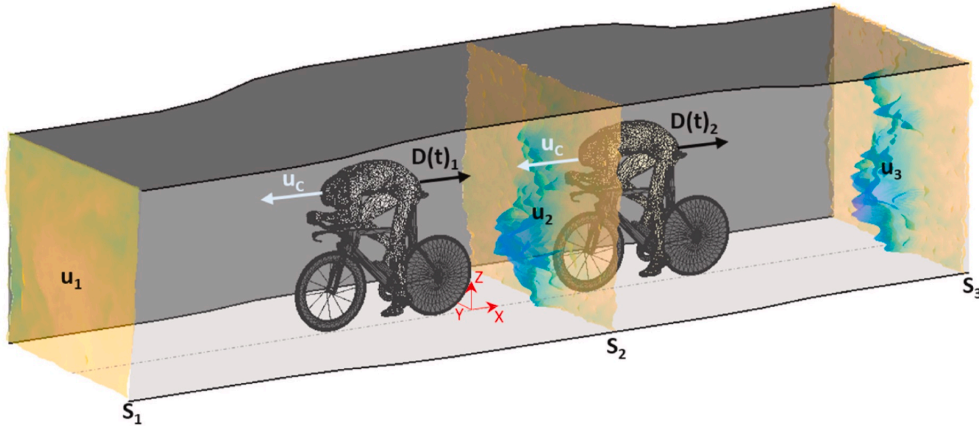


Figure 3.10: Schematic representation of the two cyclists in tandem and locations of the PIV images taken to be used as inlet and outlet for CVA. (A. Spoelstra et al. 2021).

The drag reduction of a trailing body obtained with RoF in figure 3.11 shows that results obtained with CVA match well with other studies and that the same trends can be interpreted when other methods are in use. Note that as described in the section on cycling aerodynamics, noticeable deviations between studies are visible due to various measurement tetchiness and cyclists used.

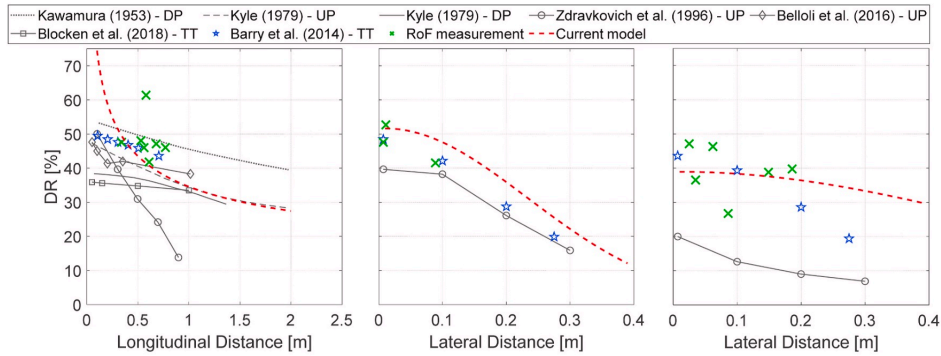


Figure 3.11: Drag reduction as a function of the longitudinal and lateral spacing between the two cyclists in tandem (A. Spoelstra et al. 2021).

3.9. Wind Tunnel

The primary objective of a wind tunnel experiment is to acquire knowledge about the aerodynamic interaction between a test object and a fluid under specific conditions. Usually, we are not interested in how that specific object performs in a specific wind tunnel, but we want to expand our newfound understanding to be applicable more generally in an unbounded flow.

The issue is that the conditions inside and outside a wind tunnel are not the same. This means that we need to account for the differences and apply modifications/corrections to the wind tunnel data for them to be applicable to the unbound free stream.

The corrections needed for the experiment vary based on the type of WT (closed test section, open jet), test conditions, and characteristics of the experimental object itself.

Our experiment will be carried out in a closed test section with parallel walls. The conditions will be subsonic and, with a Mach number below 0.3, can be considered incompressible. The models will consist of cylinders and cyclists, all considered bluff bodies. During the experiment, drag measurements will be performed.

In a closed section WT, the discrepancy between it and the free stream comes from the fact that when the flow encounters an object, the streamlines diverge around it. Outside, the streamlines have infinite space to move into and far away, so it can be considered that the flow is undisturbed by the introduction of a new object. On the contrary, in a closed loop test section, the flow does not have infinite space

to move into as it is bounded by the walls. The addition of a new object and its specific size reduces the volume through which the flow can move. The flow around it now has to accelerate to satisfy the conservation of mass, which would not be the case in an unconstrained flow. These effects can be more or less pronounced depending on the ratio between the object's size and the WT cross-sectional area, also known as the blockage ratio. It can have an effect on local measurements like pressure distribution over the circumference of a cylinder, as well as more global values like drag forces measured with a balance (Pope and Harper 1966).

For our specific case, there are three sources to be considered when applying corrections (Sinnige and Eitelberg 2021):

- *Solid blockage*. This includes corrections required due to the addition of a model in the WT section.
- *Wake blockage*. This includes corrections that are required due to blockage as a result of the model's wake.
- *Buoyancy*. This includes corrections due to the increasing size of the flow blockage as the boundary layer develops and grows.

Different methods can be used to account for these effects. The most common ones include the method of images, measured variable methods, and 3D panel methods (Sinnige and Eitelberg 2021).

3.9.1. Cylinder Wind Tunnel Corrections

In our research project, a significant portion of the experimental effort will be dedicated to the study of cylinders. Given that cylinders are frequently utilized as bluff bodies in various applications, several investigations have previously been conducted on cylinder blockage correction methods..

Through time, many different methods have been developed. They all vary in accuracy, mostly based on the cylinder flow regime, and non is best in all conditions (Anthoine, Olivari, and Portugaels 2009). Many sources cite that the blockage ratio should not exceed 10%, and (Anthoine, Olivari, and Portugaels 2009) argue that in practice, the blockage effects of bluff bodies can be neglected when the blockage ratio is below 3%.

In their experiment (Anthoine, Olivari, and Portugaels 2009) compared different blockage models for cylinders of infinite height in a closed test section and found that the one from Allen and Vincenti (Vincenti 1944) and one from Maskell (Maskell 1963) performed the best in the sub-critical cylinder flow regime:

- Allen and Vincenti (Maskell 1963) derived a theoretical model that included assumptions about two-dimensional, inviscid, compressible flow in a close wind tunnel section. Their correction equation is:

$$\frac{C_{D,c}}{C_D} = 1 - \frac{\pi^2}{4} \left(\frac{S}{C} \right)^2 - \frac{C_D}{2} \left(\frac{S}{C} \right) \quad (3.44)$$

Where $C_{D,c}$ is corrected and C_D is the uncorrected drag coefficient, S is the projected area of the cylinder, and C is the projected area of the wind tunnel cross-section.

- Maskell (Maskell 1963) developed a semi-empirical model for a wake that is axisymmetric. It is based on the conservation of momentum and additional assumption about the test condition. It can be seen in the following:

$$\frac{C_D}{C_{D,c}} = 1 + \varepsilon C_D \frac{S}{C} \quad (3.45)$$

Where ε is an empirical blockage constant. The author found that for conditions that would match those of an infinite cylinder, the best fit was when $\varepsilon = 0.96$

The study of (Matejicka and Georgakis 2021) also showed that the modified Maskel III method performed well in the sub-critical flow regime and that it and the method of Allen and Vincenti provided a reliable estimate for cylinders with larger blockage ratios.

4

Experimental Setup

The present chapter aims to provide a comprehensive overview of the various components involved in the experimental campaign.

To this end, the chapter begins with a concise overview of the wind tunnel facility, followed by a detailed account of the cylinder models utilized for the experiment. This is followed by a section on balance and stereo-PIV measurement techniques and how they were utilized during the experiment. The chapter concludes with the test procedure and measurement objectives.

4.1. Wind Tunnel Facility

The measurement campaign was conducted at the low-speed open jet W-tunnel in the High-Speed Laboratory at TU Delft. The wind tunnel setup consists of an inlet plenum and the centrifugal fan, driven by the 16.5 kW electric motor. After it, the flow passes through a diffuser, where it decelerates before reaching the settling chamber, where it straightens. Depending on the conditions, the minimum available turbulence intensity is around 0.5% (TU Delft n.d.). Following the settling chamber, the flow enters the interchangeable converging nozzle, which allows for various cross-sections and maximal achievable free stream velocities before exiting the tunnel. Free stream velocity is measured with a pitot tube inside the WT.

For our experiment, we wanted to achieve Re in the region of 10^4 to 10^5 , which is where C_D is less sensitive to small changes and variations in Re as denoted in figure 2.4. Therefore, a converging nozzle with the exit cross-section of $0.40 \cdot 0.40m^2$ was chosen. This allowed for the maximal achievable freestream velocity of around $35m/s$.

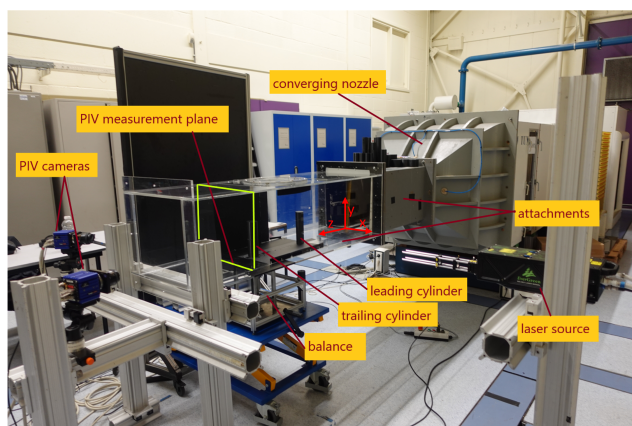


Figure 4.1: Wind tunnel experiment setup with the orientation of the coordinate system.

After the nozzle, a custom attachment was added that comprised of an initial solid section and a following transparent section that provided visual access to the cylinders and the flow. The cross-section

remained at $0.40 \cdot 0.40m^2$, and a big emphasis was put on the alignment of the individual parts to minimize the disturbance of the BI at the walls. The setup of the experiment can be seen in figure 4.1 alongside the orientation of the coordinate system that will be used later on.

As seen in the top-down scheme of figure 4.2, a bottom section of the WT attachment was replaced with the one with cut holes for the balance attachment and various screw-in positions of the leading cylinder. From this scheme and figure 4.1, it can be seen that the position of the trailing cylinder, and with it, the balance remained constant while the position of the leading cylinder upstream was varied to achieve the desired L . The distance between the trailing cylinder and the end of the converging nozzle was approximately $1.5m$.

The position of the PIV measurement plane also remained constant at the distance of $10cm$ behind the trailing cylinder.

Please note that the coordinate system with axis z pointing in the freestream direction will be used for the experiment, as seen in figure 4.2.

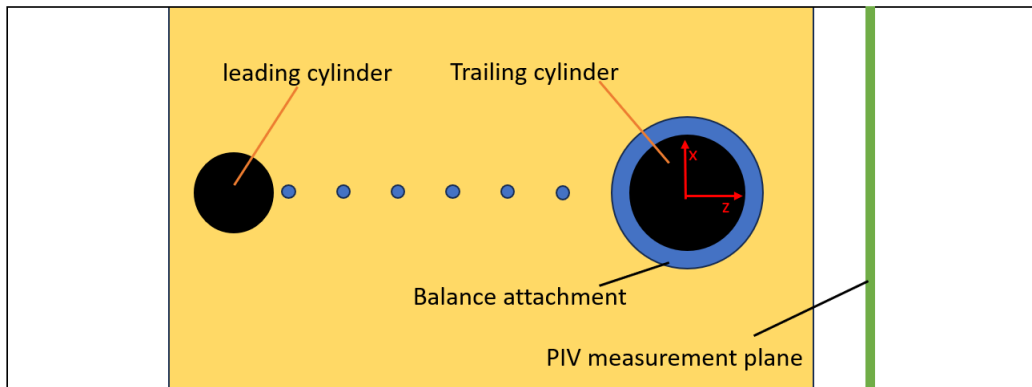


Figure 4.2: Scheme of the top-down look at the WT section where the measurements took place.

4.2. Cylinder Models

To achieve the research objective and answer the research questions, a set of cylinders had to be determined to explore all relevant degrees of freedom of the problem in question and provide the most insight. The limiting factor for the size of the cylinder was the blockage ratio, which should not exceed 10% of the WT cross-sectional area. The cylinder should also not be too small since it will experience lower absolute drag force and, therefore, larger relative measurement uncertainty. A combination of diameter and height was chosen that corresponds to the blockage ratio of 6 – 7%.

3 baseline cylinders with $AR = 1, 4, 6$ were chosen as seen in table 4.1. They represent three stages from an extremely three-dimensional cylinder with AR 1 to the one closer to two-dimensional at AR 6.

	AR	D [cm]	H [cm]	Blockage Ratio [%]
Cylinder 1	1	10	10	6.25
Cylinder 2	4	5	20	6.25
Cylinder 3	6	4	24	6

Table 4.1: Baseline Cylinders

They were used as leading cylinders and a baseline around which the diameters and heights of the trailing cylinder were determined. For each of them a cylinder with $\frac{D}{d} = 0.4, 0.6, 0.8, 1, 1.2$ and $\frac{H}{h} = 0.6, 1$ was also build. Here, D denotes a trailing cylinder diameter and d a leading cylinder diameter.

This gives a wide range of cylinders with varying AR to be tested in isolation to answer the first research sub-question and variations in diameter and height to address those in regard to tandem configuration. Baseline cylinders 2 and 3 were purposely placed closer together so that the results and conclusion based on those can be compared and used to give more confidence in the results.

Due to a large number of cylinders and the requirement for very specific dimensions, 3d printing was utilized. To speed up the process, two 3d printers were used. The first one is a FDM based printer Prusa MINI, and the second MSLA type Photon Mono X.

Models were firstly designed in CAD and then sliced in PrusaSlicer with 0.2 mm layer height for the Prusa Mini and in Lychee Slicer for Photon Mono X.

Models were designed with the ability to be screwed in from the bottom. Once printed, the parts were sprayed with a thin coating of matte paint to reduce reflections from the PIV laser. The figure 4.3 shows a set of cylinders.



Figure 4.3: A selection of cylinders used for the experiment.

4.3. Measurement Techniques

In this section balance and the stereo-PIV setup used will be explained in more detail.

4.3.1. Balance Measurements

An external two-component balance was positioned underneath the wind tunnel section, as seen in figure 4.4, to measure forces exerted by the flow on a cylinder.

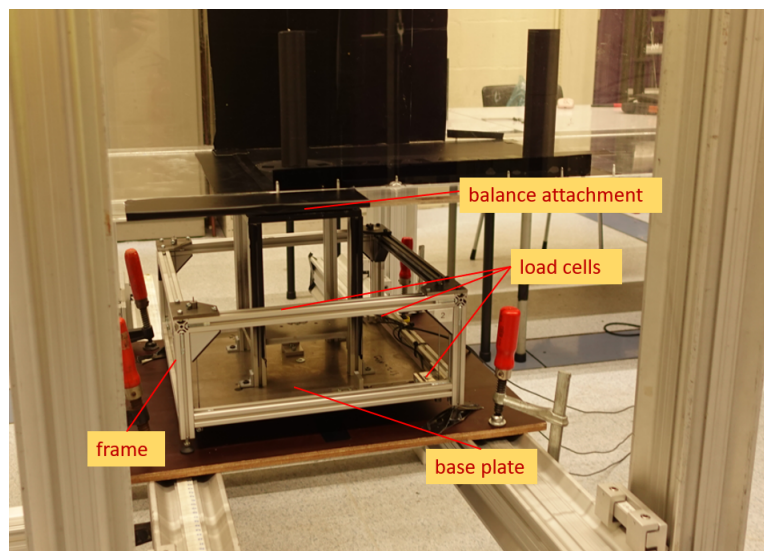


Figure 4.4: Balanced used for the experiment.

It comprises an external frame and a base plate connected together through the two load cells

aligned with the z , freestream, direction and one in x direction. On top of a base plate, a tower extending over the frame is positioned. To connect the balance to a cylinder, a special attachment was designed and 3d printed, as seen in figure 4.5, which rigidly attaches to the balance and the cylinder. The upper part of the attachment is smooth. Special care was taken in leveling it flat with the WT bottom section and having as small a gap surrounding it as possible to minimize flow leakage while still allowing for required small displacements.



Figure 4.5: Attachment connecting cylinders to the balance.

The working principle of the balance is as follows. As the cylinder experiences aerodynamic drag, the force exerted is transferred through the attachment and the tower onto the base plate. There, the force transfers to the load cell where the strain gauge sensor deforms as a result. This causes a change in resistance. The Wheatstone bridge picks this change in resistance as a change in voltage. A Data acquisition device samples this analog signal and sends it to a computer that is running a LabView program. With proper calibration, this change in voltage can be linked to a change in aerodynamic force.

Since we are interested in steady state results, each measurement was taken for a duration of 30s, with a sampling frequency of 500Hz.

The forces from the two load cells aligned in z directions are added together to get the freestream component. To determine the aerodynamic drag, the length of the force vector with x and z components is determined.

4.3.2. Stereo-PIV

Particle generation

To generate the particles required for PIV imaging, a SAFEX fog generator was used to produce a non-toxic water-glycol-based fog with a particle mean diameter of $1\mu m$. The fog generator was positioned before the WT inlet and left on for some time before measurements were taken. This was done to ensure consistent particle seeding inside the WT test section.

Luminance

Quantel Evergreen 200 laser was used to generate the required luminance, figure 4.6. Inside is a double-pulsed Nd:YAG laser. The device produced a 6 mm beam with a 532 nm wavelength at the exit. After a combination of the concave and convex lenses, the beam was expanded into the 2mm thick laser sheet positioned 10 cm behind the balance. The lights were turned off for the measurement duration to increase the contrast between the illuminated particles and the background. To reduce reflections, matte tape was put on the sides of the WT section.

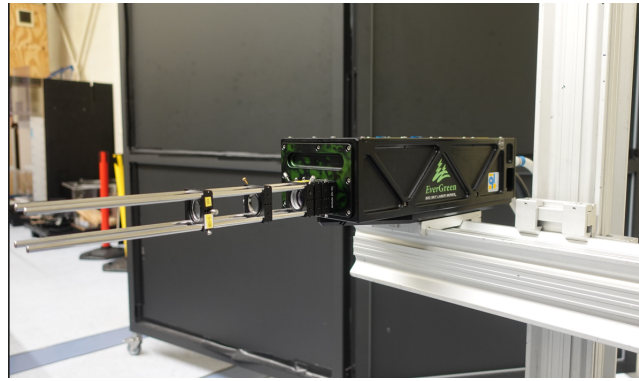
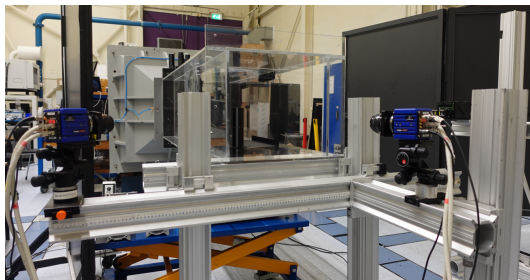


Figure 4.6: Pulsed laser used for the experiment with lenses used to expand and contract the laser beam.

Imaging

As mentioned in a previous section, a stereo-PIV dual camera setup is required. For this purpose, two LaVision's Imager sCMOS CLHS were used with 2560×2160 px image sensor size. The two cameras were positioned to the left and right of the WT section at the angle of roughly 90° , looking at the measurement plane without perturbing into the flow, figure 4.7 (a). To focus on the measurement plane behind the cylinders, two 35mm Focal Nikkor Lenses were used with the Scheimflug attachments to be able to better align the focusing plane with the measurement plane 4.7 (b).

The cameras were connected to the programmable timing unit, PTU, as did the laser, which provided accurate signal timing for imaging.



(a)



(b)

Figure 4.7: The two cameras focus on the measurement plane without perturbing the flow in Figure a). Lens connected to the camera through the Scheimflug attachments in figure b).

Acquisition setup

Cameras and the PTU were connected to a computer running DaVis 8.4 through which the PIV setup was interfaced.

Once the physical setup was completed, a multilevel calibration plane was put in line with the laser sheet, figure 4.8. This was firstly used to adjust the focus of the cameras and for the geometric calibration within DaVis to establish the geometric relations between the camera and the measurement plane, resulting in the scale factor of 7.135 px/mm.

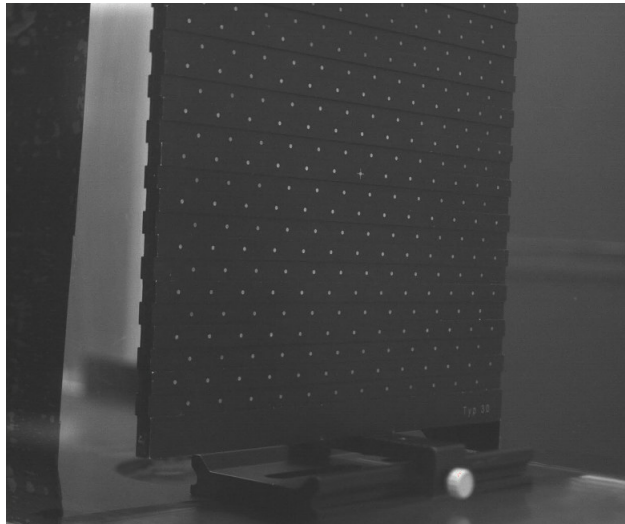


Figure 4.8: Multilevel calibration plate.

Imaging

After that was complete, the plate was removed, the WT was turned on, and the particles were let in. After they settled, multiple snapshots of the flow without any objects in it were taken. The time between consecutive images was varied based on the WT speed setting, but for freestream velocity of 25 m/s, it was set to $21\mu s$. This was then used to perform self-calibration inside DaVis.

For each run, 200 images of the wake were acquired at a sampling frequency of 15Hz, to be later used for averaging.

4.4. Measurement Campaign

The measurement campaign was conducted over the duration of 10 days. The first 3.5 days were spent setting up the experiment and calibrating the measurement devices.

Each day, before the start of data acquisition and at multiple stages throughout the day, PIV images of the freestream, WT data, and temperature and humidity values were acquired for comparison and nondimensionalization of values.

All measurements were repeated at three WT speed settings low $\approx 10\frac{m}{s}$, medium $\approx 20\frac{m}{s}$ and high $\approx 30\frac{m}{s}$ to account for any Re effects that might occur. Initially, the drag forces of all isolated cylinders was measured using a balance and images of their wake taken with stereo-PIV. For the three baseline cylinders, the wake was surveyed at multiple downstream distances between 10 and 50 cm from the measurement plane. Other cylinders were surveyed only at 10, 32, and 50 cm.

For measurements of the tandem configurations, the trailing cylinder remained constant while the leading cylinder was moved upstream. At the same time, images of the wake were taken. After those measurements was completed, some of the runs were repeated by having the trailing cylinder moved upstream to increase the distance between it and the PIV measurement plane.

Some measurements were repeated multiple times on various days to provide a point of comparison. The test matrix used for the experiment can be found in the appendix.

5

Data Reduction and Processing

In this chapter, the steps taken to determine the aerodynamic drag of cylinders from raw measurements will be explained in more detail. Firstly for balance and later in more detail for the stereo-PIV measurements. The latter will consist of initially obtaining the velocity field from the raw image and later applying it within CVA to determine the aerodynamic drag.

5.1. Balance Measurements Data Processing

As previously discussed in the chapter on the experimental setup, the three components of the balance were sampled continuously for a duration of 30 seconds. Subsequently, a Python script was employed to process the acquired data. Here, the individual components were firstly averaged over the duration of the measurements and then added together to get the combined aerodynamic force F_{aero} exerted by the flow on the cylinder. Corresponding information about the wind tunnel's freestream velocity, w_{wt} , and the temperature T were collected independently from the WT control computer. The latter information was used to determine the density of air ρ needed to determine the cylinder coefficient of drag C_D as seen in equation 5.1.

$$C_D = \frac{F_{aero}}{\frac{1}{2}\rho w_{wt}^2 A} \quad (5.1)$$

To assess the balance's repeatability, multiple measurements of an isolated cylinder were conducted on different occasions. Figure 5.1 displays the results obtained for the two distinct cylinders. Each line represents a specific run repeated at different WT velocities. Where there is only one point, the measurement was performed only at one WT velocity setting. In example (a) with cylinder $AR = 6$, it can be seen that results from the lowest WT velocity deviate significantly more than at higher settings. While this is not observable for (b), it was for the majority of other cylinders. The expected behavior should be more in line with (b) with negligible changes in C_D within this Re range. The most likely explanation for the higher spread of results is that at the lowest freestream settings, the velocity was half of what it was for the medium settings, resulting in only a quarter of the absolute force experienced by the cylinder in comparison. This means that the effects of measurement uncertainty are magnified more than in the case of a larger freestream velocity and absolute force. For this reason, the focus will be put on results from medium and high WT settings.

There, it can be observed that there is a slight offset between various runs with the standard deviation of around 4%, while gradients stayed more in line between the runs. The change in C_D with Re is negligible, which is the expected behavior for this span of Re based on the result from literature presented in Chapter 2.

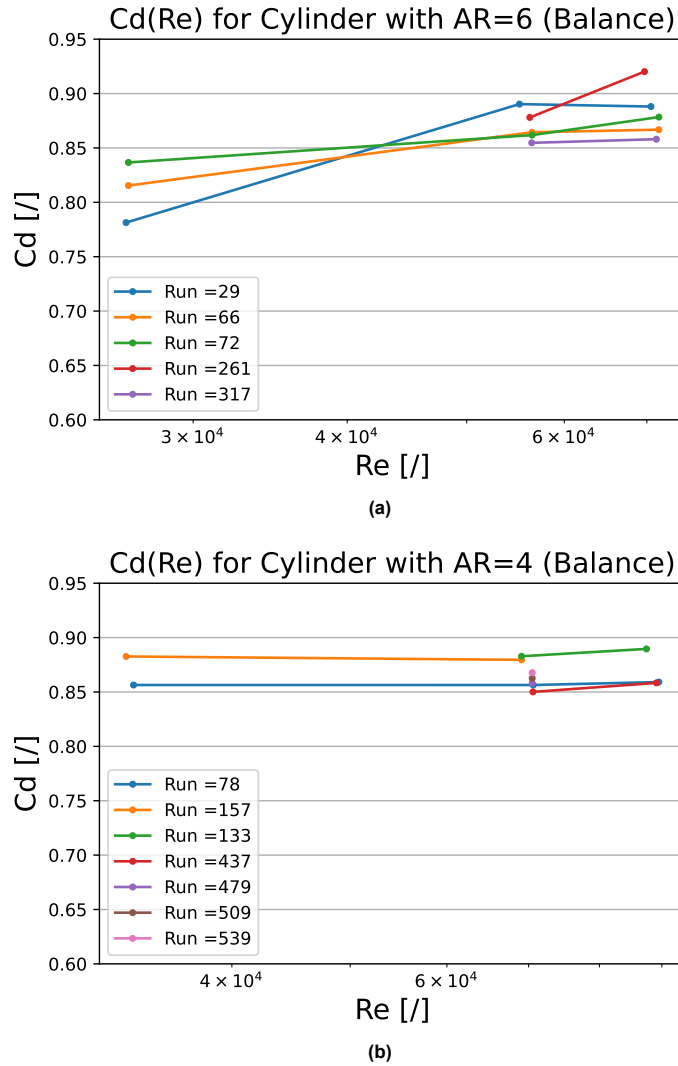


Figure 5.1: $C_D(Re)$ for the two isolated cylinders. Each line represents a specific run repeated at different WT velocities. Where there is only a point, the measurement was performed only at one WT velocity.

5.2. PIV Data Processing

This section will explain the process of obtaining a velocity field from stereo-PIV images.

5.2.1. Light Reflection

In the initial stages of the experiment, it became apparent that the transparent sides of the wind tunnel section introduced notable reflections, leading to a significant decrease in the contrast between the particles and the background. That led to reflections in certain regions near the section walls, overwhelming the refracted light from the particles. To mitigate it, matte black tape was put around the sides. Implementing this resulted in a considerable improvement in the measurements. However, it is worth noting that despite these efforts, a few reflections still persist near the bottom and the side, as evident in Figure 5.2 (a) below. Reflections were also observed from some of the cylinders, especially those with smaller diameters and especially where the distance between it and the laser sheet was the closest (10 cm), Figure 5.2 (a). In such instances, the presence of reflections introduces errors in the velocity field, as depicted in Figure 5.2 (b). These errors will subsequently impact the accuracy of the results obtained through the control volume approach. As the distance between the cylinder and the PIV measurements plane increased, the reflections disappeared.

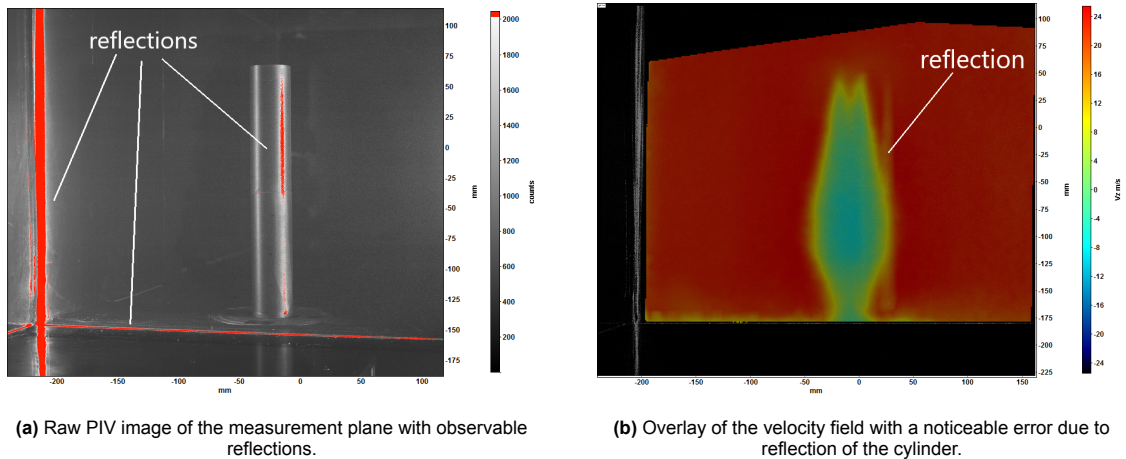


Figure 5.2: Raw PIV image and that image overlaid with the computed velocity field.

5.2.2. PIV Post-processing Settings

Once the images of the wake were acquired, they were processed with DaVis 8.4. For post-processing, the subtract minimum time filter was first applied over all 200 raw images to minimize background noise. Then, a stereo cross-correlation was applied with two passes. The first consisted of a rectangular 128×128 px interrogation windows with 25% overlap. This was then followed by a second pass with a circular 32×32 px interrogation windows and 75% overlap. This was chosen based on the recommendation from the literature and with some testing. Once the images were processed, they were averaged out to determine the quasi-steady state and the fluctuating term of the velocity field. An example of the u, v, w component of a velocity field can be seen in figure 5.3.

5.2.3. Domain

Velocity fields obtained from DaVis were roughly the size of 350×250 mm, as can be seen in 5.2 (b) and 5.4. To limit the noise that some velocity fields experienced near edges, the largest rectangle that did not include the artifacts of the processing was inscribed in the velocity field, which reduced the domain to 300×220 mm.

Velocity fields of the velocity vector components and the fluctuating term corresponding to the stream-wise turbulent kinetic energy for an isolated cylinder where the PIV measurement plane was positioned 50 cm behind the cylinder can be seen in figure 5.3.

Looking at w , (a), and w' , (b), the wake appears to be fully contained within the measurement domain even at larger downstream distances from the cylinder. While looking at u , (c), and v , (d), it can be seen that the velocities do not recover to freestream values near the edge. These two velocities are used to determine the pressure field, which means that the pressure will not recover to free stream pressure around the edge, resulting in one of the CVA assumptions not being fully satisfied. This will be explored in more detail in the following section on CVA.

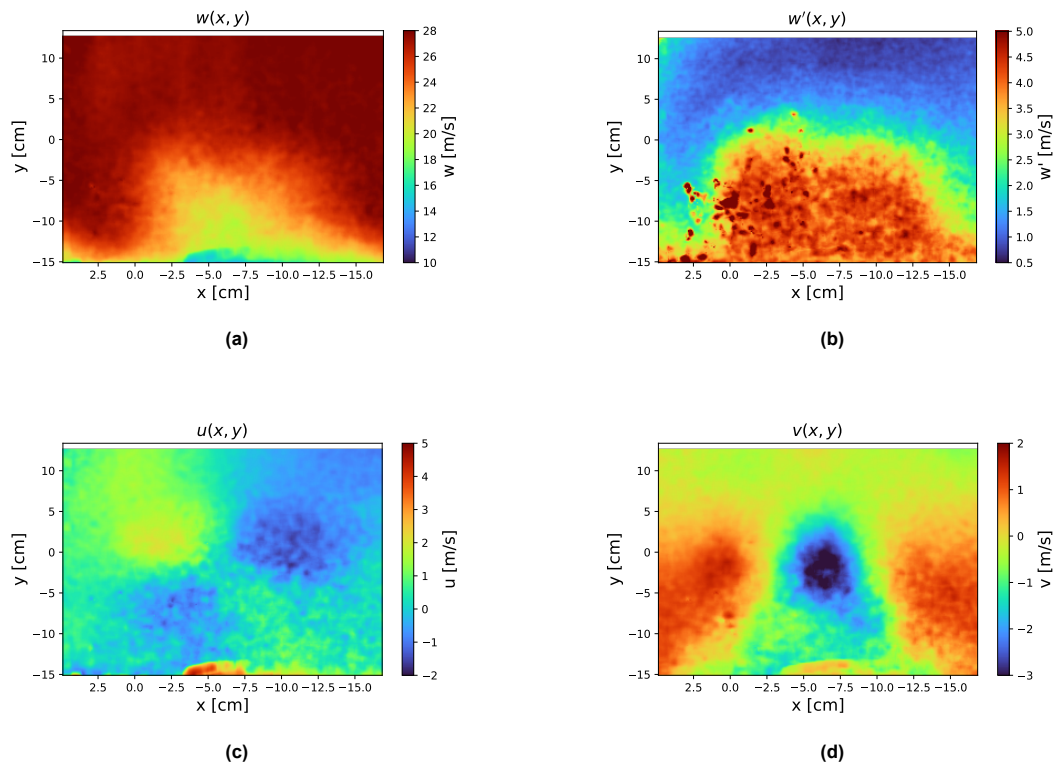


Figure 5.3: Velocity fields for individual components of the velocity vector for the isolated cylinder with $D = 5$ cm $H = 20$ cm and the distance between its center and PIV measurement plane 50 cm.

5.3. Freestream

This section will explore and compare the freestream obtained with PIV with values obtained from the WT control computer.

As discussed in a previous chapter, PIV measurements were performed at three wind tunnel velocity settings. PIV images of the freestream were taken before any cylinders were placed in the WT section. Aside from performing necessary PIV self-calibration, this was done to be used as an inlet plane for the CVA and for comparison to the free stream velocity obtained with the WT Pitot tube.

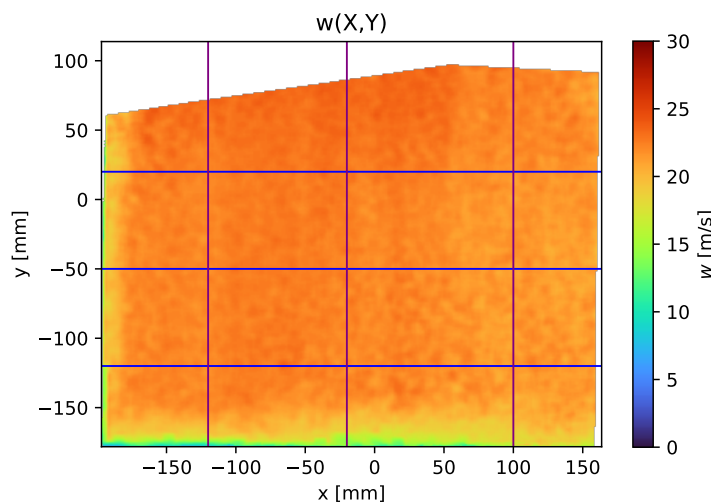
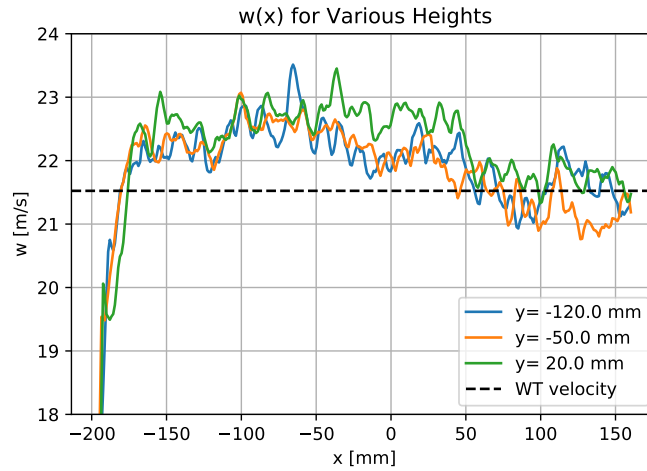
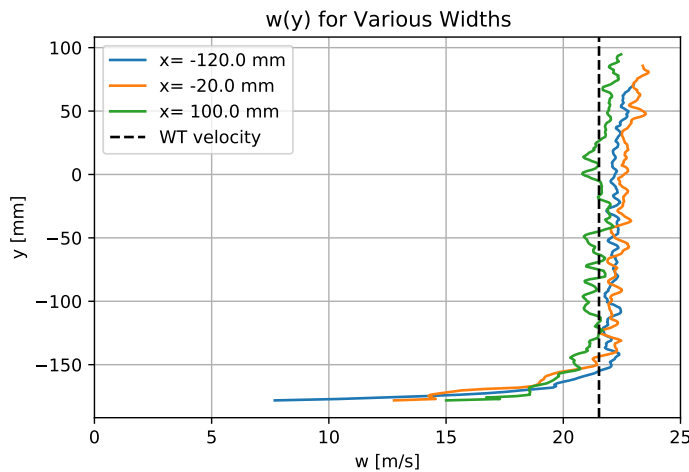


Figure 5.4: Freestream velocity component of the freestream velocity field, overlaid with lines that signify which sections were examined in figure 5.5.

An example of a freestream velocity component of the velocity field at the medium WT setting can be seen in figure 5.4. Blue horizontal lines overlaying the velocity field corresponding to $w(x)$ in figure 5.5 (a) and red vertical lines to the $w(y)$ in figure 5.5 (b).



(a) $w(x)$ for three heights y corresponding to the blue lines in figure 5.4. The dashed line represents the freestream velocity obtained with the Pitot tube inside the WT.



(b) $w(y)$ for three widths x corresponding to the purple lines in figure 5.4. The dashed line represents the freestream velocity obtained with the Pitot tube inside the WT.

Figure 5.5: Velocity profiles.

Average velocity was calculated by taking a section of the velocity field bounded by the top and bottom horizontal lines and left and right vertical lines. Results alongside freestream velocities obtained from the WT Pitot tube can be seen in table 5.1.

WT setting	u [m/s]	v [m/s]	w [m/s]	w' [m/s]	Pitot tube (w_{WT}) [m/s]	$\frac{w}{w_{WT}}$
Low	0.089	0.104	10.349	0.264	10.002	1.035
Medium	0.236	0.239	22.197	0.869	21.061	1.054
High	0.301	0.25	27.71	0.908	26.634	1.04

Table 5.1: Average freestream velocities obtained with PIV and Pitot tube for the three different WT settings.

Several observations can be made from these results. Firstly, the alignment of the measurement plane with the freestream is good since out-of-plane components comprise only 1 – 2% of the size of the velocity vector. Looking at figure 5.5, we can observe a slight negative velocity gradient from left to

right and from top to bottom. This was observed again at the low WT setting but not at the high settings. It can also be observed that velocity fluctuates on the order of 5%.

Comparing average velocities obtained with PIV and the Pitot tube, a measurable discrepancy between the two measurements can be observed. This can be attributed to the blockage inside the WT section where the PIV measurements were taken and in smaller part due to the calibration of the two devices. The two measurement devices were spaced quite far away. The Pitot tube was positioned before the contraction of the WT section, while the PIV measurement plane was located around 2 m behind. The BL on the walls grew between these points, which means that the flow inside had to accelerate to satisfy the conservation of mass. An increase in velocity due to this effect is also referred to as buoyancy. It is important that the same velocity is used for the nondimensionalization of the balance and PIV drag forces. While PIV measurements of the average velocity would be more accurate, since the measurements were taken closer to the cylinder position inside the WT section, to remove additional factor of uncertainty all drag forces will be nondimensionalized with the corresponding w_{wt} .

5.4. Aerodynamic Drag Force from PIV

In this section, the process of obtaining aerodynamic drag force from PIV velocity fields by utilizing the control volume approach will be explained in more detail. As derived in the previous chapter, equation 5.2 can be used to determine the aerodynamic drag force with the CVA.

$$\bar{D}_z = \rho \iint_{S_1} \bar{w}^2 dS - \rho \iint_{S_2} \bar{w}^2 dS + \rho \iint_{S_1} \overline{w'^2} dS - \rho \iint_{S_2} \overline{w'^2} dS - \iint_{S_1} \bar{p} n_z dS - \iint_{S_2} \bar{p} n_z dS \quad (5.2)$$

Here, the first two terms represent the change in momentum between the inlet and the outlet, the third and fourth a change in the RE stress term, and the last one is the change in pressure. All combined should give the aerodynamic drag, regardless of where the inlet and outlet planes are positioned, as long as the assumptions discussed in the previous section are satisfied. Before each term is explored in more detail, the conservation of mass will be addressed.

5.4.1. Conservation of Mass

As discussed in the chapter on CVA, to satisfy the requirements, conservation of mass needs to be enforced between the inlet and the outlet plane. This was achieved by calculating the mass flow of the outlet plane and then adjusting the size of the freestream inlet mask to match the mass flow of the outlet.

Two approaches were tested to determine the size of the domain. In principle, the outlet domain should only include the wake since taking a larger domain will result in an error manifesting as a reduction in calculate C_D (Spoelstra et al. 2021). Therefore, in the first test, the freestream velocity field was taken, and a mask was applied to isolate the wake from the freestream. An example of such a mask with the corresponding upstream plane can be seen in figure 5.6.

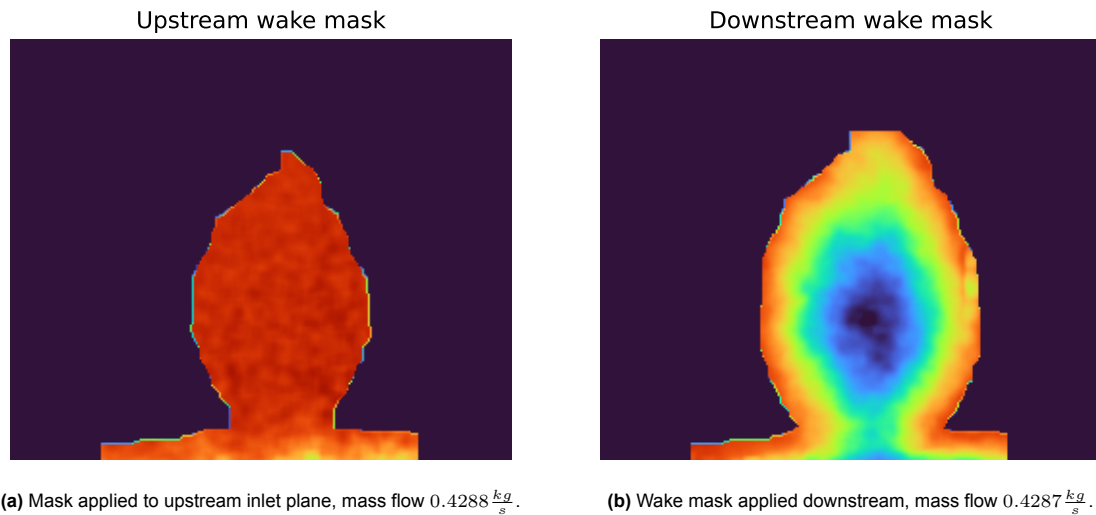


Figure 5.6: Images of the inlet and outlet with wake mask applied. Cylinder with $D = 4$ cm, $H = 24$ cm and the distance between it and PIV measurement plane 22 cm.

But as discussed in a previous subsection 5.2.3, the pressure is not fully contained within our PIV measurement domain. Therefore, for the second test, the largest possible domain of $300 \times 220 \text{ mm}^2$ was taken downstream, and again, the upstream plane was reduced to account for the conservation of mass. In principle, this should minimize the losses of the pressure term at the expense of slightly under-predicting the momentum contribution. Figure 5.7 shows an example of such a case.

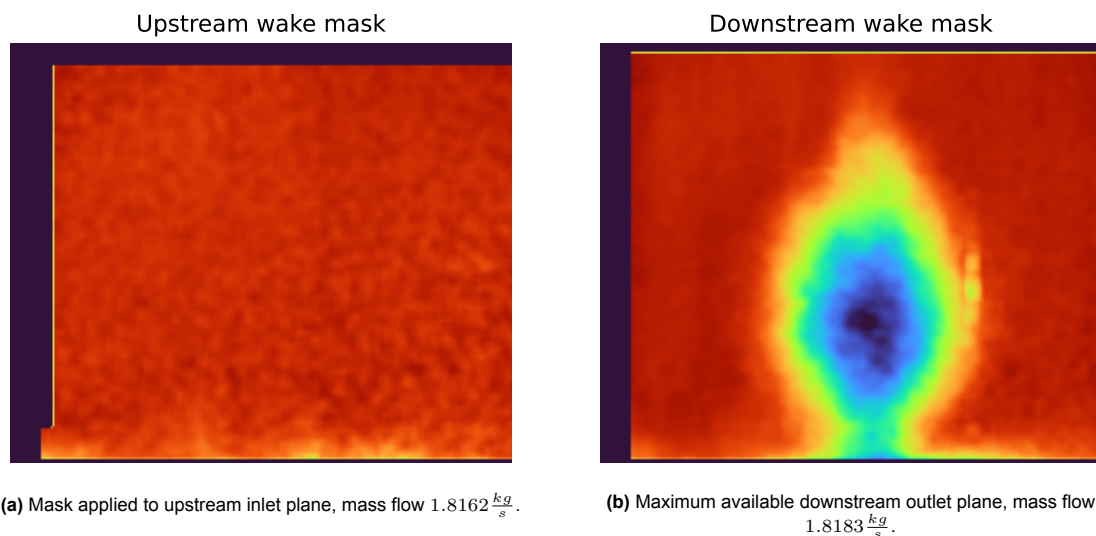


Figure 5.7: Images of the wake with the maximum available downstream outlet plane. Cylinder with $D = 4$ cm, $H = 24$ cm and the distance between it and PIV measurement plane 22 cm.

After applying these two approaches to various cylinders, the resulting C_D was compared. Between these two tests, there was a measurable difference in the calculated drag force coefficient. Apart from C_D , the contributions from the individual momentum, pressure, and Re stress terms varied as well. Results, where the whole domain was taken, were more in line with expectations and smaller changes between different cylinders, indicating the larger stability of this approach. The expected trend of under-predicting momentum term was not clear. Based on these findings and the fact that the measurement domains are not significantly larger than the wake, it was decided that the second approach with the largest possible outlet plane would be taken to generate results and conclusions.

5.4.2. Momentum Term

The first of the three terms to be considered is the momentum term, which represents the momentum deficit between the inlet and outlet plane as the flow passes the cylinder.

$$\text{Momentum term} = \rho \iint_{S_1} \bar{w}_x^2 dS - \rho \iint_{S_2} \bar{w}_x^2 dS \quad (5.3)$$

An example of such inlet and outlet plane can be seen in figure 5.8. We can see that the integral of the dynamic pressure is lower on the outlet plane than on the inlet, as expected. When nondimensionalized, this contributed 0.53 out of 0.69 for the total C_D of a cylinder (Note: the fluctuating term contributed a negative C_D as will be seen in the following subsection).

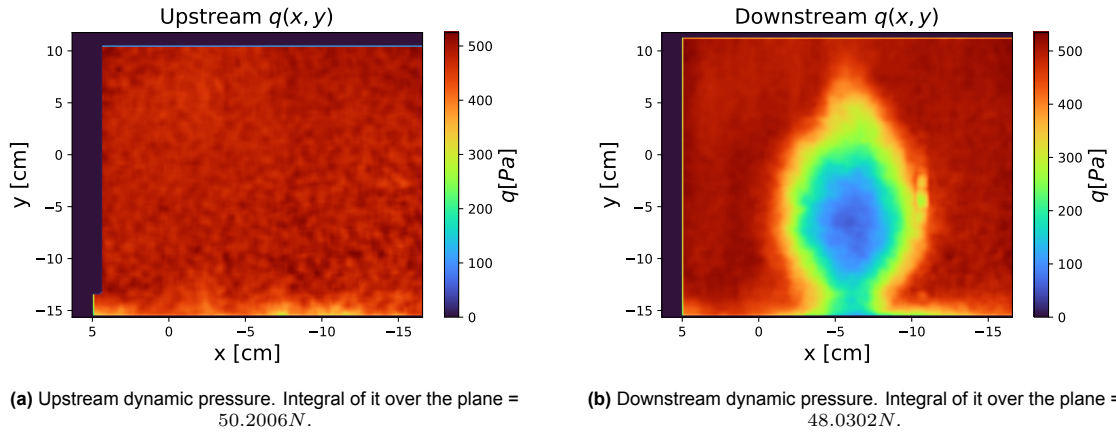


Figure 5.8: Images of the dynamic pressure distribution over the inlet and outlet. Cylinder with $D = 4$ cm, $H = 24$ cm and the distance between it and PIV measurement plane 22 cm.

5.4.3. Re Stress Term

Re stress term, also referred to as the fluctuating term, is the measure of turbulent kinetic energy in the streamwise direction, k_w .

$$k_w = \frac{1}{2} \overline{w'^2} \quad (5.4)$$

Its contribution to the overall drag can be determined from the following equation.

$$\text{Re stress term} = \rho \iint_{S_1} \overline{w'^2} dS - \rho \iint_{S_2} \overline{w'^2} dS \quad (5.5)$$

The streamwise fluctuating part $\overline{w'^2}$ can be easily obtained from the standard deviation of the w velocity field when two hundred runs were averaged after being processed.

$$\overline{w'^2} = \sigma_w^2 \quad (5.6)$$

An example of one such inlet and outlet plane can be seen in the figure 5.9.

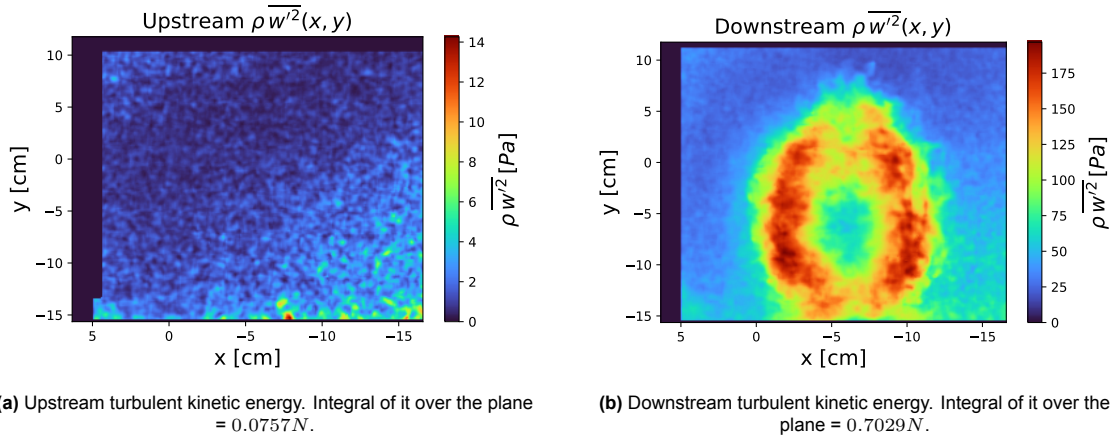


Figure 5.9: Images of the turbulent kinetic energy distribution over the inlet and outlet. Cylinder with $D = 4$ cm, $H = 24$ cm and the distance between it and PIV measurement plane 22 cm.

Looking at the figure, we can see that there is significantly more turbulent kinetic energy in the downstream plane. This is to be expected as the flow separates as it passes the cylinder. The highest concentration is not in the center but around the edge between the wake and the freestream, where we can find the detached shear layer. Since the fluctuations can only ever be positive, the overall contribution to the C_D is negative. For the cylinder example in the figure 5.9, this was -0.16 from the total 0.69.

5.4.4. Pressure Term

To determine the pressure contribution to the overall aerodynamic drag force, the following equations 5.7 need to be solved. Note that this equation assumes that the pressure on the contour of the inlet and outlet equals p_∞ so that pressure contributions from the sides of the control volume can be neglected, as discussed in more detail in a previous chapter.

$$\text{Pressure term} = - \iint_{S_1, S_2} \bar{p} n_z dS = \iint_{S_2} p_1 dS - \rho \iint_{S_2} p_2 dS \quad (5.7)$$

To determine pressure from the velocity field, a discretized form of the pressure Poisson equation was used 5.8.

$$\nabla^2 p = \left(\frac{\partial u}{\partial x} \right)^2 + \left(\frac{\partial v}{\partial y} \right)^2 + \left(\frac{\partial w}{\partial z} \right)^2 + 2 \frac{\partial v}{\partial x} \frac{\partial u}{\partial y} + 2 \frac{\partial w}{\partial x} \frac{\partial u}{\partial z} + 2 \frac{\partial w}{\partial y} \frac{\partial v}{\partial z} \quad (5.8)$$

Since measurements were taken only in one $x - y$ plane, gradients in the freestream z direction can not be determined. This means that the pressure can not be accurately determined in regions with high unsteadiness as is in the case directly behind the cylinder, but might still provide usable results further downstream as was discussed in the previous chapter 3.6. The equation 5.9 shows the terms that can be determined with a stereo-PIV setup.

$$\nabla^2 p = \left(\frac{\partial u}{\partial x} \right)^2 + \left(\frac{\partial v}{\partial y} \right)^2 + 2 \frac{\partial v}{\partial x} \frac{\partial u}{\partial y} \quad (5.9)$$

This equation requires BC to determine the pressure field. Different combinations of Neumann and Dirichlet conditions were tested, with the best results obtained when Neumann conditions were applied on all sides.

When Neumann conditions are applied on all sides, the pressure field can be determined only up to a constant. To account for this, a small reference area in the freestream was chosen on both the upstream and the downstream plane in the same location. Here, the velocity squared was averaged to get the $\overline{w_{up}^2}$ and $\overline{w_{down}^2}$ accordingly. For pressure upstream, p_{up} was set to 0. Any value can be chosen since we are interested in the difference between the two pressure fields and not the absolute value. Then a Bernoulli equation 5.10 was used to determine p_{down} . Once calculated, pressure fields were translated such that the pressure in reference areas matched p_{up} and p_{down} accordingly.

$$p_{down} = \frac{1}{2} \overline{\rho w_{up}^2} - \frac{1}{2} \overline{\rho w_{down}^2} + p_{up} \quad (5.10)$$

An example of an upstream and downstream pressure plane behind a cylinder can be seen in figure 5.10.

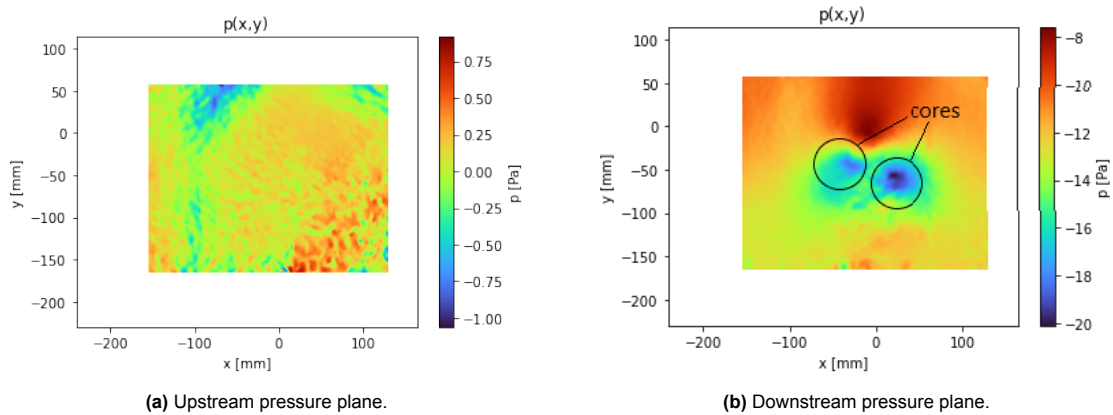


Figure 5.10: Pressure distribution on the upstream and downstream plane behind a cylinder.

To assess if the resulting pressure field matches the expectations, the vorticity, derived from the same velocity field utilized for pressure calculations, was visualized in Figure 5.11. It can be observed that the regions of low pressure match roughly to where there is a region of stronger clockwise and anti-clockwise vorticity. This vorticity results from the two vortices being shed from the free edge. This aligns well with the literature.

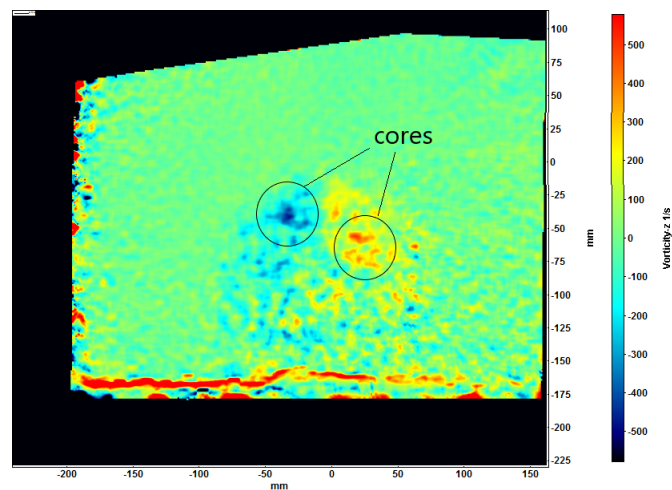


Figure 5.11: vorticity behind a cylinder with regions of clockwise and anticlockwise matching observations from the literature.

An additional example of a pressure field behind the same cylinder that was used for the Momentum and the Re stress term can be seen in figure 5.12. As designed to be, the contribution of the inlet plane is zero, while the outlet indicates a strong pressure deficit. The pressure term contributed 0.31 to the combined total C_D of 0.69.

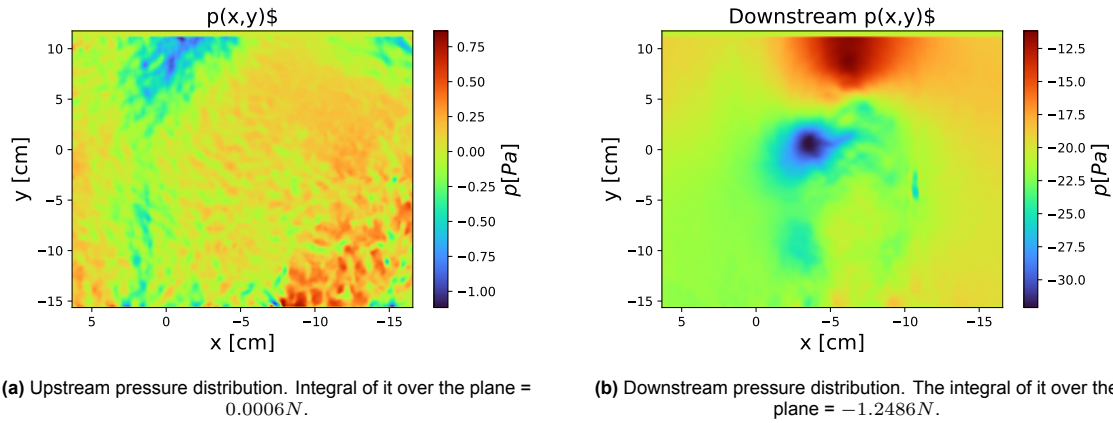


Figure 5.12: Images of the pressure distribution over the inlet and outlet. Cylinder with $D = 4$ cm, $H = 24$ cm and the distance between it and PIV measurement plane 22 cm.

Addressing the Pressure BC Issue

As discussed in a previous section, looking at figure 5.10 and 5.12, it is clear that the effects of the pressure are not fully contained within the domain. This makes it hard to find a region that can be considered freestream where the Bernoulli equation holds well. If the region is chosen, that is not part of the freestream but the wake, it can not be assured that the regions selected are part of the same stream tube, which will result in the incorrect determination of p_{down} .

Shifting the region where the Bernoulli equation was applied, in some cases, changed the pressure C_D contributions by more than 10%. This causes issues when trying to get the best estimate of the C_D and relative comparison between different cylinders. To test the influence of picking a region on the pressure C_D contribution, three different masks were created. The first one was a square domain in the upper right corner, the second a sleeve on the right-hand side of the domain, and the third one a region with one sleeve on the right and another on the left-hand side. Regions were selected in such a way that can be considered freestream, looking at the w velocity field. The pressure C_D contribution was calculated for different cylinders.

It was observed from the results that the discrepancy between the different masks was largest at close distances behind the cylinder and decreased as the distances between the measurement plane and the cylinder increased. This is to be expected since the pressure term contribution decreases and spreads more evenly across the domain. The one with a mask on both sides performed the best, with small perturbations in its size or position resulting in only small changes in C_D contribution.

CVA Domain Size Issue

Due to wake blockage present in the WT section, the velocity of the fluid increased between the inlet and outlet plane of the control volume. As a result of the increase in velocity, the pressure decreased. On the outlet plane, that does not present an issue since a deficit in C_D contribution from the momentum term due to blockage gets countered by the contribution from the pressure term.

But on the sides of the domain, this presents an issue. While there is no additional contribution from the momentum term, even if the velocity changes along the sides of the control volume, there is still no normal flow component to the control volume side, resulting in zero contribution. But a change in pressure can not be neglected. Looking at the equation 3.23, we can see that $p * n_z$ contributes to the drag force D . This means that the pressure would need to be integrated over the CVA's sides to satisfy all assumptions.

To investigate the effect of satisfying or not this assumption, we interpolated the pressure from the upstream inlet wake edge, figure 5.13 (a), to the downstream wake edge, figure 5.13 (b), resulting in figure 5.13 (c) when looked at from the direction of downstream. Since we are only interested in the integral of $p * n_z$, we only need to integrate the pressure over the projected area of the CV sides on the plane parallel with the inlet and outlet plane, figure 5.13 (c).

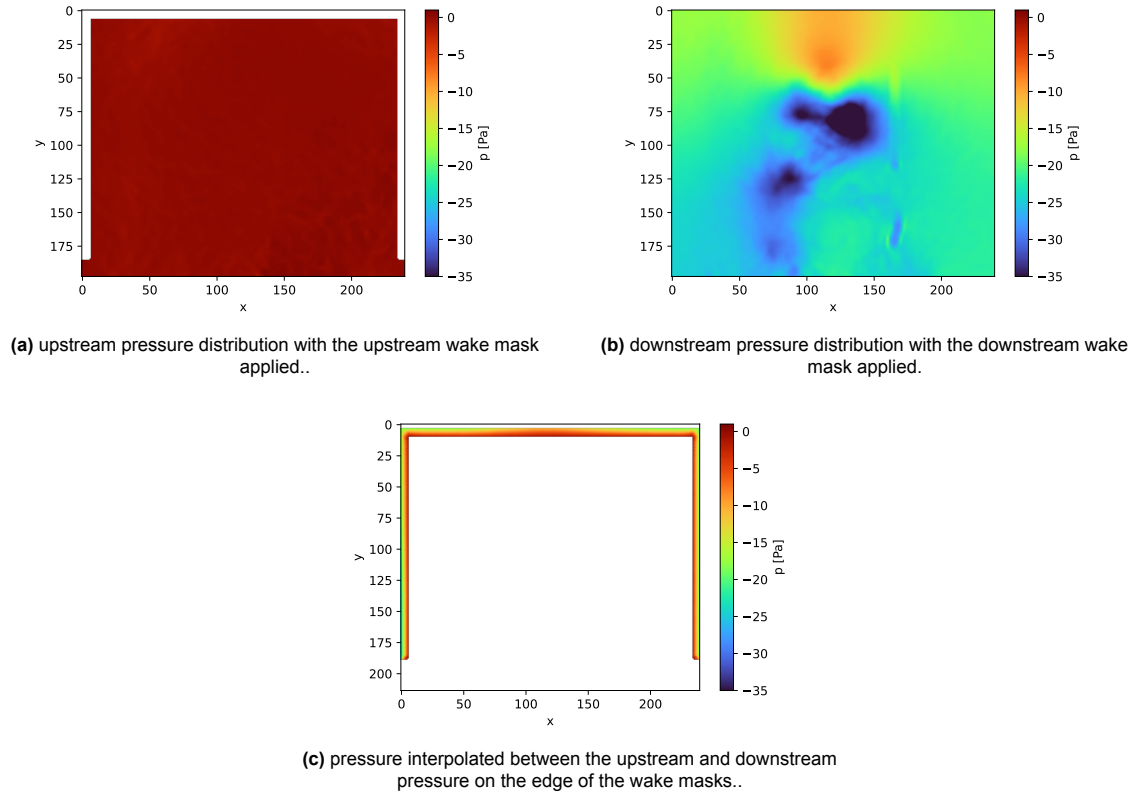


Figure 5.13: Pressure distribution along upstream and downstream planes.

In doing so, we have seen a small pressure term C_D contribution as expected, but it was inconsistent between various cylinders tested. Due to it being a small contribution and the fact that it introduces additional uncertainty, this will not be used in the calculation of the total C_D .

5.5. C_D from CVA

In this section, C_D , as a function of distance between the isolated cylinder and the PIV measurement plane, will be explored in more detail as well as individual contributions from the momentum, Re stress, and the pressure term.

To study this, PIV images of the wake were taken at multiple distances behind it for some of the cylinders. To be able to compare wakes of cylinders with varying diameters, the distance between the cylinder and the measurement plane was nondimensionalized and is denoted as L_{PIV} where:

$$L_{PIV} = \frac{\text{distance between the cylinder center and the measurement plane}}{D} \quad (5.11)$$

An example of wake progression for a cylinder with $D = 4$ cm and $H = 24$ cm that will be used for this analysis can be seen in figure 5.14.

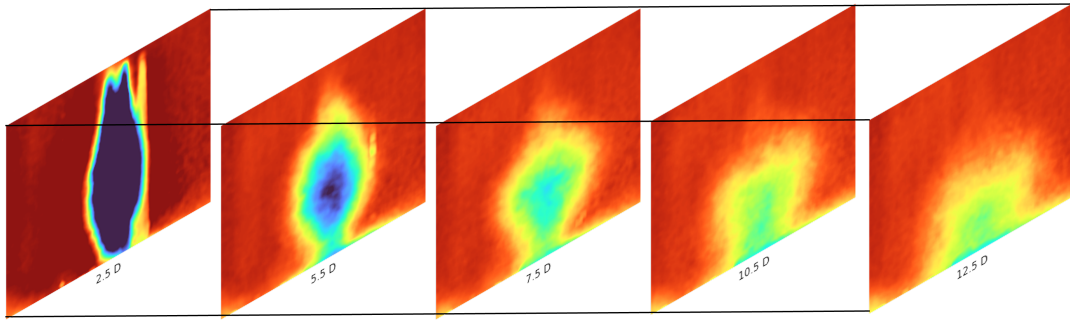


Figure 5.14: Images of the wake at varying distances behind the cylinder with $D = 4$ cm, $AR = 6$ and high WT speed setting. The images show the freestream component $w(x, y)$.

It can be seen from the wake development that even for the cylinder with $AR = 6$, the flow is still highly three-dimensional. The flow structures resemble that of a finite cylinder with $AR = 1$ discussed in a previous Chapter 2. Two counter-rotating vortices shed from the free edge move downwards before merging with the detached free shear layer from the sides of a cylinder and later expand and move outboard as they reach the ground.

As mentioned in a previous chapter, the position of the outlet plane should not have an effect on the drag estimate when CVA is applied. C_D as a function of L_{PIV} for the cylinder in figure 5.14 can be seen in figure 5.15.

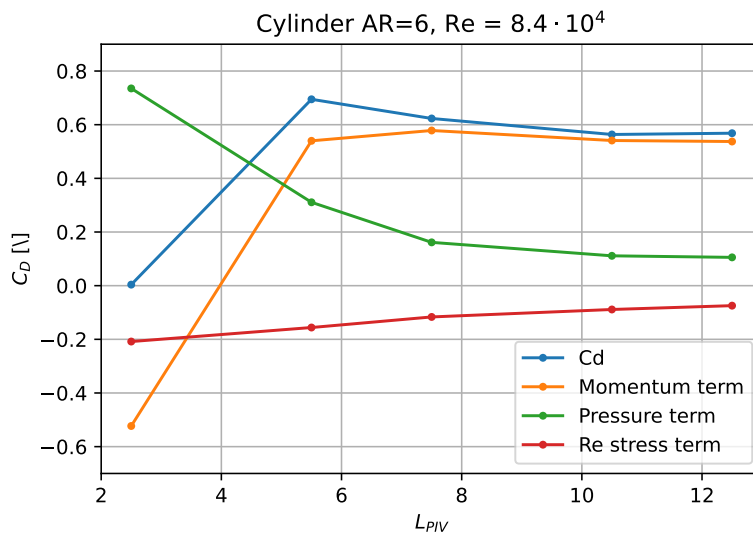


Figure 5.15: C_D as a function of L_{PIV} alongside individual contributions from the momentum, Re stress, and the pressure term.

The first measurement was conducted at $L_{PIV} = 2.5$, according to some past studies, as seen in table 2.1, still within the wake recirculating region behind the cylinder. This can also be inferred from the momentum term, which indicates a negative C_D contribution or thrust. Due to the shear layer being detached from the cylinder, combined with complex unsteady flow in the near wake, the contribution of Re stress tensors is non-negligible and negative in nature, as discussed in the previous section. The contribution of the pressure is significant due to low pressure within the wake. When all terms are combined, the resulting C_D is close to 0, which is not physical. This is mostly due to the pressure

term, which can not be accurately captured with this measurement technique due to the lack of ability to determine the freestream gradient, which is required to fully determine the pressure field.

As the L_{PIV} increases, C_D becomes more stable. Momentum term increases in its contributions and should, after a while, become the dominant contributor to the C_D , as it does. At an increasing distance from the cylinder, the pressure should converge back to freestream pressure, or in our case, due to increased blockage, to slightly lower pressure and a slight C_D contribution. As the distance increases, the fluctuations dissipate, and the contributions of the Re stress term should become smaller.

Looking at C_D , we see that it becomes more stable and constant as the distance increases, where it aligns well with the momentum term. Variation of around 4% after $L_{PIV} > 7$ could be explained with the uncertainties discussed earlier.

To better understand how the results vary between the cylinders and WT speeds, the same plot was reproduced for cylinders with $AR = 4$. In figure 5.16 (a), we can see the resulting C_D as a function of L_{PIV} for the two cylinders at two different WT velocity settings. In figure (b), we can see the same plot but with only momentum term C_D contribution. The nonphysical results at small L_{PIV} were removed for clarity.

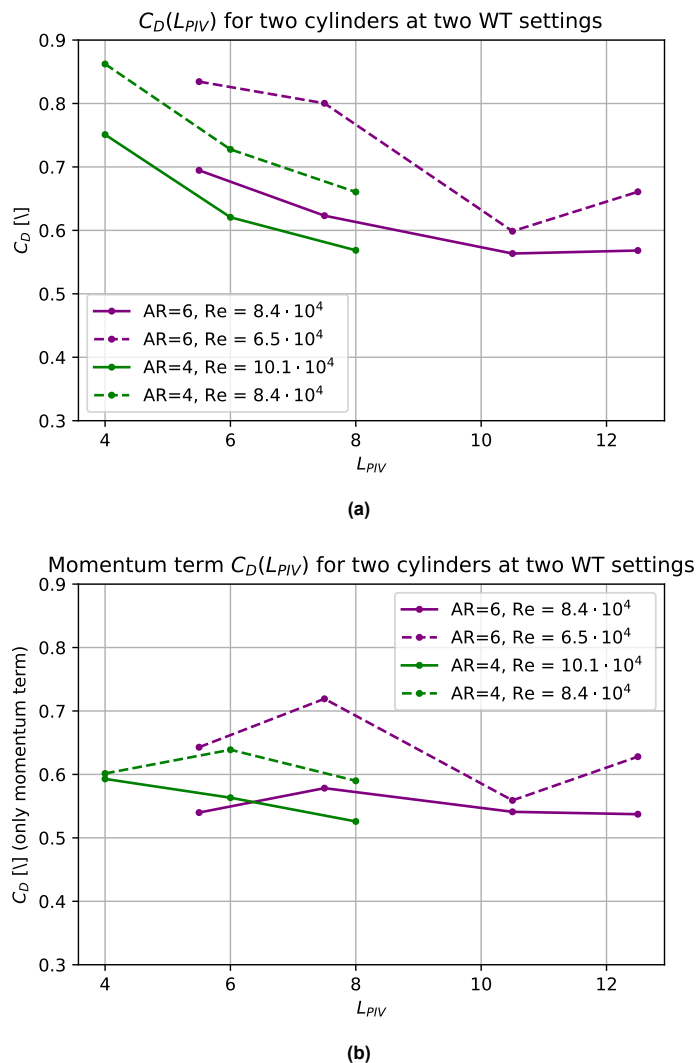


Figure 5.16: $C_D(L_{PIV})$ for the two cylinders at medium and high WT settings in figure a). Momentum term $C_D(L_{PIV})$ contribution for the two cylinders at medium and high WT settings in figure b).

From varying the WT velocity, it can be observed that in the case of both cylinders, there is a noticeable offset in C_D between the medium and high-velocity settings. At the same time, the trend is similar,

especially at higher L_{PIV} . Based on the literature and balanced results, there should not be a noticeable difference between the two. The offset between the two velocities WT settings could, in part, be explained by the velocities that were used for nondimensionalized. The alignment was significantly better when medium WT settings were scaled down by 1.2. When comparing figures (a) and (b), we can see that the spread of the results is smaller when only momentum contribution is considered. This is due to it not including the pressure term and its uncertainty at lower L_{PIV} . Apart from missing terms, the contributions of the momentum term are also under-predicted due to not having a wake mask and taking a larger than necessary outlet plane, which results in a reduction in C_D . When comparing the two cylinders in all cases at the same L_{PIV} the cylinder with the larger AR experiences larger C_D and momentum term contribution.

In the table 5.2 below a comparison between the results from literature and average C_D , obtained from the last two measurements for cylinders with $AR = 4$ and the last three measurements for cylinders with $AR = 6$, can be observed.

It can be seen that there is a large spread in the results obtained from the literature. In the case of high WT settings, the C_D value is under-predicted, while in the case of medium WT, the results lie somewhere in between.

	Cylinder and WT setting	PIV	goettingen	farivar_VLT	farivar_LT
C_D	AR=6, Re = $8.4 \cdot 10^4$	0.585	0.739	0.632	0.671
	AR=6, Re = $6.5 \cdot 10^4$	0.687	0.739	0.632	0.671
	AR=4, Re = $10.1 \cdot 10^4$	0.595	0.725	0.608	0.6344
	AR=4, Re = $8.4 \cdot 10^4$	0.694	0.725	0.608	0.6344
Only momentum term	AR=6, Re = $8.4 \cdot 10^4$	0.552	0.739	0.632	0.671
	AR=6, Re = $6.5 \cdot 10^4$	0.635	0.739	0.632	0.671
	AR=4, Re = $10.1 \cdot 10^4$	0.545	0.725	0.608	0.6344
	AR=4, Re = $8.4 \cdot 10^4$	0.614	0.725	0.608	0.6344

Table 5.2: Comparison between C_D results obtained with PIV and literature.

To sum it up, when it comes to absolute values, there is a lot of uncertainty, which makes it hard to determine the absolute value of C_D looking from PIV and the control volume approach with this experimental setup. But suppose the same WT setting is kept, and the results are compared at the same L_{PIV} , which should be positioned as far away as possible. In that case, this methodology should allow for relative comparison between the runs. Excepting that the momentum term will underpredict absolute value, it alone can be used for relative comparison between runs since it follows C_D closely at higher L_{PIV} due to the benefit of reduced uncertainty from not including the pressure term.

6

Results

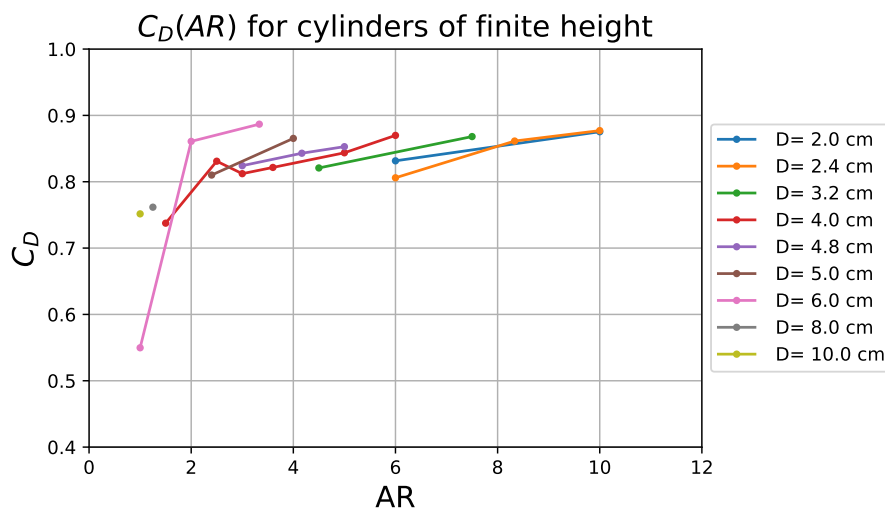
In this chapter, results from balance and PIV measurements will be presented. Each section addresses one of the research sub-questions. Firstly, the question is addressed with quantitative data obtained from the balance, followed by qualitative and quantitative data from the stereo-PIV setup.

6.1. Aerodynamic Drag of Isolated Cylinders of Finite Height

6.1.1. Balance Measurements

Cylinders of finite height vary among each other by a diameter D and height H or by one non-dimensional value, the aspect ratio AR . To quantify the effect of this parameter, $C_D(AR)$ is plotted in figure 6.1. In (a), only results obtained with balance are presented, while in (b), the same plot is overlaid with results obtained from the literature.

In the case of results obtained with the balance, each line represents cylinders with the same diameter but different heights to achieve a varying AR .



(a)

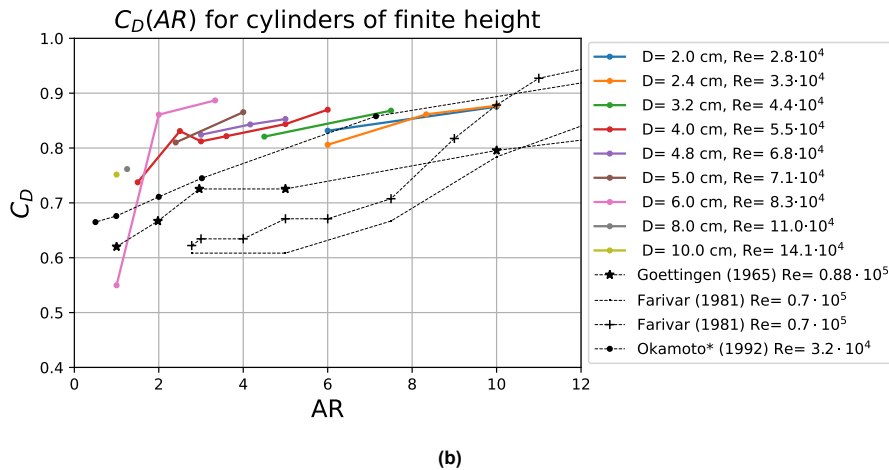


Figure 6.1: $C_D(AR)$ for selected cylinders obtained with a balance compared to results from literature.

Looking at balance results in figure 6.1 (b) two things can be observed. The first thing is that balance measurement gives C_D values that are higher than what sources from the literature would indicate. Secondly, the trend of increasing C_D with higher AR is not directly clear.

In principle cylinders of the same AR , but different D in H should experience the same C_D . Looking at cylinders with $AR = 6$ in figure 6.1 (a) but varying D and H , the spread of C_D is so large that it encompasses the third smallest and the second largest measured C_D . Therefore, looking just at individual data points does not give the expected trend of increasing C_D with increasing AR . It is only when we focus on cylinders of the same diameter but varying height, like in the example of a cylinder with diameter $D = 4$ cm, plotted in red, that we see the expected trend.

Since AR should be the only governing parameter of this problem, this discrepancy might indicate either that there is an additional governing parameter, like Re number, or that some effects did not scale when testing different cylinders.

Re Number

Apart from AR , Re number is the only other parameter that changes between different cylinders, as can be seen in the legend of figure 6.1 (b). This might indicate an additional governing parameter and is therefore worth investigating.

Since cylinders were tested at different WT velocity settings, we can compare $C_D(AR)$ plots from previous figures with the same plots done at higher velocities, and therefore, the only change is in the Re . Comparison for a selection of finite cylinders can be seen in figure 6.2. Looking at cylinders with the same diameter but increased Re , same color but line style, we see that it has a negligible effect on C_D ; otherwise, lines with the same Re but varying diameter would overlap. It can be concluded that, as expected, the Re number is not the governing parameter.

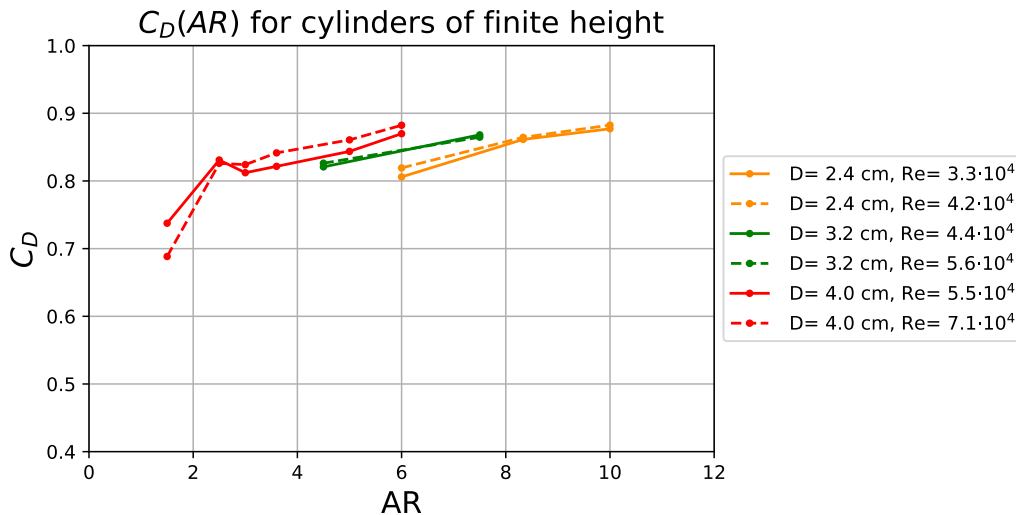


Figure 6.2: $C_D(AR)$ for selected cylinders with the same diameter at two different Re .

Nonscalable Parameters

Since there are no additional governing parameters, this variation in C_D at the same AR but different diameters must be explained somehow. Arguably, some of the variation is down to the uncertainty in the measurement chain. However, when cylinders of the same diameter but varying height are looked at, they all experience the expected increasing trend even though the changes in C_D between them are small.

This indicated that there might be additional differences between the runs that are not immediately clear.

The most likely explanation for the observation is blockage inside the closed WT section. For the three cylinders in figure 6.2, the corresponding blockage ratios are 2%, 3.8%, 6%. These values are fairly low but can not be completely neglected. At $AR = 6$, the cylinder with the largest blockage also saw the highest drag force, while the one with the smallest blockage also experienced the smallest C_D . This is consistent since higher blockage leads to higher induced axial velocities, increasing the negative pressure gradient and resulting in a larger over-prediction of drag.

The second thing that does not scale is the boundary layer that develops on the WT section floor. It remains at a constant height for all cylinders while the diameter of the cylinders varies, and therefore, the area of the cylinder exposed to the BL also varies. The potential effect of this on drag was not studied and would require additional experimental work to be carried out. No reference to this was observed during the literature study, which might indicate a negligible effect.

6.1.2. PIV Measurements

To determine C_D of an isolated cylinder from PIV, multiple images of the wake at varying distances L_{PIV} were taken. As was discussed in data reduction, to get the most reliable results, taking values at larger L_{PIV} is desirable. For this purpose, $L_{PIV} = 10$ was determined to be used since it was sufficiently far away. In cases where cylinders were not measured at exactly $L_{PIV} = 10$, but at a smaller and larger L_{PIV} , C_D was determined by interpolating between these two measurements.

Many measurements were unusable. This included all cylinders with a height of $H/h = 0.6$ where the wake of the cylinder would be lost in the BL and noise from reflection near the ground. In those cases, the spread of C_D values and the momentum term was very large. When all nonphysical results were removed, the remaining data points were plotted over the results from balance and literature in figure 6.3.

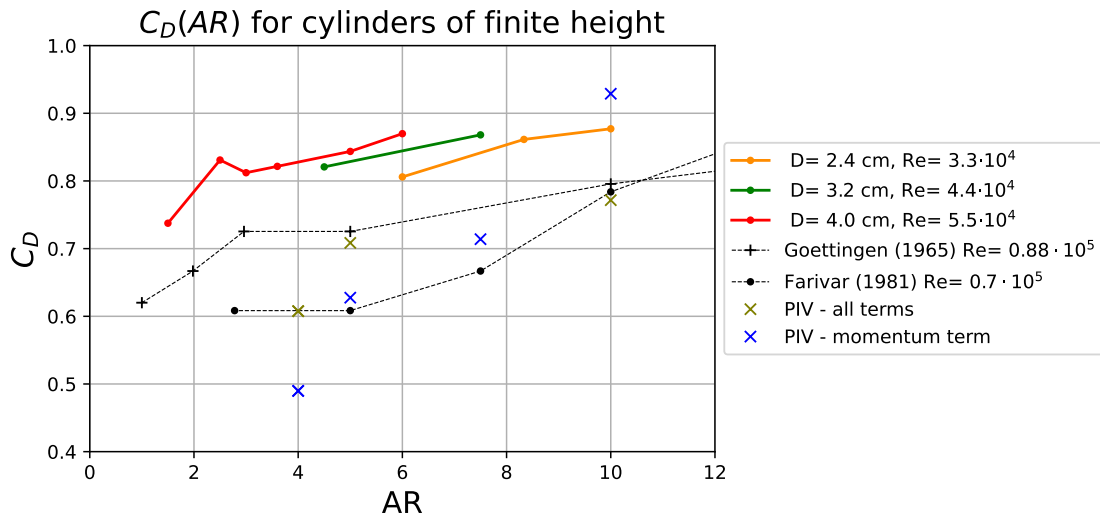


Figure 6.3: $C_D(AR)$ from different sources. Results from PIV were taken at $L_{PIV} = 10$.

a couple of things can be observed from this plot. Firstly, the PIV measurements follow the expected trend and results from the literature more closely than balance measurements. We can also see that the momentum term, which should be the dominant term at $L_{PIV} = 10$, shows a more clear trend than when all terms are included. To get a better perspective of what is going on, the momentum distribution of the corresponding cylinder's wake can be seen in figure 6.4. It can be seen how the wake at low AR resembles the wake of a finite cylinder, being spread more horizontally and with signs of tip vortices on the sides. This is in contrast with the wake of a cylinder with $AR = 10$, which resembles the wake of a 2D cylinder more, with only a small indication of tip vortices and the wake being more contained in width. It appears to have a small region of narrow, what appears to be 2D flow between the floor BL and the more three-dimensional wake at the top.

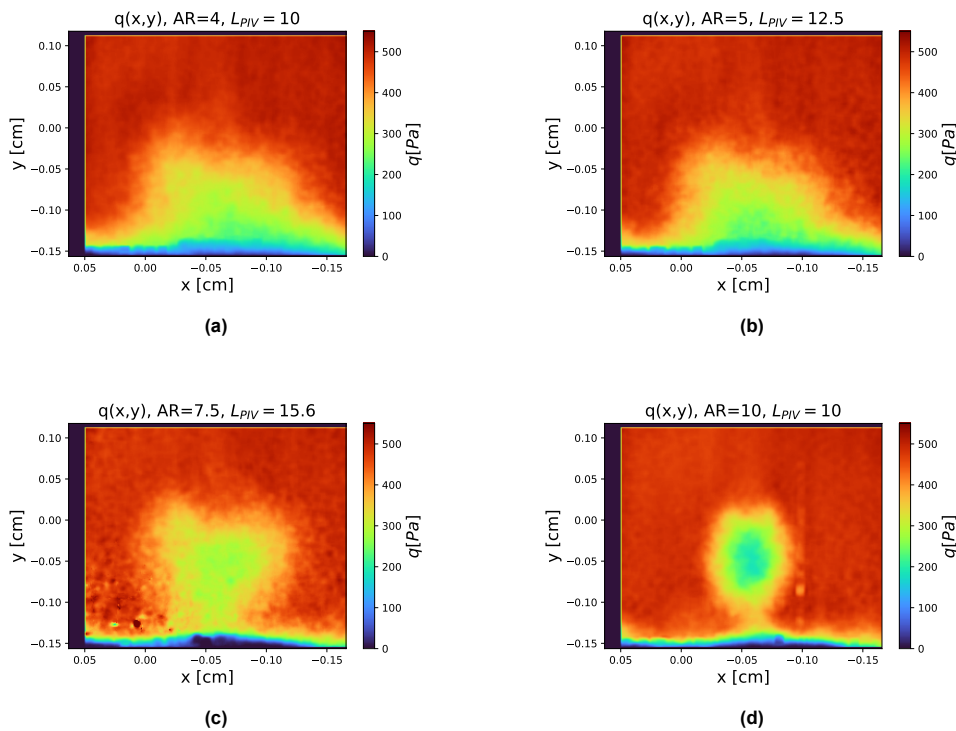


Figure 6.4: Dynamic pressure distributing behind cylinders of various AR at $L_{PIV} = 10$ or close to 10.

6.2. Aerodynamic Drag of Cylinders in Tandem

In this section, drag reduction, DR , of cylinders in tandem will be looked at in more detail. Firstly, drag reduction where both cylinders are of the same AR and later, where this also varies. As discussed earlier DR is defined as:

$$DR = \frac{C_{D,iso} - C_{D,tand}}{C_{D,iso}} \quad (6.1)$$

where $C_{D,iso}$ represents the drag of a trailing cylinder in isolation and $C_{D,tand}$ the drag when the trailing cylinder is part of a cylinder tandem.

6.2.1. Cylinders in Tandem of the same AR

As mentioned in the previous section, going from isolated cylinders of finite height to cylinders in tandem with the same AR , another variable, pitch ratio L , is introduced. It is defined as the ratio of the distance between the two cylinders and the diameter of the trailing cylinder.

$C_D(L)$ for the trailing cylinder in tandem configuration can be seen in figure 6.5, where each line represents a different pair with the same leading and trailing cylinder AR . Overlaid are results obtained from literature for 2D cylinders, or $AR = \infty$.

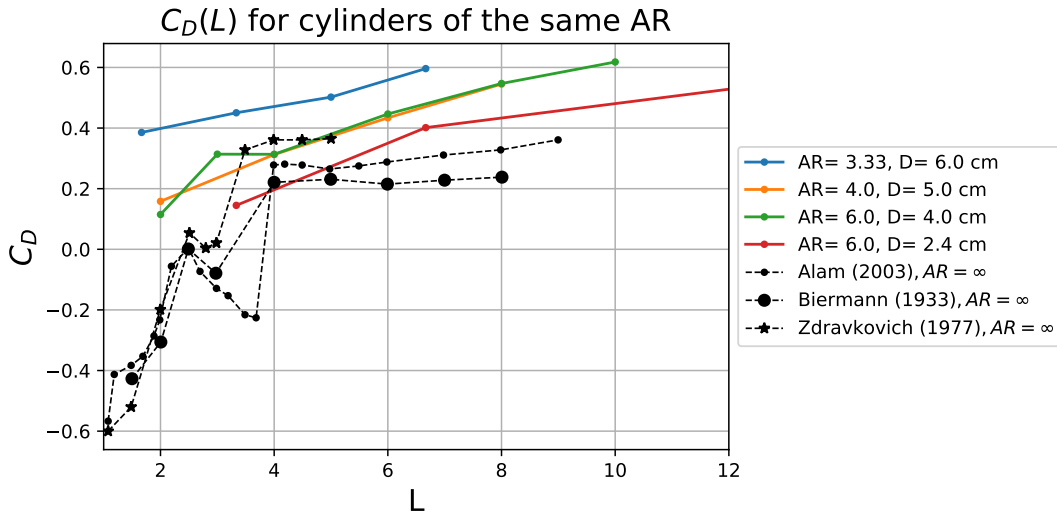


Figure 6.5: $C_D(L)$ for cylinders of the same AR , overlaid are the results from literature.

Looking at the figure 6.5, it can be seen that results obtained with balance follow the expected behavior, which is that as the L increases, C_D should converge to that of an isolated cylinder. It needs to be kept in mind that the results from the literature are for cylinders of infinite height, where three-dimensional effects are negligible. This is also why there is no observable intricate $C_D(L)$ at L below L_{crit} and no jump in C_D where there should be one for infinite cylinders. Note that the experiment was not designed for the exploration of small L . However, anecdotally, when a trailing cylinder was put close to the leading cylinder ($L \approx 1$) during the time that the WT was on, the trailing cylinder would remain in the wake of the leading cylinder, touching it, even when it was not screwed into the WT floor. A small but noticeable resisting force was experienced when removing it by hand. This correlates well with results from the literature, which state that at very small L , the trailing cylinder should experience a thrust force.

In figure 6.6 $DR(L)$ can be seen for the same cylinders. This is also the plot we are more interested in and will be used to present future results. We see the expected trend of lowering DR as the distance increases.

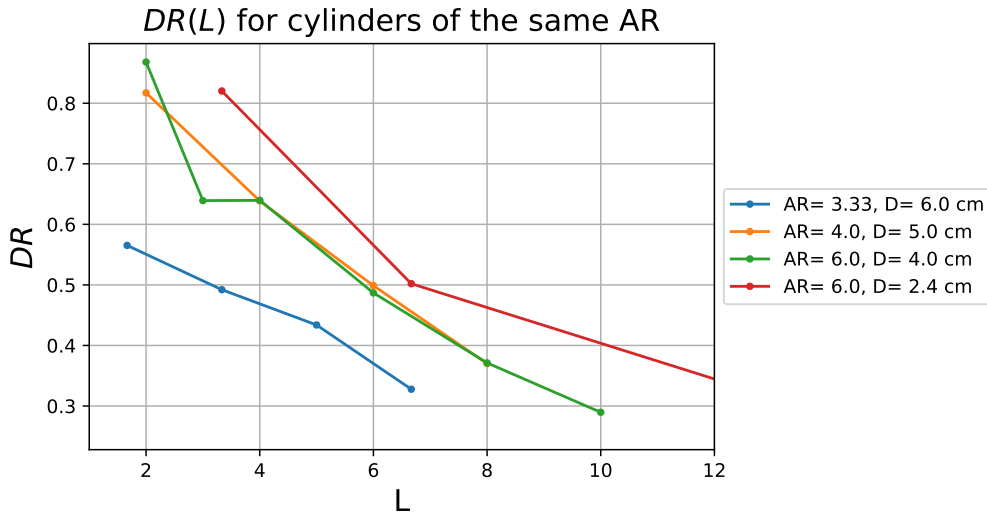


Figure 6.6: $DR(L)$ for cylinders of the same AR .

When focusing on results from the balance, individual lines do not overlap. It appears that cylinders with lower AR at the same pitch ratio experience smaller DR than cylinders with higher AR . To a certain extent, this could be explained by the three-dimensionality of the flow and its effect on the variation of upstream momentum deficit experienced by the trailing cylinder as a result of varying leading cylinders AR . This can be seen in figure 6.4. However, some variation in drag can also be attributed to different flow interactions between various wake shapes and the trailing cylinder, resulting in different tandem wake topology and trailing cylinder C_D .

Looking at the cylinder with $AR = 6$ in green, it can be seen that it is overlapping with a cylinder with $AR = 4$ and not $AR = 6$. This might be an indicator of the similar effect as seen in the isolated cylinder where cylinders with the same AR but varying D would not have the same C_D . This indicates that caution needs to be applied when making concrete conclusions.

6.2.2. Cylinder in Tandem of Varying AR

In this section, cylinders in tandem are expanded to include variations in the two cylinders AR . This expansion adds an additional variable, the diameter ratio D/d .

$$D/d = \frac{D_{trailing}}{D_{leading}} \quad (6.2)$$

The height ratio, H/h , will be used instead of AR in combination with the diameter ratio.

$$H/h = \frac{H_{trailing}}{H_{leading}} \quad (6.3)$$

To study these tandem configurations more systematically, a study of initially having a fixed leading cylinder with a varying trailing cylinder will be performed, followed by having a trailing cylinder fixed with a varying leading cylinder.

When we keep the leading cylinder constant and vary the diameter of the trailing cylinder, we get the following results in figure 6.7. In the subplot (a), the distance between the two cylinder centers has been nondimensionalized by the leading cylinder diameter L_{lead} whereas as in (b), it was nondimensionalized by the trailing diameter L_{trail} .

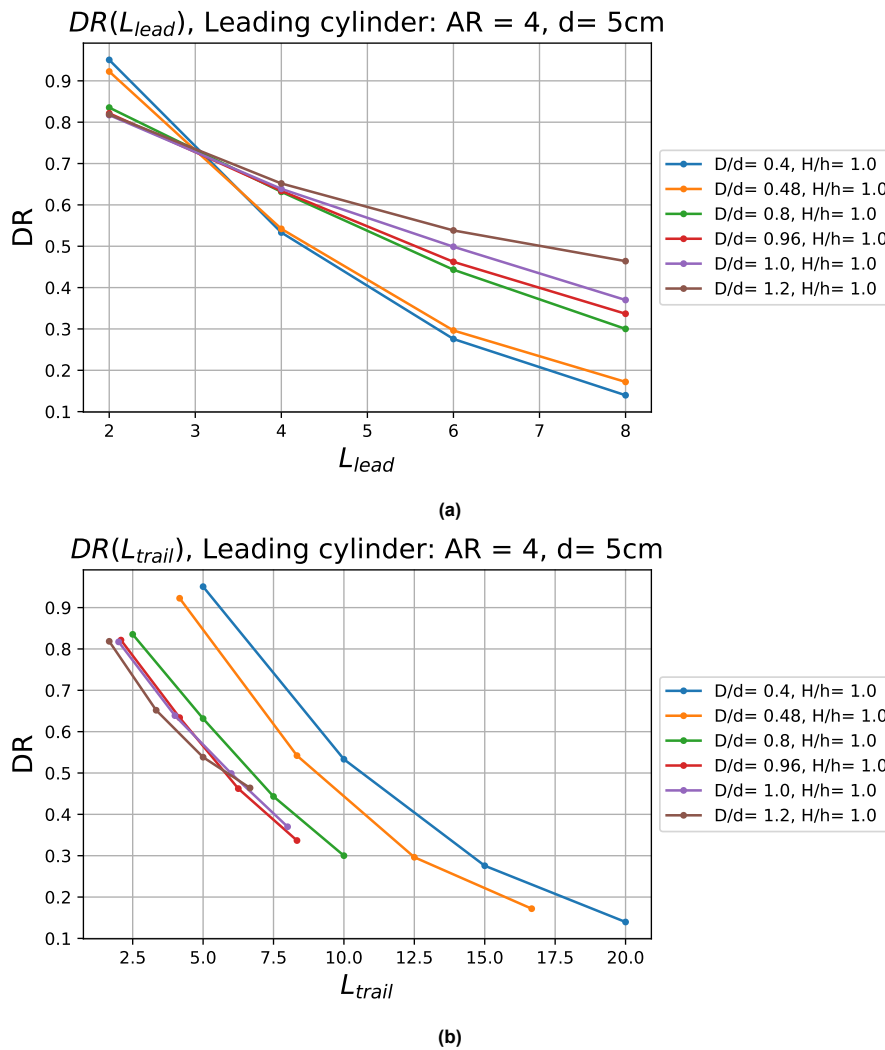


Figure 6.7: DR as a function of distance for the case where there was the same leading cylinder and the distance between them being nondimensionalized by the leading diameter L_{lead} in a) and trailing diameter L_{trail} in b).

At the same L_{lead} distance, trailing cylinders were exposed to the same part of the leading cylinder wake. This plot (a) is interesting as it indicates a trend that at short distances behind the leading cylinder, trailing cylinders with smaller diameters experience larger drag reduction. However, after a certain point, the trend reverses where cylinders with larger diameters experience a greater DR being submerged in the wake of a leading cylinder.

From a perspective of the trailing cylinder, figure (b), at a fixed L_{trail} , a slimmer cylinder will experience a larger DR .

The same trend was also observed with a different leading cylinder and can be seen in figure 6.8. Interestingly, the L_{lead} at which the trend reverses is pushed further downstream when the leading cylinder AR is larger.

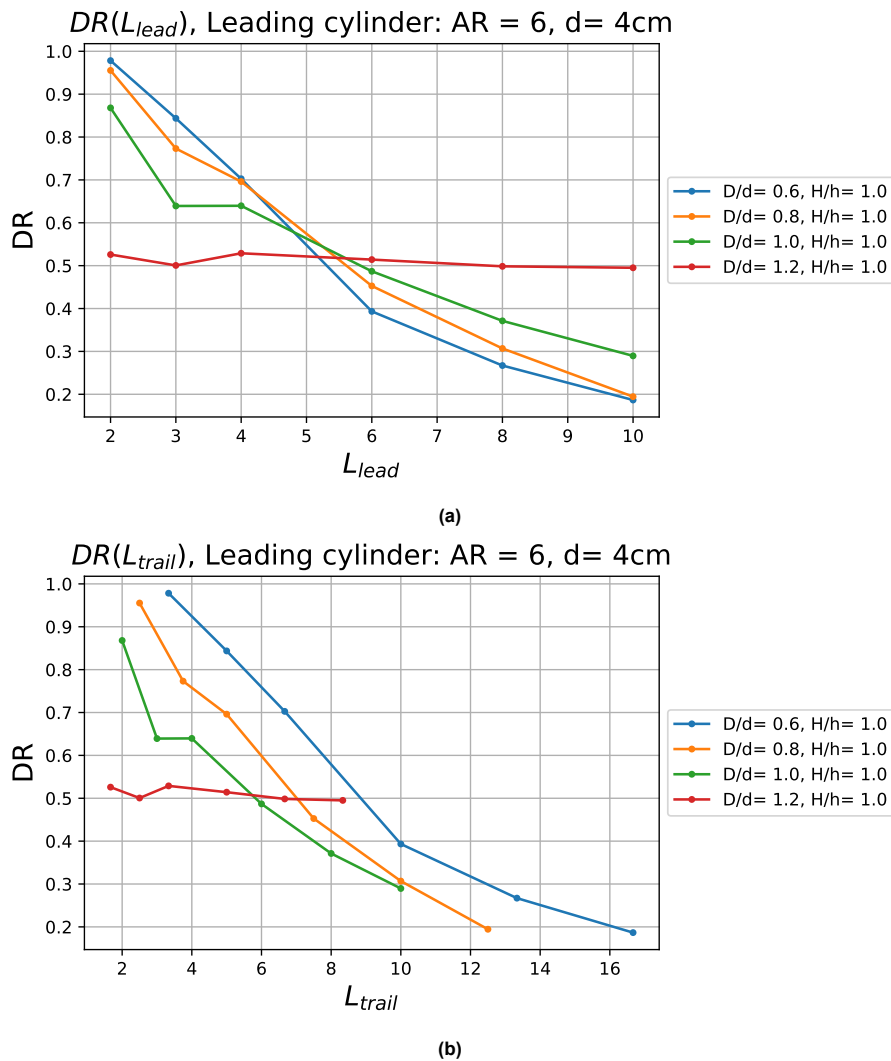


Figure 6.8: DR as a function of distance for the case where there was the same leading cylinder and the distance between them being nondimensionalized by the leading diameter L_{lead} in a) and trailing diameter L_{trail} in b).

The same plots were reproduced for the case where now the trailing cylinder is kept constant, but the leading cylinders were varied in diameter. One such result can be seen in figure 6.9.

When the distance is nondimensionalized by the trailing cylinder L_{trail} (a) it means that the absolute distance between the leading and trailing cylinder is the same, but the shape of the wake is different. As expected, the trailing cylinder experiences a larger drag reduction when being behind a cylinder with a larger diameter. When nondimensionalized by the leading cylinder diameter L_{lead} , it means that the trailing cylinder was submerged in the wake of a leading cylinder at the same relative distance; being behind a cylinder with a smaller diameter was more beneficial.

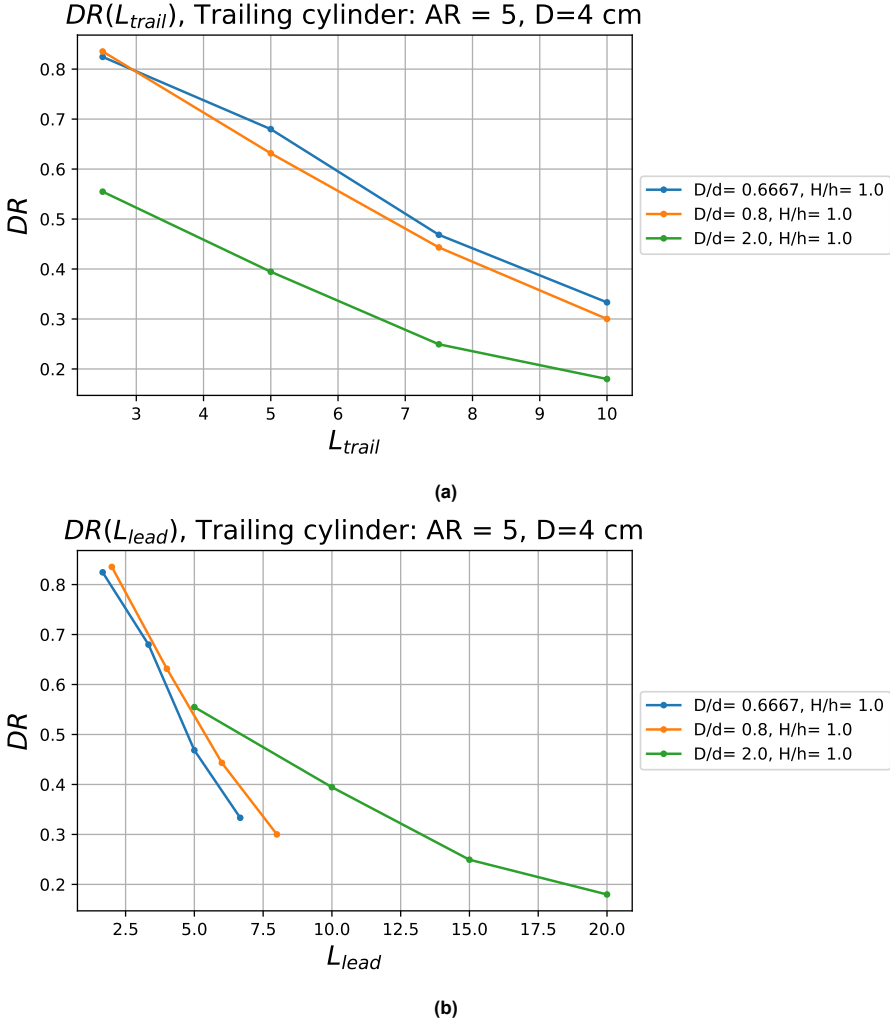


Figure 6.9: DR as a function of distance for the case where there was the same trailing cylinder and the distance between them being nondimensionalized by the trailing diameter L_{trail} in a) and leading diameter L_{lead} in b).

An additional example of this phenomenon can be seen in figure 6.10.

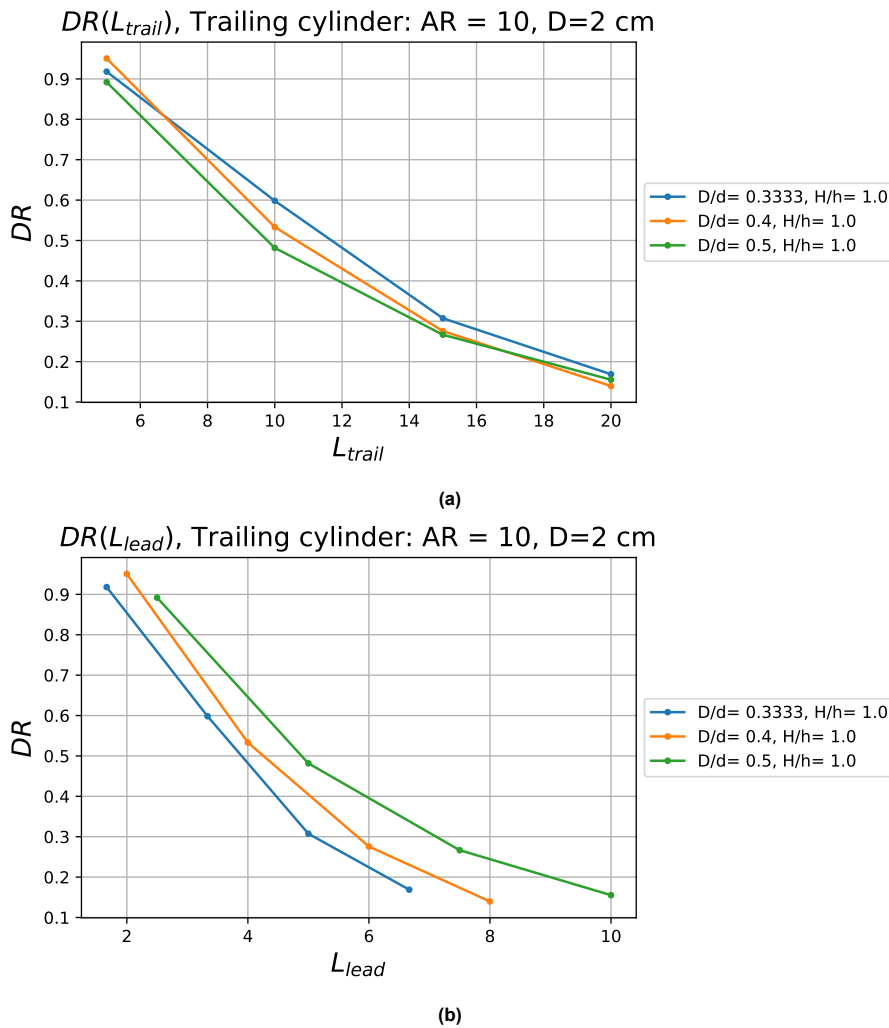


Figure 6.10: DR as a function of distance for the case where there was the same trailing cylinder and the distance between them being nondimensionalized by the trailing diameter L_{trail} in a) and leading diameter L_{lead} in b).

6.2.3. PIV measurements

Due to the issues mentioned earlier, only a selection of PIV data points could be extracted, and only one plot with a fixed leading cylinder could be produced. It can be seen in figure 6.11. Here, the momentum term contribution was used to determine the DR of a trailing cylinder. The plot is the same as in figure 6.11 with PIV data points overlaid.

It is hard to make conclusions based on such a limited data set. However, according to this plot and some additional results, it can be seen that while the absolute values differ noticeably between balance and PIV measurements, they both showed the same trend.

This is encouraging since it means that PIV measurements can be used to conduct relative comparisons even in situations where conditions for such measurements are not ideal.

Dynamic pressure distribution in the wake behind these three cylinder combinations can be seen in figure 6.12.

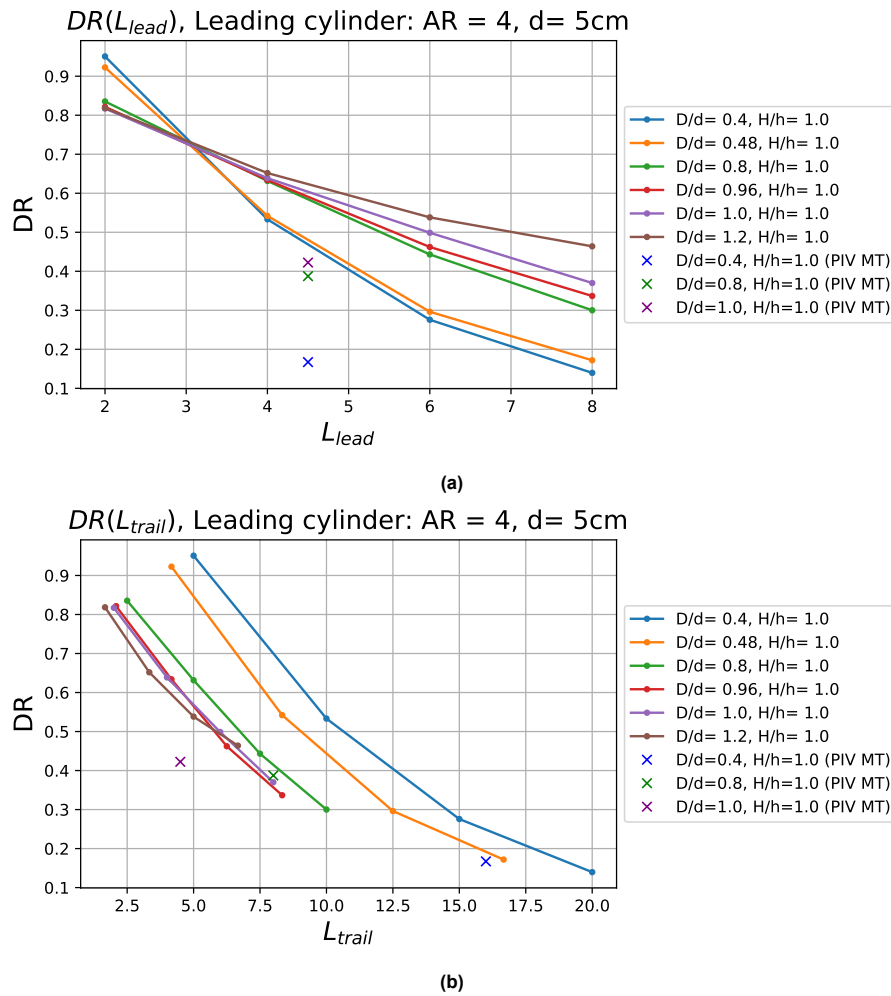


Figure 6.11: DR as a function of distance for the case where there was the same leading cylinder and the distance between them being nondimensionalized by the leading diameter L_{lead} in a) and trailing diameter L_{trail} in b). With balance data overlaid with PIV measurements.

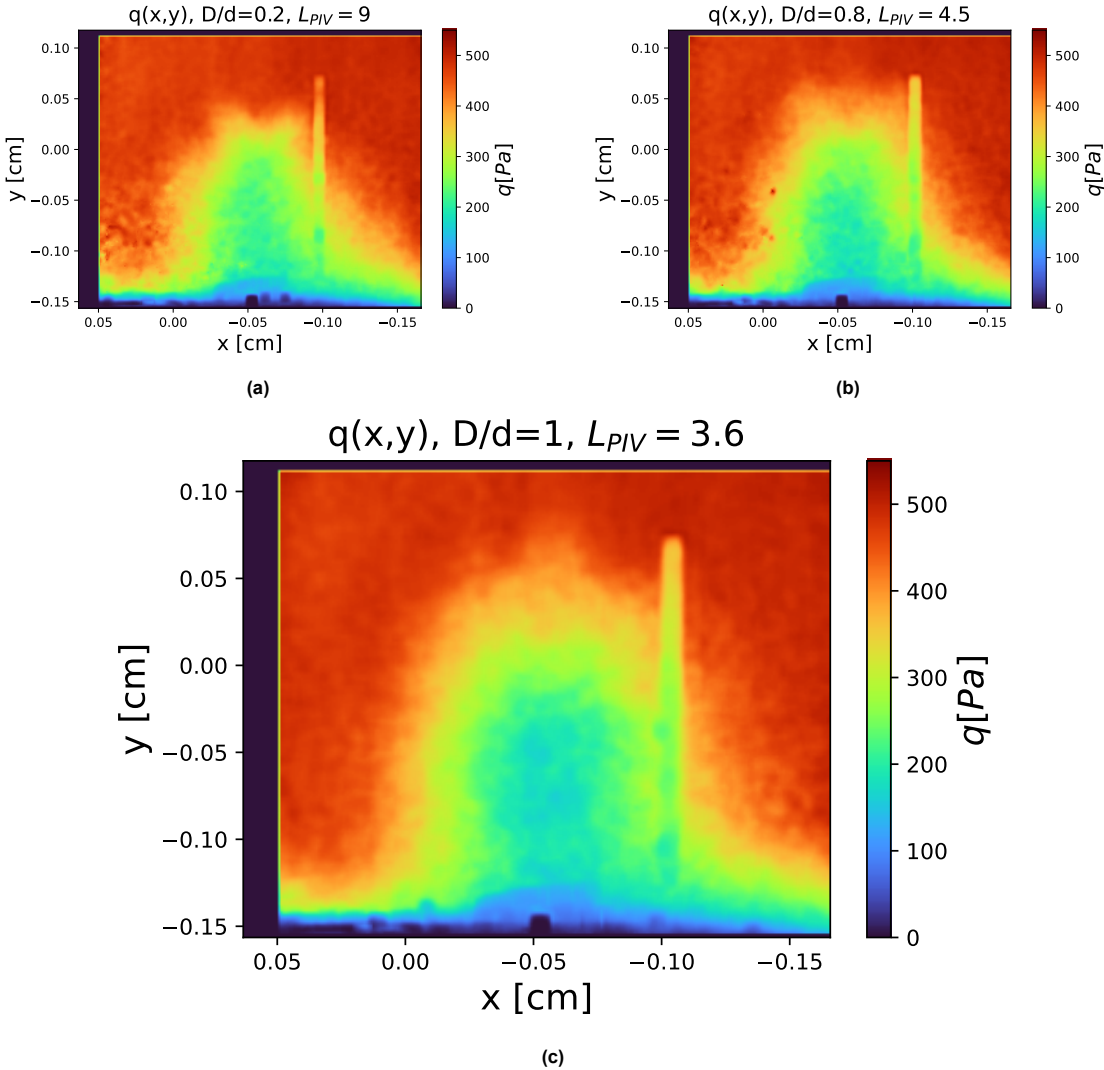


Figure 6.12: Images of the wake behind cylinders in tandem. In all cases, the leading cylinder was $AR = 4, d = 5$ cm. All images were taken at the same distance of 18 cm behind the trailing cylinder center.

7

Conclusion

This thesis aimed to characterize the aerodynamics of two finite cylinders in tandem, focusing on the drag reduction of the trailing cylinder by varying spacing, aspect ratio, and diameter ratio. This was done through an experimental WT campaign, where two different measurement techniques, balance measurements and PIV, were employed to measure the drag of drafting cylinders. A cylinder was rigidly attached to a two-component load balance, positioned under the test tunnel section. For the latter measurement technique, a stereo-PIV setup was used in combination with a control volume approach to determine the C_D of a trailing cylinder.

The balance's repeatability was good with a standard deviation of measurements of around 4%. Compared with similar experiments from the literature, the obtained C_D values were on the upper side. For PIV, individual contributions to C_D were calculated separately and added together. The values were under-predicted for the momentum and Re stress term but in line with expectations. For the pressure term, the uncertainty was significantly larger even at further distances from the trailing cylinder, where the underlining assumptions of the equation used to calculate the pressure field should be satisfied. Measurement uncertainty aside, laser reflections from cylinder models and the WT section were a large unforeseen issue, resulting in numerous measurements having to be disregarded.

In the case of an isolated cylinder, where the only expected governing parameter is the aspect ratio AR , results from balance measurements aligned well with the results from the literature, i.e., as the AR of a cylinder increases C_D increases, converging to the drag coefficient of an infinite cylinder. Apart from this, it was observed that the diameter of a cylinder had a noticeable effect. When two cylinders had the same AR but different diameters, a cylinder with a larger diameter would experience a larger C_D . This was not expected, and Re was investigated as a potential cause, but it did not explain the observation. This means that this was due to some other effect that did not scale with different cylinders that were being tested. One such effect that would explain this trend is blockage since it would be expected that measured C_D values are larger with physically larger cylinders in a closed test section due to increased induced axial velocity and, therefore, increased negative pressure gradient as a result of blockage. The same dependency of C_D on AR was also observed with PIV measurements, where the trend was even more pronounced and more in line with the literature than in the case of balance measurements. It has to be kept in mind, however, that the uncertainty of this method was significantly larger with a much more limited sample size.

Continuing with cylinders in tandem with the same AR adds a new degree of freedom to the problem. This is the distance between the two cylinders, denoted as L . Looking at the balance measurements, the trends again align with the literature, which indicates noticeably smaller C_D for the trailing cylinder at small distances L . As L increases, the drag convergence to that of an isolated cylinder. Looking at the drag reduction plot for cylinders of different AR , it can be seen that at the same distance, L , the cylinder with higher AR (more *2d-like*) experiences larger drag reduction than cylinders with smaller AR . This could be explained by the shorter reattachment distance of cylinders of lower AR as shown in table 2.1. This can be interpreted as saying that at the same distance, L , the wake of cylinders with

lower AR will sit lower and be spread more outboard, leaving the trailing cylinder exposed to more free-stream air with higher momentum. This can be seen qualitatively from PIV images of the wake in figure 6.4. It can be clearly seen that with cylinders of higher AR , the momentum deficit generated by the leading cylinders, which is part of the driving force behind drag reduction, seats higher and centered around the center line, where it will interact more with the trailing cylinder than in the case of a cylinder with a smaller AR where the momentum deficit is spread more.

Allowing AR to be different between the cylinders adds a new degree of freedom, the ratio of the two cylinder's diameter D/d . Firstly, keeping the leading cylinder constant and varying the diameter of the trailing cylinder, it was found that at a close absolute distance behind the leading cylinder, the trailing cylinder with the smallest diameter experienced the largest drag reduction. However, this reversed after a certain distance further downstream, and a cylinder with the largest diameter experienced the largest drag reduction. This would indicate that cylinders with larger diameters experience a lower starting DR due to their proportions to the leading cylinder but would lose their DR as a function of distance more slowly and, therefore, be less sensitive to changes in distance. When the AR of the leading cylinder was increased, and the experiment was repeated, the distance at which this transition happened moved downstream. This was collaborated later in the case where a trailing cylinder was kept fixed but the leading cylinder changed. At the same absolute distance from the trailing cylinder, a leading cylinder with a larger diameter will increase the drag reduction of the trailing cylinder and keep it higher for longer. However, if we measure the relative distance in terms of the leading cylinder, those with a smaller diameter will have a larger DR .

The sample size of the usable stereo-PIV measurements drastically decreased after post-processing, resulting in low reliability of its results. However, those usable measurements confirmed the trends observed with the balance measurements. This indicates that this method could also be used quantitatively to study cylinders in tandem, within the method's limitations and assumptions of the control volume approach.

7.1. Improvements and Further Research Recommendations

While reliable conclusions were able to be made, mostly due to focusing on a relative comparison of the results, multiple things could be improved to reduce the uncertainty of the results and remove some of the limitations.

On the side of the experimental setup, an open test section would be preferred to the closed test section that was used. This would reduce the influence of blockage, which was thought to be mostly negligible at the maximum blockage ratio of 8%. However, the results of isolated cylinders indicate that this might not be the case. This would also be beneficial for PIV measurements since it could be assumed that the pressure would be equal to that of the freestream at a suitable distance away from the cylinder. This would mean that the CVA assumptions for only using the upstream and downstream PIV planes would hold better, resulting in less uncertain pressure term. The momentum term would also be more reliable since it would be decoupled from the blockage and its effect on pressure and velocity within the closed test section.

The experiment would also benefit from more emphasis on ensuring that the floor BL was small. A long test section will always encourage BL growth; therefore, if the experiment were to be repeated in an open test section, a plate should be used where the ground begins shortly before the leading cylinder.

on the side of the stereo-PIV, the biggest improvements would be if the reflections were to be reduced. The open test section would solve some of the issues regarding reflections from the sides of the WT section. Cylinders could be painted in a color that would reflect less light. The positions of the two cameras could be adjusted to mitigate cylinder reflections.

It would also help if the cylinders were smaller to fit better within the measurement domain.

Looking at potential future research projects. On the side of cylinder tandem aerodynamics, the most surprising observation was that smaller diameter cylinders experienced a larger DR than larger diameter ones at a close distance behind the leading cylinder and that this trend reverses further downstream.

A more detailed study of this observation would provide more insight into mechanisms behind DR of trailing cylinders and potentially other bluff bodies as well.

The other direction is to pursue further drafting aerodynamics with PIV in a quantitative manner. This study showed that this is possible, but due to multiple factors, the results obtained here can only be used as rough proof of concept.

The most favorable setup would be to use tomographic PIV and survey the whole influential domain at the same time. This would be most beneficial for the calculation of the pressure term since it would be possible to determine streamwise velocity gradients and, therefore, fully resolve the pressure field. Something similar has been done in the past around isolated bodies, like in this study (Terra, Sciacchitano, and Scarano 2017), but, to the best of our understanding, it has yet to be done on trailing bodies. This would also enable the evaluation of optimal stereo-PIV scenarios by isolating individual planes and assessing the impacts of the underlying assumptions.

7.2. Application in Cycling

As was stated in the introduction, motivation for this work comes from cycling aerodynamics. While the experimental part did not focus on it, some recommendations for future cycling experiments can be made based on the findings. The most interesting observation was that different cylinder diameter ratios experienced different DR sensitivities. A small cylinder experienced a large drag reduction initially, but further downstream, the drag reduction fell more quickly and was smaller than a larger cylinder. If the same can be shown for cyclists, that would be useful as it would indicate that at close distances, a certain cycling tandem configuration is optimal. However, a different tandem configuration could be optimal if that close distance can not be maintained and the trailing cyclist is positioned predominately further downstream.

While both cases fall under bluff bodies, the flow structures in the wake are very different, and caution needs to be practiced when extrapolating results from one to the other. One potential next step in bridging the gap is to repeat the experiment with models of cyclists. But instead of scaling and moving them anatomically correctly, they should be scaled and scratched globally to mimic aspect ratio and diameter ratios with cylinders. If the same trend is observed, more complexity can be added to match the real world more closely.

The second aspect of the work that can be applied to studying cycling is the usage of stereo-PIV. It was shown that it could be used as a tool to study the aerodynamics of drafting quantitatively and qualitatively. It gives a more detailed insight into the problem. A systematic and extensive experimental campaign could potentially allow the identification of certain flow features and regions that are most influential for drag reduction. A potential approach to this study would be to start with a fixed trailing cyclist and vary the geometric features of the leading cyclist while taking images of the wake at multiple distances downstream. Then, the same control volume calculations and quantitative studies could be performed.

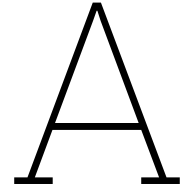
References

- Alam, Md.Mahbub et al. (2003). "Fluctuating fluid forces acting on two circular cylinders in a tandem arrangement at a subcritical Reynolds number". In: *Journal of Wind Engineering and Industrial Aerodynamics* 91.1. Fifth Asia-Pacific Conference on Wind Engineering, pp. 139–154. ISSN: 0167-6105. DOI: [https://doi.org/10.1016/S0167-6105\(02\)00341-0](https://doi.org/10.1016/S0167-6105(02)00341-0). URL: <https://www.sciencedirect.com/science/article/pii/S0167610502003410>.
- Anderson, John D. (2017). *Fundamentals of aerodynamics*. Sixth edition. McGraw-Hill series in aeronautical and aerospace engineering. New York, NY: McGraw Hill Education. 1130 pp. ISBN: 978-1-259-12991-9.
- Anthoine, Jerome, Domenico Olivari, and D. Portugaels (Nov. 2009). "Wind-tunnel blockage effect on drag coefficient of circular cylinders". In: *Wind and Structures* 12. DOI: 10.12989/was.2009.12.6.541.
- Atkins, M.D. (2016). "Chapter 5 - Velocity Field Measurement Using Particle Image Velocimetry (PIV)". In: *Application of Thermo-Fluidic Measurement Techniques*. Ed. by Tongbeum Kim, Tian Jian Lu, and Seung Jin Song. Butterworth-Heinemann, pp. 125–166. ISBN: 978-0-12-809731-1. DOI: <https://doi.org/10.1016/B978-0-12-809731-1.00005-8>. URL: <https://www.sciencedirect.com/science/article/pii/B9780128097311000058>.
- Baker, C.J. (1980). "The turbulent horseshoe vortex". In: *Journal of Wind Engineering and Industrial Aerodynamics* 6.1, pp. 9–23. ISSN: 0167-6105. DOI: [https://doi.org/10.1016/0167-6105\(80\)90018-5](https://doi.org/10.1016/0167-6105(80)90018-5). URL: <https://www.sciencedirect.com/science/article/pii/0167610580900185>.
- Bardet, PM, MA André, and DR Neal (2013). "Systematic timing errors in laser-based transit-time velocimetry". In: .
- Biermann, D. and W. H. Herrnstein (1933). "The Interference Between Struts in Various Combinations". In: NACA-TR-468. URL: <https://ntrs.nasa.gov/citations/19930091542>.
- Charonko, John J et al. (2010). "Assessment of pressure field calculations from particle image velocimetry measurements". In: *Measurement Science and technology* 21.10, p. 105401.
- De Kat, R and BW Van Oudheusden (2012). "Instantaneous planar pressure determination from PIV in turbulent flow". In: *Experiments in fluids* 52, pp. 1089–1106.
- F.R.S., Lord Rayleigh O.M. (1915). "XLVIII. Æolian tones". In: *The London, Edinburgh, and Dublin Philosophical Magazine and Journal of Science* 29.172, pp. 433–444. DOI: 10.1080/14786440408635325. eprint: <https://doi.org/10.1080/14786440408635325>. URL: <https://doi.org/10.1080/14786440408635325>.
- Farivar, Dj. (Mar. 1981). "Turbulent uniform flow around cylinders of finite length". In: *AIAA Journal* 19.3, pp. 275–281. ISSN: 0001-1452, 1533-385X. DOI: 10.2514/3.7771. URL: <https://arc.aiaa.org/doi/10.2514/3.7771> (visited on 02/02/2023).
- Fox, T.A. and G.S. West (1993). "Fluid-Induced Loading of Cantilevered Circular Cylinders in a Low-Turbulence Uniform Flow. Part 1: Mean Loading with Aspect Ratios in the Range 4 to 30". In: *Journal of Fluids and Structures* 7.1, pp. 1–14. ISSN: 0889-9746. DOI: <https://doi.org/10.1006/jfls.1993.1001>. URL: <https://www.sciencedirect.com/science/article/pii/S0889974683710017>.
- Gerrard, JH (1966). "The mechanics of the formation region of vortices behind bluff bodies". In: *Journal of fluid mechanics* 25.2, pp. 401–413.
- Igarashi, Tamotsu (1982). "Characteristics of a Flow around Two Circular Cylinders of Different Diameters Arranged in Tandem". In: *Bulletin of JSME* 25.201, pp. 349–357. DOI: 10.1299/jsme1958.25.349.
- (1984). "Characteristics of the Flow around Two Circular Cylinders Arranged in Tandem : 2nd Report, Unique Phenomenon at Small Spacing". In: *Bulletin of JSME* 27.233, pp. 2380–2387. DOI: 10.1299/jsme1958.27.2380.
- Jakobsen, ML, TP Dewhurst, and CA Greated (1997). "Particle image velocimetry for predictions of acceleration fields and force within fluid flows". In: *Measurement Science and Technology* 8.12, p. 1502.

- Kähler, Christian J and Jürgen Kompenhans (2000). "Fundamentals of multiple plane stereo particle image velocimetry". In: *Experiments in Fluids* 29.Suppl 1, S070–S077.
- Kawamura, Takao et al. (1984). "Flow around a Finite Circular Cylinder on a Flat Plate : Cylinder height greater than turbulent boundary layer thickness". In: *Bulletin of JSME* 27.232, pp. 2142–2151. DOI: 10.1299/jsme1958.27.2142.
- Kovaszny, LSG (1949). "Hot-wire investigation of the wake behind cylinders at low Reynolds numbers". In: *Proceedings of the Royal Society of London. Series A. Mathematical and Physical Sciences* 198.1053, pp. 174–190.
- LaVision (n.d.). *Calibration Plates*. <https://www.smart-piv.com/en/products/strainmaster/system-components/calibration-plates/>. Accessed: 10-04-2023.
- 3D-Flow Structures Behind Truncated Circular Cylinders* (July 2003). Vol. Volume 2: Symposia, Parts A, B, and C. Fluids Engineering Division Summer Meeting, pp. 825–831. DOI: 10.1115/FEDSM2003-45083. eprint: https://asmedigitalcollection.asme.org/FEDSM/proceedings-pdf/FEDSM2003/36975/825/2592955/825_1.pdf. URL: <https://doi.org/10.1115/FEDSM2003-45083>.
- Lienhard, John H et al. (1966). *Synopsis of lift, drag, and vortex frequency data for rigid circular cylinders*. Vol. 300. Technical Extension Service, Washington State University Pullman, WA.
- Lin, J.-C., Y. Yang, and D. Rockwell (2002). "Flow past two cylinders in tandem: instantaneous and averaged flow structure". In: *Journal of Fluids and Structures* 16.8, pp. 1059–1071. ISSN: 0889-9746. DOI: <https://doi.org/10.1006/jfls.2002.0469>. URL: <https://www.sciencedirect.com/science/article/pii/S088997460290469X>.
- Ljungkröna, L., Ch. Norberg, and B. Sundén (1991). "Free-stream turbulence and tube spacing effects on surface pressure fluctuations for two tubes in an in-line arrangement". In: *Journal of Fluids and Structures* 5.6, pp. 701–727. ISSN: 0889-9746. DOI: [https://doi.org/10.1016/0889-9746\(91\)90364-U](https://doi.org/10.1016/0889-9746(91)90364-U). URL: <https://www.sciencedirect.com/science/article/pii/088997469190364U>.
- Ljungkröna, Lars and Bengt Sundén (1993). "Flow visualization and surface pressure measurement on two tubes in an inline arrangement". In: *Experimental Thermal and Fluid Science* 6.1, pp. 15–27. ISSN: 0894-1777. DOI: [https://doi.org/10.1016/0894-1777\(93\)90037-J](https://doi.org/10.1016/0894-1777(93)90037-J). URL: <https://www.sciencedirect.com/science/article/pii/089417779390037J>.
- Mahbub Alam, Md. and Y. Zhou (2008). "Strouhal numbers, forces and flow structures around two tandem cylinders of different diameters". In: *Journal of Fluids and Structures* 24.4, pp. 505–526. ISSN: 0889-9746. DOI: <https://doi.org/10.1016/j.jfluidstructs.2007.10.001>. URL: <https://www.sciencedirect.com/science/article/pii/S0889974607000850>.
- Maskell, EC (1963). *A theory of the blockage effects on bluff bodies and stalled wings in a closed wind tunnel*. Tech. rep. Aeronautical Research Council London (United Kingdom).
- Matejicka, Lubomir and Christos Georgakis (Sept. 2021). "Wind tunnel blockage corrections of rectangular and circular cylinders". In.
- Meneghini, J.R. et al. (2001). "Numerical simulation of flow interference between two circular cylinders in tandem and side-by-side arrangements". In: *Journal of Fluids and Structures* 15.2, pp. 327–350. ISSN: 0889-9746. DOI: <https://doi.org/10.1006/jfls.2000.0343>. URL: <https://www.sciencedirect.com/science/article/pii/S0889974600903438>.
- Mittal, Sanjay, Vinod Kumar, and A. Raghuvanshi (1997). "Unsteady incompressible flows past two cylinders in tandem and staggered arrangements". In: *International Journal for Numerical Methods in Fluids* 25, pp. 1315–1344.
- Murai, Yuichi et al. (2007). "Particle tracking velocimetry applied to estimate the pressure field around a Savonius turbine". In: *Measurement science and technology* 18.8, p. 2491.
- Okamoto, Shiki and Yukisada Sunabashiri (Dec. 1992). "Vortex Shedding From a Circular Cylinder of Finite Length Placed on a Ground Plane". In: *Journal of Fluids Engineering* 114.4, pp. 512–521. ISSN: 0098-2202. DOI: 10.1115/1.2910062. eprint: https://asmedigitalcollection.asme.org/fluidsengineering/article-pdf/114/4/512/5711648/512_1.pdf. URL: <https://doi.org/10.1115/1.2910062>.
- Oudheusden, B W van (Jan. 2013). "PIV-based pressure measurement". In: *Measurement Science and Technology* 24.3, p. 032001. DOI: 10.1088/0957-0233/24/3/032001. URL: <https://dx.doi.org/10.1088/0957-0233/24/3/032001>.
- Oudheusden, Bas et al. (Aug. 2007). "Evaluation of Integral Forces and Pressure Fields from Planar Velocimetry Data for Incompressible and Compressible Flows". In: *Experiments in Fluids - EXP FLUID* 43, pp. 1–12. DOI: 10.1007/s00348-007-0261-y.

- Pattenden, R. J., S. R. Turnock, and X. Zhang (July 1, 2005). "Measurements of the flow over a low-aspect-ratio cylinder mounted on a ground plane". In: *Experiments in Fluids* 39.1, pp. 10–21. ISSN: 1432-1114. DOI: 10.1007/s00348-005-0949-9. URL: <https://doi.org/10.1007/s00348-005-0949-9>.
- Polhamus, E C (Aug. 1981). *A review of some Reynolds number effects related to bodies at high angles of attack - NASA technical reports server (NTRS)*. URL: <https://ntrs.nasa.gov/citations/19840023027>.
- Pope, A. and J.J. Harper (1966). *Low-speed Wind Tunnel Testing*. Wiley. ISBN: 9780471693925. URL: <https://books.google.si/books?id=7HhTAAAAAAAJ>.
- Raffel, Markus et al. (2018). *Particle Image Velocimetry: A Practical Guide*. Cham: Springer International Publishing. ISBN: 978-3-319-68851-0 978-3-319-68852-7. DOI: 10.1007/978-3-319-68852-7. URL: <https://link.springer.com/10.1007/978-3-319-68852-7> (visited on 02/27/2023).
- Rodríguez, I. et al. (2015). "On the flow past a circular cylinder from critical to super-critical Reynolds numbers: Wake topology and vortex shedding". In: *International Journal of Heat and Fluid Flow* 55. Special Issue devoted to the 10th Int. Symposium on Engineering Turbulence Modelling and Measurements (ETMM10) held in Marbella, Spain on September 17-19, 2014, pp. 91–103. ISSN: 0142-727X. DOI: <https://doi.org/10.1016/j.ijheatfluidflow.2015.05.009>. URL: <https://www.sciencedirect.com/science/article/pii/S0142727X15000557>.
- Samimy, M. and S. K. Lele (Aug. 1991). "Motion of particles with inertia in a compressible free shear layer". In: *Physics of Fluids A: Fluid Dynamics* 3.8, pp. 1915–1923. ISSN: 0899-8213. DOI: 10.1063/1.857921. eprint: https://pubs.aip.org/aip/pof/article-pdf/3/8/1915/12387330/1915_1_online.pdf. URL: <https://doi.org/10.1063/1.857921>.
- Sarode, R.S., S.L. Gai, and C.K. Ramesh (1981). "Flow around circular- and square-section models of finite height in a turbulent shear flow". In: *Journal of Wind Engineering and Industrial Aerodynamics* 8.3, pp. 223–230. ISSN: 0167-6105. DOI: [https://doi.org/10.1016/0167-6105\(81\)90022-2](https://doi.org/10.1016/0167-6105(81)90022-2). URL: <https://www.sciencedirect.com/science/article/pii/0167610581900222>.
- Scarano, Fulvio et al. (2015). "On the use of helium-filled soap bubbles for large-scale tomographic PIV in wind tunnel experiments". In: *Experiments in Fluids* 56, pp. 1–12.
- Sciacchitano, Andrea (2019). "Uncertainty quantification in particle image velocimetry". In: *Measurement Science and Technology* 30.9, p. 092001.
- Sciacchitano, Andrea and Fulvio Scarano (2022). *Particle Image Velocimetry (PIV) [Lecture Notes], AE4180 Flow Measurement Techniques*.
- Sinnige, T. and G. Eitelberg (2021). *Wind-Tunnel Boundary Corrections*.
- Spaelstra, Alexander et al. (2021). "On-site drag analysis of drafting cyclists". In: *Journal of Wind Engineering and Industrial Aerodynamics* 219, p. 104797.
- Spaelstra et al. (2021). "Uncertainty assessment of the Ring of Fire concept for on-site aerodynamic drag evaluation". In: *Measurement Science and Technology* 32.4, p. 044004.
- Sumner, D. (2010). "Two circular cylinders in cross-flow: A review". In: *Journal of Fluids and Structures* 26.6, pp. 849–899. ISSN: 0889-9746. DOI: <https://doi.org/10.1016/j.jfluidstructs.2010.07.001>. URL: <https://www.sciencedirect.com/science/article/pii/S0889974610000861>.
- Sumner, D., J. L. Heseltine, and O. J. P. Dansereau (Nov. 1, 2004). "Wake structure of a finite circular cylinder of small aspect ratio". In: *Experiments in Fluids* 37.5, pp. 720–730. ISSN: 1432-1114. DOI: 10.1007/s00348-004-0862-7. URL: <https://doi.org/10.1007/s00348-004-0862-7>.
- Terra, W, A Sciacchitano, and F Scarano (2017). "Aerodynamic drag of a transiting sphere by large-scale tomographic-PIV". In: *Experiments in Fluids* 58, pp. 1–14.
- TU Delft (n.d.). *W-Tunnel*. <https://www.tudelft.nl/lr/organisatie/afdelingen/flow-physics-and-technology/facilities/low-speed-wind-tunnels/w-tunnel>. [Online; accessed 21-June-2023].
- Vincenti, Walter G (1944). *Wall interference in a two-dimensional-flow wind tunnel with consideration of the effect of compressibility*. Tech. rep.
- Violato, Daniele, Peter Moore, and Fulvio Scarano (Apr. 1, 2011). "Lagrangian and Eulerian pressure field evaluation of rod-airfoil flow from time-resolved tomographic PIV". In: *Experiments in Fluids* 50.4, pp. 1057–1070. ISSN: 1432-1114. DOI: 10.1007/s00348-010-1011-0. URL: <https://doi.org/10.1007/s00348-010-1011-0>.

- Wang, Longjun, Md. Mahbub Alam, and Yu Zhou (2018). "Two tandem cylinders of different diameters in cross-flow: effect of an upstream cylinder on wake dynamics". In: *Journal of Fluid Mechanics* 836, pp. 5–42. DOI: 10.1017/jfm.2017.735.
- Wang, Shunsen, Jingru Mao, and Liu Guanwei (June 2007). "Uncertainty of the PIV Testing Results for Gas Flow Field Caused by Tracer Particles and Seeding Method". In: *AIP Conference Proceedings* 914. DOI: 10.1063/1.2747424.
- Westerweel, J (Dec. 1997). "Fundamentals of digital particle image velocimetry". In: *Measurement Science and Technology* 8.12, p. 1379. DOI: 10.1088/0957-0233/8/12/002. URL: <https://dx.doi.org/10.1088/0957-0233/8/12/002>.
- Zdravkovich, M. M. (1997). *Flow Around Circular Cylinders Volume 1: Fundamentals*. United Kingdom: Oxford University Press. 694 pp. ISBN: 0198563965.
- (1987). "The effects of interference between circular cylinders in cross flow††An earlier version as originally presented as an invited paper, entitled "Forces on pipe clusters", at the International Symposium on Separated Flow around Marine Structures, Norwegian Institute of Technology, Trondheim, Norway, 26–28 June 1985." In: *Journal of Fluids and Structures* 1.2, pp. 239–261. ISSN: 0889-9746. DOI: [https://doi.org/10.1016/S0889-9746\(87\)90355-0](https://doi.org/10.1016/S0889-9746(87)90355-0). URL: <https://www.sciencedirect.com/science/article/pii/S0889974687903550>.
- Zdravkovich, M.M. and D.L. Pridden (1977). "Interference between two circular cylinders; Series of unexpected discontinuities". In: *Journal of Wind Engineering and Industrial Aerodynamics* 2.3, pp. 255–270. ISSN: 0167-6105. DOI: [https://doi.org/10.1016/0167-6105\(77\)90026-5](https://doi.org/10.1016/0167-6105(77)90026-5). URL: <https://www.sciencedirect.com/science/article/pii/0167610577900265>.
- Zhou, Y. and M. W. Yiu (2006). "Flow structure, momentum and heat transport in a two-tandem-cylinder wake". In: *Journal of Fluid Mechanics* 548, pp. 17–48. DOI: 10.1017/S002211200500738X.



Test Matrix

The test matrix used for the experiment.

d and h relate to the leading cylinder and D and H to the trailing cylinder.

$dist$ represents the distance between the trailing and leading cylinder, and PIV indicates if the PIV measurement was taken alongside the balance measurement, which was taken for all runs.

day	run	d [mm]	h [mm]	D [mm]	H [mm]	$dist$ [mm]	PIV
Friday 0309	1	0	0	120	100	0	PIV
Friday 0309	2	100	100	120	100	200	PIV
Friday 0309	3	100	100	120	100	300	PIV
Friday 0309	4	100	100	120	100	400	PIV
Friday 0309	5	0	0	60	60	0	PIV
Friday 0309	6	100	100	60	60	200	PIV
Friday 0309	7	100	100	60	60	300	PIV
Friday 0309	8	100	100	60	60	400	PIV
Friday 0309	9	0	0	80	100	0	PIV
Friday 0309	10	100	100	80	100	200	PIV
Friday 0309	11	100	100	80	100	300	PIV
Friday 0309	12	100	100	80	100	400	PIV
Friday 0309	13	0	0	40	60	0	PIV
Friday 0309	14	100	100	40	60	200	PIV
Friday 0309	15	100	100	40	60	300	PIV
Friday 0309	16	100	100	40	60	400	PIV
Friday 0309	17	0	0	40	100	0	PIV
Friday 0309	18	100	100	40	100	200	PIV
Friday 0309	19	100	100	40	100	300	PIV
Friday 0309	20	100	100	40	100	400	PIV
Friday 0309	21	0	0	80	60	0	PIV
Friday 0309	22	100	100	80	60	200	PIV
Friday 0309	23	100	100	80	60	300	PIV
Friday 0309	24	100	100	80	60	400	PIV
Friday 0309	25	0	0	120	60	0	PIV
Friday 0309	26	100	100	120	60	200	PIV
Friday 0309	27	100	100	120	60	300	PIV
Friday 0309	28	100	100	120	60	400	PIV
Friday 0309	29	0	0	40	240	0	PIV
Friday 0309	30	0	0	32	240	0	PIV
Friday 0309	31	40	240	32	240	80	PIV
Friday 0309	32	40	240	32	240	120	PIV
Friday 0309	33	40	240	32	240	160	PIV
Friday 0309	34	40	240	32	240	240	PIV

day	run	d [mm]	h [mm]	D [mm]	H [mm]	dist [mm]	PIV
Friday 0309	35	40	240	32	240	400	PIV
Friday 0309	36	0	0	24	240	0	PIV
Friday 0309	37	40	240	24	240	80	PIV
Friday 0309	38	40	240	24	240	120	PIV
Friday 0309	39	40	240	24	240	160	PIV
Friday 0309	40	40	240	24	240	240	PIV
Friday 0309	41	40	240	24	240	400	PIV
Friday 0309	42	0	0	24	144	0	PIV
Friday 0309	43	40	240	24	144	80	PIV
Friday 0309	44	40	240	24	144	120	PIV
Friday 0309	45	40	240	24	144	160	PIV
Friday 0309	45	40	240	24	144	240	PIV
Friday 0309	46	40	240	24	144	400	PIV
Friday 0309	47	0	0	32	144	0	PIV
Friday 0309	48	40	240	32	144	80	PIV
Friday 0309	49	40	240	32	144	120	PIV
Friday 0309	50	40	240	32	144	160	PIV
Friday 0309	51	40	240	32	144	240	PIV
Friday 0309	52	40	240	32	144	400	PIV
Friday 0309	53	0	0	40	144	0	PIV
Friday 0309	54	40	240	40	144	80	PIV
Friday 0309	55	40	240	40	144	120	PIV
Friday 0309	56	40	240	40	144	160	PIV
Friday 0309	57	40	240	40	144	240	PIV
Friday 0309	58	40	240	40	144	400	PIV
Friday 0309	59	0	0	0	0	0	PIV
Tuesday 0706	60	0	0	48	144	0	PIV
Tuesday 0706	61	40	240	48	144	80	PIV
Tuesday 0706	62	40	240	48	144	120	PIV
Tuesday 0706	63	40	240	48	144	160	PIV
Tuesday 0706	64	40	240	48	144	240	PIV
Tuesday 0706	65	40	240	48	144	400	PIV
Tuesday 0706	66	0	0	40	240	0	PIV
Tuesday 0706	67	40	240	40	240	80	PIV
Tuesday 0706	68	40	240	40	240	120	PIV
Tuesday 0706	69	40	240	40	240	160	PIV
Tuesday 0706	70	40	240	40	240	240	PIV
Tuesday 0706	71	40	240	40	240	400	PIV
Tuesday 0706	72	0	0	40	240	0	PIV
Tuesday 0706	73	0	0	100	100	200	PIV
Tuesday 0706	74	100	100	100	100	200	PIV
Tuesday 0706	75	100	100	100	100	300	PIV
Tuesday 0706	76	100	100	100	100	400	PIV
Tuesday 0706	77	0	0	100	100	0	PIV
Tuesday 0706	78	0	0	50	200	0	PIV
Tuesday 0706	79	0	0	50	120	0	PIV
Tuesday 0706	80	50	200	50	120	100	PIV
Tuesday 0706	81	50	200	50	120	200	PIV
Tuesday 0706	82	50	200	50	120	400	PIV
Tuesday 0706	83	0	0	0	0	0	
Tuesday 0706	84	0	0	0	0	0	
Tuesday 0706	85	0	0	0	0	0	
Tuesday 0706	86	0	0	0	0	0	
Tuesday 0706	87	0	0	0	0	0	
Tuesday 0706	88	0	0	0	0	0	

day	run	d [mm]	h [mm]	D [mm]	H [mm]	dist [mm]	PIV
Tuesday 0706	89	0	0	0	0	0	
Tuesday 0706	90	0	0	0	0	0	
Wednesday 0806	91	100	100	0	0	0	PIV
Wednesday 0806	92	100	100	0	0	100	PIV
Wednesday 0806	93	100	100	0	0	200	PIV
Wednesday 0806	94	100	100	0	0	300	PIV
Wednesday 0806	95	100	100	0	0	400	PIV
Wednesday 0806	96	40	240	0	0	0	PIV
Wednesday 0806	97	40	240	0	0	80	PIV
Wednesday 0806	98	40	240	0	0	120	PIV
Wednesday 0806	99	40	240	0	0	160	PIV
Wednesday 0806	100	40	240	0	0	200	PIV
Wednesday 0806	101	40	240	0	0	240	PIV
Wednesday 0806	102	40	240	0	0	280	PIV
Wednesday 0806	103	40	240	0	0	320	PIV
Wednesday 0806	104	40	240	0	0	360	PIV
Wednesday 0806	105	40	240	0	0	400	PIV
Wednesday 0806	106	50	200	0	0	0	PIV
Wednesday 0806	107	50	200	0	0	100	PIV
Wednesday 0806	108	50	200	0	0	200	PIV
Wednesday 0806	109	50	200	0	0	300	PIV
Wednesday 0806	110	50	200	0	0	400	PIV
Wednesday 0806	111	0	0	120	100	0	PIV
Wednesday 0806	112	0	0	120	100	300	PIV
Wednesday 0806	113	0	0	40	100	0	PIV
Wednesday 0806	114	0	0	40	100	300	PIV
Wednesday 0806	115	0	0	40	144	0	
Wednesday 0806	116	0	0	40	144	80	
Wednesday 0806	117	0	0	32	144	0	
Wednesday 0806	118	0	0	32	144	80	
Wednesday 0806	119	0	0	32	240	0	
Wednesday 0806	120	0	0	32	240	80	
Wednesday 0806	121	0	0	40	144	0	
Wednesday 0806	122	0	0	40	144	80	
Wednesday 0806	123	0	0	40	144	0	
Wednesday 0806	124	0	0	40	144	80	
Wednesday 0806	125	0	0	50	120	0	
Wednesday 0806	126	50	200	50	120	100	
Wednesday 0806	127	50	200	50	120	200	
Wednesday 0806	128	50	200	50	120	400	
Wednesday 0806	129	0	0	40	120	0	
Wednesday 0806	130	50	200	40	120	100	
Wednesday 0806	131	50	200	40	120	200	
Wednesday 0806	132	50	200	40	120	400	
Thursday 0906	133	0	0	50	200	0	
Thursday 0906	134	50	200	50	200	100	
Thursday 0906	135	50	200	50	200	200	
Thursday 0906	136	50	200	50	200	400	
Thursday 0906	137	0	0	40	200	0	
Thursday 0906	138	50	200	40	200	100	
Thursday 0906	139	50	200	40	200	200	
Thursday 0906	140	50	200	40	200	400	
Thursday 0906	141	0	0	60	200	0	
Thursday 0906	142	50	200	60	200	100	
Thursday 0906	143	50	200	60	200	200	

day	run	d [mm]	h [mm]	D [mm]	H [mm]	dist [mm]	PIV
Thursday 0906	144	50	200	60	200	400	
Thursday 0906	145	0	0	60	120	0	
Thursday 0906	146	50	200	60	120	100	
Thursday 0906	147	50	200	60	120	200	
Thursday 0906	148	50	200	60	120	400	
Thursday 0906	149	0	0	20	200	0	
Thursday 0906	150	50	200	20	200	100	
Thursday 0906	151	50	200	20	200	200	
Thursday 0906	152	50	200	20	200	400	
Thursday 0906	153	0	0	20	120	0	
Thursday 0906	154	50	200	20	120	100	
Thursday 0906	155	50	200	20	120	200	
Thursday 0906	156	50	200	20	120	400	
Thursday 0906	157	0	0	50	200	0	PIV
Thursday 0906	158	0	0	50	200	100	PIV
Thursday 0906	159	0	0	50	200	400	PIV
Thursday 0906	160	0	0	40	200	0	PIV
Thursday 0906	161	0	0	40	200	100	PIV
Thursday 0906	162	0	0	40	200	400	PIV
Thursday 0906	163	0	0	60	200	0	PIV
Thursday 0906	164	0	0	60	200	100	PIV
Thursday 0906	165	0	0	60	200	400	PIV
Thursday 0906	166	0	0	60	120	0	PIV
Thursday 0906	167	0	0	60	120	100	PIV
Thursday 0906	168	0	0	60	120	400	PIV
Thursday 0906	169	0	0	20	120	0	PIV
Thursday 0906	170	0	0	20	120	100	PIV
Thursday 0906	171	0	0	20	120	400	PIV
Thursday 0906	172	0	0	20	200	0	PIV
Thursday 0906	173	0	0	20	200	100	PIV
Thursday 0906	174	0	0	20	200	400	PIV
Thursday 0906	175	0	0	50	120	0	PIV
Thursday 0906	176	0	0	50	120	100	PIV
Thursday 0906	177	0	0	50	120	400	PIV
Thursday 0906	178	0	0	40	120	0	PIV
Thursday 0906	179	0	0	40	120	100	PIV
Thursday 0906	180	0	0	40	120	400	PIV
Thursday 0906	181	0	0	40	144	0	PIV
Thursday 0906	182	0	0	40	144	80	PIV
Thursday 0906	183	0	0	40	144	400	PIV
Thursday 0906	184	0	0	24	240	0	PIV
Thursday 0906	185	0	0	24	240	80	PIV
Thursday 0906	186	0	0	24	240	400	PIV
Thursday 0906	187	0	0	32	144	0	PIV
Thursday 0906	188	0	0	32	144	80	PIV
Thursday 0906	189	0	0	32	144	400	PIV
Thursday 0906	190	0	0	32	240	0	PIV
Thursday 0906	191	0	0	32	240	80	PIV
Thursday 0906	192	0	0	32	240	400	PIV
Thursday 0906	193	0	0	24	240	0	PIV
Thursday 0906	194	0	0	24	240	80	PIV
Thursday 0906	195	0	0	24	240	400	PIV
Thursday 0906	196	0	0	48	144	0	PIV
Thursday 0906	197	0	0	48	144	80	PIV
Thursday 0906	198	0	0	48	144	400	PIV

day	run	d [mm]	h [mm]	D [mm]	H [mm]	dist [mm]	PIV
Thursday 0906	199	0	0	48	144	0	PIV
Thursday 0906	200	0	0	48	144	80	PIV
Thursday 0906	201	0	0	48	144	400	PIV
Thursday 0906	202	50	200	50	200	300	
Thursday 0906	203	50	200	50	120	300	
Thursday 0906	204	50	200	40	200	300	
Thursday 0906	205	50	200	40	120	300	
Thursday 0906	206	50	200	20	200	300	
Thursday 0906	207	50	200	20	120	300	
Thursday 0906	208	50	200	60	200	300	
Thursday 0906	209	50	200	60	120	300	
Thursday 0906	210	500	500	500	500	5000	
Friday 1006	211	0	0	50	200	400	
Friday 1006	212	50	200	50	200	400	
Friday 1006	213	50	200	50	120	400	
Friday 1006	214	50	200	40	200	400	
Friday 1006	215	50	200	40	120	400	
Friday 1006	216	50	200	20	200	400	
Friday 1006	217	50	200	20	120	400	
Friday 1006	218	50	200	60	200	400	
Friday 1006	219	50	200	60	120	400	
Friday 1006	220	0	0	50	200	400	
Friday 1006	221	50	200	50	200	320	PIV
Friday 1006	222	50	200	50	120	320	PIV
Friday 1006	223	50	200	40	200	320	PIV
Friday 1006	224	50	200	40	120	320	PIV
Friday 1006	225	50	200	20	200	320	PIV
Friday 1006	226	50	200	20	120	320	PIV
Friday 1006	227	50	200	60	200	320	PIV
Friday 1006	228	50	200	60	120	320	PIV
Friday 1006	229	0	0	100	100	400	PIV
Friday 1006	230	100	100	100	100	0	PIV
Friday 1006	231	100	100	100	100	100	PIV
Friday 1006	232	100	100	60	60	0	PIV
Friday 1006	233	100	100	60	60	100	PIV
Friday 1006	234	0	0	40	240	400	PIV
Friday 1006	235	40	240	40	240	0	PIV
Friday 1006	236	40	240	240	240	80	PIV
Friday 1006	237	40	240	32	144	0	PIV
Friday 1006	238	40	240	32	144	80	PIV
Friday 1006	239	0	0	0	0	0	PIV
Friday 1006	240	40	240	40	240	320	
Friday 1006	241	40	240	40	144	320	
Friday 1006	242	40	240	32	240	320	
Friday 1006	243	40	240	32	144	320	
Friday 1006	244	40	240	24	240	320	
Friday 1006	245	40	240	24	144	320	
Friday 1006	246	40	240	48	240	320	
Friday 1006	247	40	240	48	144	320	
Friday 1006	248	0	0	48	240	0	
Friday 1006	249	40	240	48	240	80	
Friday 1006	250	40	240	48	240	120	
Friday 1006	251	40	240	48	240	160	
Friday 1006	252	40	240	48	240	240	
Friday 1006	253	40	240	48	240	400	

day	run	d [mm]	h [mm]	D [mm]	H [mm]	dist [mm]	PIV
Wednesday 2707	260	0	0	40	240	999	
Wednesday 2707	261	0	0	40	240	0	
Wednesday 2707	262	40	240	40	240	80	
Wednesday 2707	263	40	240	40	240	120	
Wednesday 2707	264	40	240	40	240	160	
Wednesday 2707	265	40	240	40	240	240	
Wednesday 2707	266	40	240	40	240	320	
Wednesday 2707	267	40	240	40	240	400	
Wednesday 2707	268	0	0	48	240	999	
Wednesday 2707	269	0	0	48	240	0	
Wednesday 2707	270	40	240	48	240	80	
Wednesday 2707	271	40	240	48	240	120	
Wednesday 2707	272	40	240	48	240	160	
Wednesday 2707	273	40	240	48	240	240	
Wednesday 2707	274	40	240	48	240	320	
Wednesday 2707	275	40	240	48	240	400	
Wednesday 2707	276	0	0	24	240	999	
Wednesday 2707	277	0	0	24	240	0	
Wednesday 2707	278	40	240	24	240	80	
Wednesday 2707	279	40	240	24	240	120	
Wednesday 2707	280	40	240	24	240	160	
Wednesday 2707	281	40	240	24	240	240	
Wednesday 2707	282	40	240	24	240	320	
Wednesday 2707	283	40	240	24	240	400	
Wednesday 2707	284	0	0	24	144	999	
Wednesday 2707	285	0	0	24	144	0	
Wednesday 2707	286	40	240	24	144	80	
Wednesday 2707	287	40	240	24	144	120	
Wednesday 2707	288	40	240	24	144	160	
Wednesday 2707	289	40	240	24	144	240	
Wednesday 2707	290	40	240	24	144	320	
Wednesday 2707	291	40	240	24	144	400	
Wednesday 2707	292	0	0	32	144	999	
Wednesday 2707	293	0	0	32	144	0	
Wednesday 2707	294	40	240	32	144	80	
Wednesday 2707	295	40	240	32	144	120	
Wednesday 2707	296	40	240	32	144	160	
Wednesday 2707	297	40	240	32	144	240	
Wednesday 2707	298	40	240	32	144	320	
Wednesday 2707	299	40	240	32	144	400	
Wednesday 2707	300	0	0	40	144	999	
Wednesday 2707	301	0	0	40	144	0	
Wednesday 2707	302	40	240	40	144	80	
Wednesday 2707	303	40	240	40	144	120	
Wednesday 2707	304	40	240	40	144	160	
Wednesday 2707	305	40	240	40	144	240	
Wednesday 2707	306	40	240	40	144	320	
Wednesday 2707	307	40	240	40	144	400	
Wednesday 2707	308	0	0	48	144	999	
Wednesday 2707	309	0	0	48	144	0	
Wednesday 2707	310	40	240	48	144	80	
Wednesday 2707	311	40	240	48	144	120	
Wednesday 2707	312	40	240	48	144	160	
Wednesday 2707	313	40	240	48	144	240	
Wednesday 2707	314	40	240	48	144	320	

day	run	d [mm]	h [mm]	D [mm]	H [mm]	dist [mm]	PIV
Wednesday 2707	315	40	240	48	144	400	
Thursday 2807	316	0	0	40	240	999	
Thursday 2807	317	0	0	40	240	0	
Thursday 2807	318	40	144	40	240	80	
Thursday 2807	319	40	144	40	240	120	
Thursday 2807	320	40	144	40	240	160	
Thursday 2807	321	40	144	40	240	240	
Thursday 2807	322	40	144	40	240	320	
Thursday 2807	323	40	144	40	240	400	
Thursday 2807	324	0	0	48	240	999	
Thursday 2807	325	0	0	48	240	0	
Thursday 2807	326	40	144	48	240	80	
Thursday 2807	327	40	144	48	240	120	
Thursday 2807	328	40	144	48	240	160	
Thursday 2807	329	40	144	48	240	240	
Thursday 2807	330	40	144	48	240	320	
Thursday 2807	331	40	144	48	240	400	
Thursday 2807	332	0	0	24	240	999	
Thursday 2807	333	0	0	24	240	0	
Thursday 2807	334	40	144	24	240	80	
Thursday 2807	335	40	144	24	240	120	
Thursday 2807	336	40	144	24	240	160	
Thursday 2807	337	40	144	24	240	240	
Thursday 2807	338	40	144	24	240	320	
Thursday 2807	339	40	144	24	240	400	
Thursday 2807	340	0	0	24	144	999	
Thursday 2807	341	0	0	24	144	0	
Thursday 2807	342	40	144	24	144	80	
Thursday 2807	343	40	144	24	144	120	
Thursday 2807	344	40	144	24	144	160	
Thursday 2807	345	40	144	24	144	240	
Thursday 2807	346	40	144	24	144	320	
Thursday 2807	347	40	144	24	144	400	
Thursday 2807	348	0	0	32	144	999	
Thursday 2807	349	0	0	32	144	0	
Thursday 2807	350	40	144	32	144	80	
Thursday 2807	351	40	144	32	144	120	
Thursday 2807	352	40	144	32	144	160	
Thursday 2807	353	40	144	32	144	240	
Thursday 2807	354	40	144	32	144	320	
Thursday 2807	355	40	144	32	144	400	
Thursday 2807	356	0	0	48	144	999	
Thursday 2807	357	0	0	48	144	0	
Thursday 2807	358	40	144	48	144	80	
Thursday 2807	359	40	144	48	144	120	
Thursday 2807	360	40	144	48	144	160	
Thursday 2807	361	40	144	48	144	240	
Thursday 2807	362	40	144	48	144	320	
Thursday 2807	363	40	144	48	144	400	
Thursday 2807	364	0	0	48	144	999	
Thursday 2807	365	0	0	48	144	0	
Thursday 2807	366	24	144	48	144	80	
Thursday 2807	367	24	144	48	144	160	
Thursday 2807	368	24	144	48	144	320	
Thursday 2807	369	24	144	48	144	400	

day	run	d [mm]	h [mm]	D [mm]	H [mm]	dist [mm]	PIV
Thursday 2807	370	0	0	48	240	999	
Thursday 2807	371	0	0	48	240	0	
Thursday 2807	372	24	144	48	240	80	
Thursday 2807	373	24	144	48	240	160	
Thursday 2807	374	24	144	48	240	320	
Thursday 2807	375	24	144	48	240	400	
Thursday 2807	376	0	0	24	240	999	
Thursday 2807	377	0	0	24	240	0	
Thursday 2807	378	24	144	24	240	80	
Thursday 2807	379	24	144	24	240	160	
Thursday 2807	380	24	144	24	240	320	
Thursday 2807	381	24	144	24	240	400	
Thursday 2807	382	0	0	48	144	999	
Thursday 2807	383	0	0	48	144	0	
Thursday 2807	384	24	240	48	144	80	
Thursday 2807	385	24	240	48	144	160	
Thursday 2807	386	24	240	48	144	320	
Thursday 2807	387	24	240	48	144	400	
Thursday 2807	388	0	0	48	240	999	
Thursday 2807	389	0	0	48	240	0	
Thursday 2807	390	24	240	48	240	80	
Thursday 2807	391	24	240	48	240	160	
Thursday 2807	392	24	240	48	240	320	
Thursday 2807	393	24	240	48	240	400	
Thursday 2807	394	0	0	24	144	999	
Thursday 2807	395	0	0	24	144	0	
Thursday 2807	396	24	144	24	144	80	
Thursday 2807	397	24	144	24	144	160	
Thursday 2807	398	24	144	24	144	320	
Thursday 2807	399	24	144	24	144	400	
Thursday 2807	400	0	0	48	144	999	
Thursday 2807	401	0	0	48	144	0	
Thursday 2807	402	48	240	48	144	80	
Thursday 2807	403	48	240	48	144	160	
Thursday 2807	404	48	240	48	144	320	
Thursday 2807	405	48	240	48	144	400	
Thursday 2807	406	0	0	24	240	999	
Thursday 2807	407	0	0	24	240	0	
Thursday 2807	408	48	240	24	240	80	
Thursday 2807	409	48	240	24	240	160	
Thursday 2807	410	48	240	24	240	320	
Thursday 2807	411	48	240	24	240	400	
Thursday 2807	412	0	0	24	144	999	
Thursday 2807	413	0	0	24	144	0	
Thursday 2807	414	48	240	24	144	80	
Thursday 2807	415	48	240	24	144	160	
Thursday 2807	416	48	240	24	144	320	
Thursday 2807	417	48	240	24	144	400	
Thursday 2807	418	0	0	48	240	999	
Thursday 2807	419	0	0	48	240	0	
Thursday 2807	420	48	144	48	240	80	
Thursday 2807	421	48	144	48	240	160	
Thursday 2807	422	48	144	48	240	320	
Thursday 2807	423	48	144	48	240	400	
Thursday 2807	424	0	0	24	240	999	

day	run	d [mm]	h [mm]	D [mm]	H [mm]	dist [mm]	PIV
Thursday 2807	425	0	0	24	240	0	
Thursday 2807	426	48	144	24	240	80	
Thursday 2807	427	48	144	24	240	160	
Thursday 2807	428	48	144	24	240	320	
Thursday 2807	429	48	144	24	240	400	
Thursday 2807	430	0	0	24	144	999	
Thursday 2807	431	0	0	24	144	0	
Thursday 2807	432	48	144	24	144	80	
Thursday 2807	433	48	144	24	144	160	
Thursday 2807	434	48	144	24	144	320	
Thursday 2807	435	48	144	24	144	400	
Thursday 2807	436	0	0	50	200	999	
Thursday 2807	437	0	0	50	200	0	
Thursday 2807	438	50	200	50	200	100	
Thursday 2807	439	50	200	50	200	200	
Thursday 2807	440	50	200	50	200	300	
Thursday 2807	441	50	200	50	200	400	
Thursday 2807	442	0	0	60	200	999	
Thursday 2807	443	0	0	60	200	0	
Thursday 2807	444	50	200	60	200	100	
Thursday 2807	445	50	200	60	200	200	
Thursday 2807	446	50	200	60	200	300	
Thursday 2807	447	50	200	60	200	400	
Thursday 2807	448	0	0	40	200	999	
Thursday 2807	449	0	0	40	200	0	
Thursday 2807	450	50	200	40	200	100	
Thursday 2807	451	50	200	40	200	200	
Thursday 2807	452	50	200	40	200	300	
Thursday 2807	453	50	200	40	200	400	
Friday 2907	454	0	0	20	200	999	
Friday 2907	455	0	0	20	200	0	
Friday 2907	456	50	200	20	200	100	
Friday 2907	457	50	200	20	200	200	
Friday 2907	458	50	200	20	200	300	
Friday 2907	459	50	200	20	200	400	
Friday 2907	460	0	0	24	200	999	
Friday 2907	461	0	0	24	200	0	
Friday 2907	462	50	200	24	200	100	
Friday 2907	463	50	200	24	200	200	
Friday 2907	464	50	200	24	200	300	
Friday 2907	465	50	200	24	200	400	
Friday 2907	466	0	0	48	200	999	
Friday 2907	467	0	0	48	200	0	
Friday 2907	468	50	200	48	200	100	
Friday 2907	469	50	200	48	200	200	
Friday 2907	470	50	200	48	200	300	
Friday 2907	471	50	200	48	200	400	
Friday 2907	472	0	0	60	200	999	
Friday 2907	473	0	0	60	200	0	
Friday 2907	474	40	200	60	200	100	
Friday 2907	475	40	200	60	200	200	
Friday 2907	476	40	200	60	200	300	
Friday 2907	477	40	200	60	200	400	
Friday 2907	478	0	0	50	200	999	
Friday 2907	479	0	0	50	200	0	

day	run	d [mm]	h [mm]	D [mm]	H [mm]	dist [mm]	PIV
Friday 2907	480	40	200	50	200	100	
Friday 2907	481	40	200	50	200	200	
Friday 2907	482	40	200	50	200	300	
Friday 2907	483	40	200	50	200	400	
Friday 2907	484	0	0	48	200	999	
Friday 2907	485	0	0	48	200	0	
Friday 2907	486	40	200	48	200	100	
Friday 2907	487	40	200	48	200	200	
Friday 2907	488	40	200	48	200	300	
Friday 2907	489	40	200	48	200	400	
Friday 2907	490	0	0	24	200	999	
Friday 2907	491	0	0	24	200	0	
Friday 2907	492	40	200	24	200	100	
Friday 2907	493	40	200	24	200	200	
Friday 2907	494	40	200	24	200	300	
Friday 2907	495	40	200	24	200	400	
Friday 2907	496	0	0	20	200	999	
Friday 2907	497	0	0	20	200	0	
Friday 2907	498	40	200	20	200	100	
Friday 2907	499	40	200	20	200	200	
Friday 2907	500	40	200	20	200	300	
Friday 2907	501	40	200	20	200	400	
Friday 2907	502	0	0	20	200	999	
Friday 2907	503	0	0	20	200	0	
Friday 2907	504	60	200	20	200	100	
Friday 2907	505	60	200	20	200	200	
Friday 2907	506	60	200	20	200	300	
Friday 2907	507	60	200	20	200	400	
Friday 2907	508	0	0	50	200	999	
Friday 2907	509	0	0	50	200	0	
Friday 2907	510	60	200	50	200	100	
Friday 2907	511	60	200	50	200	200	
Friday 2907	512	60	200	50	200	300	
Friday 2907	513	60	200	50	200	400	
Friday 2907	514	0	0	48	200	999	
Friday 2907	515	0	0	48	200	0	
Friday 2907	516	60	200	48	200	100	
Friday 2907	517	60	200	48	200	200	
Friday 2907	518	60	200	48	200	300	
Friday 2907	519	60	200	48	200	400	
Friday 2907	520	0	0	24	200	999	
Friday 2907	521	0	0	24	200	0	
Friday 2907	522	60	200	24	200	100	
Friday 2907	523	60	200	24	200	200	
Friday 2907	524	60	200	24	200	300	
Friday 2907	525	60	200	24	200	400	
Friday 2907	526	0	0	40	200	999	
Friday 2907	527	0	0	40	200	0	
Friday 2907	528	60	200	40	200	100	
Friday 2907	529	60	200	40	200	200	
Friday 2907	530	60	200	40	200	300	
Friday 2907	531	60	200	40	200	400	
Friday 2907	532	0	0	40	200	999	
Friday 2907	533	0	0	40	200	0	
Friday 2907	534	20	200	40	200	100	

day	run	d [mm]	h [mm]	D [mm]	H [mm]	dist [mm]	PIV
Friday 2907	535	20	200	40	200	200	
Friday 2907	536	20	200	40	200	300	
Friday 2907	537	20	200	40	200	400	
Friday 2907	538	0	0	50	200	999	
Friday 2907	539	0	0	50	200	0	
Friday 2907	540	60	200	50	200	100	
Friday 2907	541	60	200	50	200	200	
Friday 2907	542	60	200	50	200	300	
Friday 2907	543	60	200	50	200	400	
Friday 2907	544	0	0	48	200	999	
Friday 2907	545	0	0	48	200	0	
Friday 2907	546	60	200	48	200	100	
Friday 2907	547	60	200	48	200	200	
Friday 2907	548	60	200	48	200	300	
Friday 2907	549	60	200	48	200	400	
Friday 2907	550	0	0	24	200	999	
Friday 2907	551	0	0	24	200	0	
Friday 2907	552	60	200	24	200	100	
Friday 2907	553	60	200	24	200	200	
Friday 2907	554	60	200	24	200	300	
Friday 2907	555	60	200	24	200	400	
Friday 2907	556	0	0	60	200	999	
Friday 2907	557	0	0	60	200	0	
Friday 2907	558	60	200	60	200	100	
Friday 2907	559	60	200	60	200	200	
Friday 2907	560	60	200	60	200	300	
Friday 2907	561	60	200	60	200	400	
Friday 2907	562	0	0	60	200	999	
Friday 2907	563	0	0	60	200	0	
Friday 2907	564	50	200	60	200	100	
Friday 2907	565	50	200	60	200	200	
Friday 2907	566	50	200	60	200	300	
Friday 2907	567	50	200	60	200	400	
Friday 2907	568	0	0	40	200	999	
Friday 2907	569	0	0	40	200	0	
Friday 2907	570	50	200	40	200	100	
Friday 2907	571	50	200	40	200	200	
Friday 2907	572	50	200	40	200	300	
Friday 2907	573	50	200	40	200	400	